WAVE GROUP FORCED NEARSHORE CIRCULATION: A GENERATION MECHANISM FOR MIGRATING RIP CURRENTS AND LOW FREQUENCY MOTION

Rachel Elizabeth Fowler and Robert A. Dalrymple

RESEARCH REPORT NO. CACR-91-03
March, 1991

CENTER FOR APPLIED COASTAL RESEARCH
Department of Civil Engineering
University of Delaware
Newark, DE 19716

TABLE OF CONTENTS

LIST OF FIGURES

iv

LIST OF TABLES

ABSTRACT

Forcing of the nearshore circulation system by incident wave groups is examined. Particular attention is focused on the generation of migrating rip currents and the associated development of low frequency motion. Simple, linear theory is used to study the interaction of two incident wave trains, and expressions for the total free surface elevation and the wave group envelope are developed. For incident wave trains of the same frequency, stationary rip currents are known to develop at the intersection of the wave envelope nodal lines and the beach. For wave trains of slightly different frequencies, the wave group envelope is not stationary. The hypothesis of the migrating rip current generation mechanism is that the rip currents will move slowly along the beach as the nodal lines propagate through the wave field.

Laboratory experiments are performed to prove the validity of the proposed mechanism, using the directional wave basin in the Ocean Engineering Laboratory. Eight different experimental test cases are investigated. Water surface elevations and cross–shore and longshore velocities are measured at a number of locations in the nearshore region for each case. The experimental work shows that offshore, incident wave groups, with slightly different frequencies, can force a response of the nearshore circulation system in the form of migrating rip currents. Analysis of the experimental results categorizes the migrating rip currents as very low frequency motion in the far infra–gravity, or FIG, energy band. It is suggested that migrating rip currents, in addition to the recently discovered shear waves, are a valid generation mechanism for very low frequency motion in the nearshore region.

Chapter 1

THE NEARSHORE CIRCULATION SYSTEM

1.1 Introduction

A primary concern of coastal engineers is understanding and predicting the movement of sediments in the nearshore area. This ability is fundamentally important for the planning and design of coastal structures. Excessive accretion of coastal sediments in the vicinity of some of these structures can render them useless. Alternatively, severe erosion can result in the failure of coastal protection measures, leading to the destruction of valuable hinterland by the encroaching sea.

Before coastal engineers can understand sediment transport processes, however, they must first have a sound knowledge of the forces driving the sediment movements, i.e. the nearshore circulation system. Features of the nearshore circulation system can be categorized in to two groups; currents, and low frequency motion.

1.2 Nearshore Currents

Nearshore currents, such as longshore, cross–shore and rip currents, are wind and/or wave–induced flows. Diffuse return flows can also be generated by pressure, salinity and/or density gradients, but such low velocity water drifts can be considered negligible by coastal engineers as a mechanism for sediment movement.

Longshore currents are generated in the nearshore region by incident wave trains with an oblique angle of incidence to the shoreline. The induced currents are unidirectional, flowing downwave, parallel to the shoreline. The majority of the longshore flow is confined between the mean water level (MWL) and the breaker line, and the velocity of the current is proportional to the angle of incidence of the incoming wave trains. Longshore currents are of major importance to coastal engineers as they can be responsible for

1

transporting many thousands of cubic meters of sand along a coastline per year. Placement of structures such as groynes or jetties, interrupt the longshore transport, causing accumulation updrift of the structure, and erosion downdrift.

Contrary to longshore currents, cross–shore currents transport sediments in the on/offshore direction. These currents develop in order to maintain the mass flux balance in the surf zone. Cross–shore currents are often horizontally segregated, with mean onshore flows in the uppermost part of the water column, and mean seaward flows, often called undertow currents, near the sea bed. Cross–shore currents can carry sediments in both on- and offshore directions, but the offshore currents cannot transport sediments far beyond the breaker line.

Rip currents are more powerful surface currents and are a major mechanism for water and sediment exchange across the breaker line. A rip current can transport large volumes of sediment offshore, depositing it at the head of the rip current where the flow dissipates, see figure 1.1. Only small amounts of sediment may be carried back onshore with the slow return flow. Many generation mechanisms for rip currents have been proposed, including periodic longshore bathymetry, wave interaction with coastal structures such as breakwaters and jetties, wave–current interaction, incident edge waves, and synchronous, intersecting wave trains. These various mechanisms are discussed and evaluated in Dalrymple (1978).

In general, nearshore currents are viewed as stationary processes. The current velocities, and the rate at which they transport sediments, are constant over time. Their spatial structure may be periodic, for example, rip currents at regular intervals along a beach.

These features of the nearshore circulation system receive the most attention from coastal engineers concerned about sediment movements. They are assumed to provide the major mechanisms for transport of sediments in the nearshore region, and for this reason, they have been studied extensively.

rip current cell

head of rip current

head of rip current

breaker
line

rip cell length, L_r

BEACH
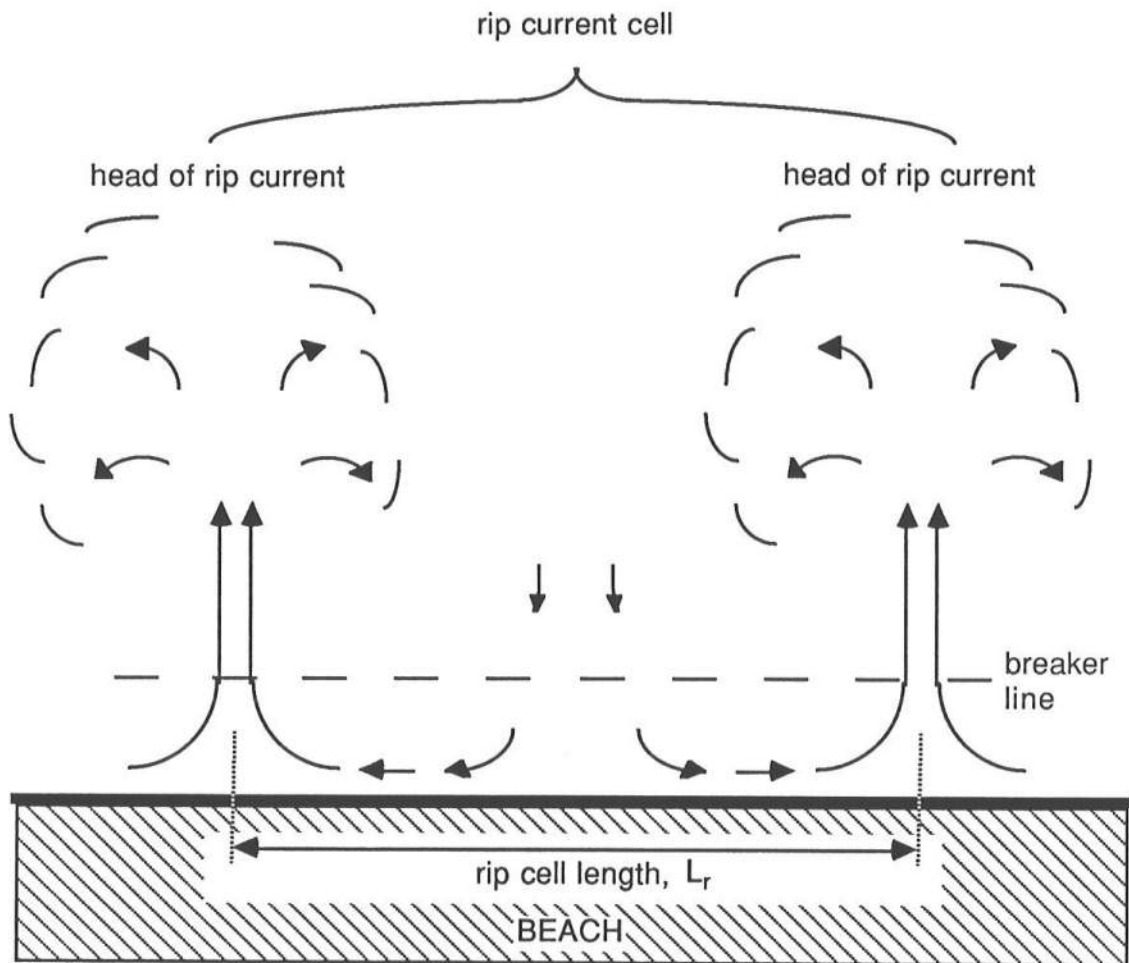
Figure 1.1: Definition sketch of a rip current system.

1.3 Low Frequency Motion

Underlying the nearshore currents are low frequency motions (frequencies < incident wave frequencies; periods > 30 seconds) which are typically unsteady and periodic in nature. These motions include surf beat, edge waves and far infra–gravity motions. Much attention has been given to the characterization of these low frequency motions, but as yet, their generation mechanisms are not fully understood.

The significance of low frequency motion to the transportation of sediments in the nearshore region was highlighted in a field study by Wright, Guza and Short (1982). From measurements made at a high energy, extremely dissipative beach in southern Australia, they found evidence that the surf beat frequency contribution to the nearshore currents increased shoreward as the incident wave contribution decreased. The surf beat related currents were stronger than those induced by the incident waves and hence, due to the rate of sediment transport being dependent on the cube of the instantaneous velocity, their sediment transporting capabilities were much greater. They concluded that sediment transport in the inner surf zone and the swash zone was dominated by surf beat energy rather than incident wave energy. Despite the results of this work, coastal engineers generally ignore low frequency motion as a mechanism for transporting sediments in the nearshore region.

1.4 Objectives of the Present Work

The fundamental aim of the research detailed in this thesis was to study the nearshore circulation system and evaluate its response to forcing by offshore wave groups. Theoretical investigations of the interaction of incident wave trains were specifically directed towards the development of a generation mechanism for migrating rip currents. Laboratory experiments were performed to assess the validity of this mechanism. In addition, the development of low frequency motion associated with the rip currents was examined in order to evaluate the hypothesis that a nearshore current system could be coupled with unsteady, low frequency motions.

Chapter 2

WAVE GROUPS AND LOW FREQUENCY MOTION
IN THE NEARSHORE REGION

2.1 Surf Beat

Initial discoveries of low frequency motion in the nearshore region were made by Munk (1949) and Tucker (1950). Munk (1949) conducted field experiments at the Scripps Institution of Oceanography, La Jolla, California, using a "tsunami recorder," located 304.8 m (1000 ft) offshore, which recorded long period water surface elevations, and a bottom mounted pressure sensor, located 609.6 m (2000 ft) offshore, which was designed to measure swell. From the tsunami recorder, Munk observed 2–3 minute oscillations in the water surface elevation that were related to the variability in height and period of the incident waves. He examined the mass transport associated with the incoming waves, which were recorded by the swell sensor, and suggested that, for a fixed period of time, the total mass transport into the surf zone from all the incident waves is equal to a constant return flow for the same period. However, when a group of higher than average waves enters the surf zone, there is, temporarily, an excess of mass transport over the constant seaward return flow. Munk termed this excess mass transport the "integrated swell record" and compared it to the low frequency oscillations in the tsunami record. He found a close resemblance between the two records provided they were offset by 140 seconds. This offset was explained as the time taken for the incident waves to propagate to the surf zone and be reflected back in the form of long, low frequency oscillations. So, Munk proposed that an excess of shoreward mass transport arriving in the surf zone under groups of high waves would be reflected as long, low frequency oscillations which he named "surf beat."

Tucker independently found similar, small amplitude, long period water level fluctuations during a field experiment conducted at Perranporth in Cornwall, England. He

found an approximately linear relationship between the peak wave heights of the long waves and the heights of groups of short incident waves. Similar to Munk's observations, Tucker found groups of high incident waves were associated with long waves which were observed 4–5 minutes later. Tucker also attributed this delay to the time taken for the groups of waves to reach the beach and be reflected as long waves. He found the best evidence of long waves during periods of long, regular groups of incident waves and also observed that the incident wave groups were out of phase with the long waves. Tucker developed Munk's suggestion that the long waves were due to the varying mass transport in the incoming waves groups, and formulated a hypothesis based on shoreward mass transport at the breaker line. Using a conservation of momentum argument, Tucker proposed that, as the wave groups reached the surf zone and caused a sudden increase of mass transport shoreward, there would be an equivalent acceleration of water seaward. He stated that this would result in a depression in the water surface elevation at the breaker line which would propagate seaward, providing the phase difference observed between the incident wave groups and the long waves.

Following these initial field observations of low frequency motion, Biesel (1952) and Longuet–Higgins and Stewart (1962, 1964) studied surf beat theoretically. Biesel demonstrated that a forced, small amplitude, second–order undulation accompanies a first–order wave group and is 180° out of phase with that wave group. This concept is shown, diagrammatically, in figure 2.1. Longuet–Higgins and Stewart developed this idea in terms of radiation stresses. They suggested that, when the incident wave groups are destroyed at the breaker line, the forced, second–order waves associated with the wave groups are released and propagate seaward as free waves. This would account for the time delays in the correlations between the incident wave groups and the long waves as seen by Munk and Tucker, and would also account for Tucker's observation that groups of high waves are associated with the trough of a long wave.
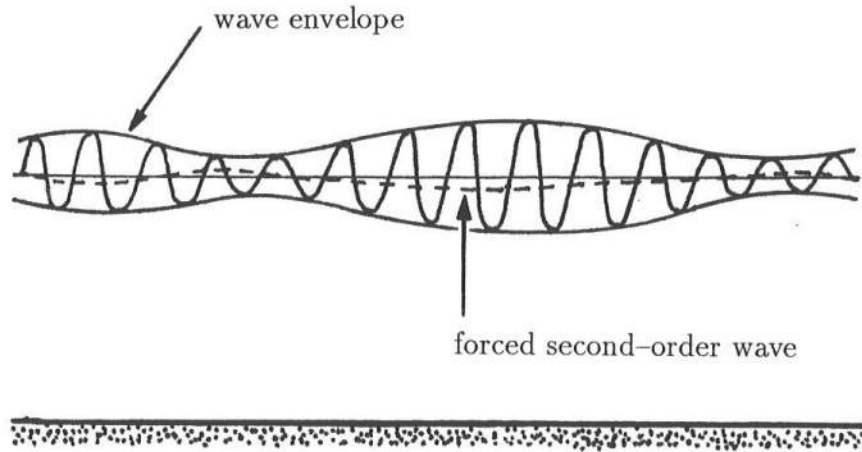
Figure 2.1: A forced, second–order wave accompanying a first–order wave group.

2.2 Edge Waves

In an expansion of surf beat studies to three dimensions, investigations into wave groups and low frequency motion in the surf zone have focused on edge waves. Edge waves are free waves which are trapped to the shoreline; they are spatially (in the longshore direction) and temporally periodic.

Gallagher (1971) demonstrated, theoretically, that non–linear interactions between wind waves with certain frequencies and directions, leading to an inter–frequency energy transfer, can initiate forced edge waves in the surf zone at the group frequency, which can grow resonantly. Guza and Davis (1974) showed, theoretically, that edge waves could be generated by a standing wave normally incident on a beach. They demonstrated that incident wave energy can be transferred to edge waves through weak resonant interactions. However, the frequencies of the edge waves generated were limited to half those of the incident waves.

In order to investigate the importance of wave interactions to the development of edge wave motions in the nearshore region, Bowen and Guza (1978) performed a series of

laboratory experiments in which they considered both resonant and non–resonant inter-actions between incident wave trains. They confirmed Gallagher's hypothesis that, when the frequency and longshore wave number of incident waves groups satisfy the edge wave dispersion relationship, edge wave motions can be generated and maintained. This edge wave generation mechanism was found to remain valid even when the incident waves were breaking, a conclusion that could not be drawn from the theoretical investigations due to the complexity of dealing with breaking waves. Bowen and Guza found the low frequency response of the nearshore region to be much stronger when the resonance conditions for edge wave growth were satisfied. They concluded that surf beat, or low frequency motion in the nearshore region, was primarily due to edge waves.

Huntley, Guza and Thornton (1981) summarized that there are three different generation mechanisms for nearshore low frequency motion:

(i) progressive edge waves,

(ii) standing edge waves (caused by an obstruction or topographic form),

(iii) forced second–order waves under incident wave groups.

They analysed data from the National Sediment Transport Study field experiment con-ducted at Torrey Pines Beach, California, in 1978, in an attempt to assess the relative importance of these three mechanisms. Their analysis focused on data from two arrays of current meters, one in the longshore direction, in the surf zone, and the other in the cross–shore direction, traversing the breaker line. Data from the longshore array provided unequivocal evidence of the existence of progressive edge waves in the surf zone at surf beat frequencies. The observed progressive edge waves were in very good agreement with the theoretically predicted edge waves dispersion relationship curves.

The observed edge waves were primarily modes zero and one and were curiously separated in frequency. Mode zero edge waves occurred at lower frequencies than the mode one edge waves. Reasons for the separation of modes were suggested, such as the existence of nodes in the offshore profile of the edge waves at certain frequencies, but no firm conclusions were made. Analysis of data from the on/offshore current meter array did not provide such solid evidence for the presence of progressive edge waves; instead

other forms of energy were seen to be important. It was suggested that standing edge waves were present along with forced long waves associated with incident waves groups. Both of these low frequency motion generation mechanisms would have been much more difficult to detect and hence less pronounced in the longshore direction.

2.3 Far Infra–Gravity Motions

Data from the Torrey Pines field experiment were also analysed by Tang and Dalrymple (1989); however, they concentrated on nearshore motions at much lower frequencies than those in the edge wave band. They found the significant majority of energy in the infra–gravity band was confined to very low frequencies ($<$0.0024 Hz). This very low frequency motion was predominantly observed in the longshore current records inside the surf zone, whereas energy in the cross–shore current records was considerably lower. From these observations, and the absence of large water surface elevations, Tang and Dalrymple concluded that the very low frequency motion was not pure edge wave motion, but rather a forced response. For the observed period of the nearshore motion, of the order of 1000 seconds, the corresponding edge wave length for Torrey Pines Beach would be approximately 30 km, and would therefore be detectable offshore. However, no evidence of such a wave form was found in the offshore pressure sensor records so it was suggested that the very low frequency motion was locally induced and decayed rapidly seaward.

Representation of the data in wave number–frequency space, figure 2.2, confirmed the presence of significant low frequency energy (frequencies $<$ 0.0015 Hz, periods $>$ 660 seconds), removed from the edge wave dispersion relationship curves, in the nearshore region. Figure 2.2 also shows the edge wave energy identified by Huntley *et al.* (1981). Tang and Dalrymple proceeded to demonstrate, through the use of various statistical analysis methods, that offshore wave groups were significantly correlated with the measured, very low frequency motion. During the field experiment, observations were made of slowly migrating rip current cells in the surf zone which had the same wave length as the very low frequency motion. Tang and Dalrymple hypothesised that the incident wave groups were forcing the observed response of the nearshore circulation in the form
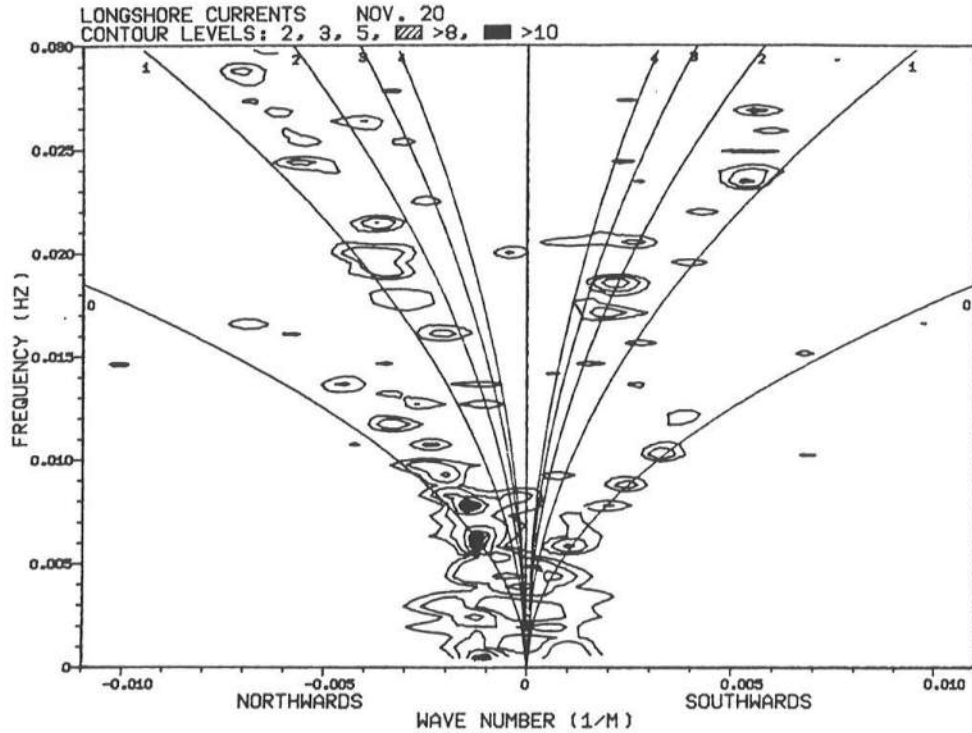
Figure 2.2: Wave number–frequency spectrum derived from cross–shore current measurements at an offshore location. Torrey Pines Beach, California, USA. (Fig. 10B–5 of Tang and Dalrymple, 1989)

of migrating rip currents, which, in turn, had a very low frequency motion signature in wave number–frequency space.

The most recent discussion of very low frequency motion in the nearshore region has focused on data from the SUPERDUCK field experiment (see Crowson *et al.* (1988)) conducted at Duck, North Carolina, in 1986. Analysis of this data by Oltman–Shay, Howd and Birkemeier (1989) produced convincing evidence of high energy motion at very low frequencies. Low frequency oscillations were initially seen in the velocity records, figure 2.3, with the longshore velocity record in particular clearly showing a periodicity of the order of 1000 seconds. By analysing velocity records from longshore and cross–shore arrays
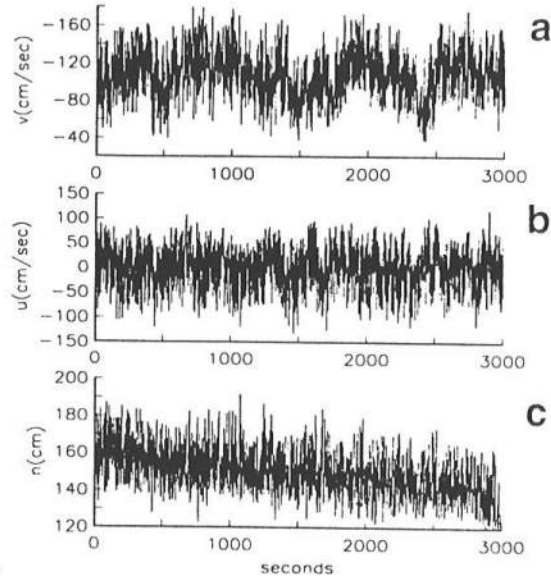
Figure 2.3: Time series measurements of (a) longshore (v), (b) cross–shore (u) velocity, and (c) surface displacement (η) colocated in the surf zone. Duck, North Carolina, U.S.A. (Fig. 2 of Oltman–Shay, Howd and Birkemeier, 1989.)

Oltman–Shay *et al.* demonstrated that the low frequency motions present in the nearshore region were clearly distinct from edge wave motions. The low frequency motions had shorter wave lengths at edge wave frequencies than those predicted by the edge wave dispersion relationship. Figure 2.4 shows edge wave motions at frequencies > 0.01 Hz, but also displays other concentrations of energy, removed from the edge wave dispersion relationship curves, in the frequency range 0.001 Hz < f < 0.01 Hz. This very low frequency motion also demonstrates an approximately linear relationship between cyclic longshore wave number (1/longshore wave length) and frequency, implying that the low frequency motion is non–dispersive.

Oltman–Shay *et al.* noted that the very low frequency motion was observed only in the presence of a mean longshore current, and would change speed and direction with that current. They reviewed a small subset of velocity data and compared it with off-shore significant wind wave height, but this limited study did not reveal any particular
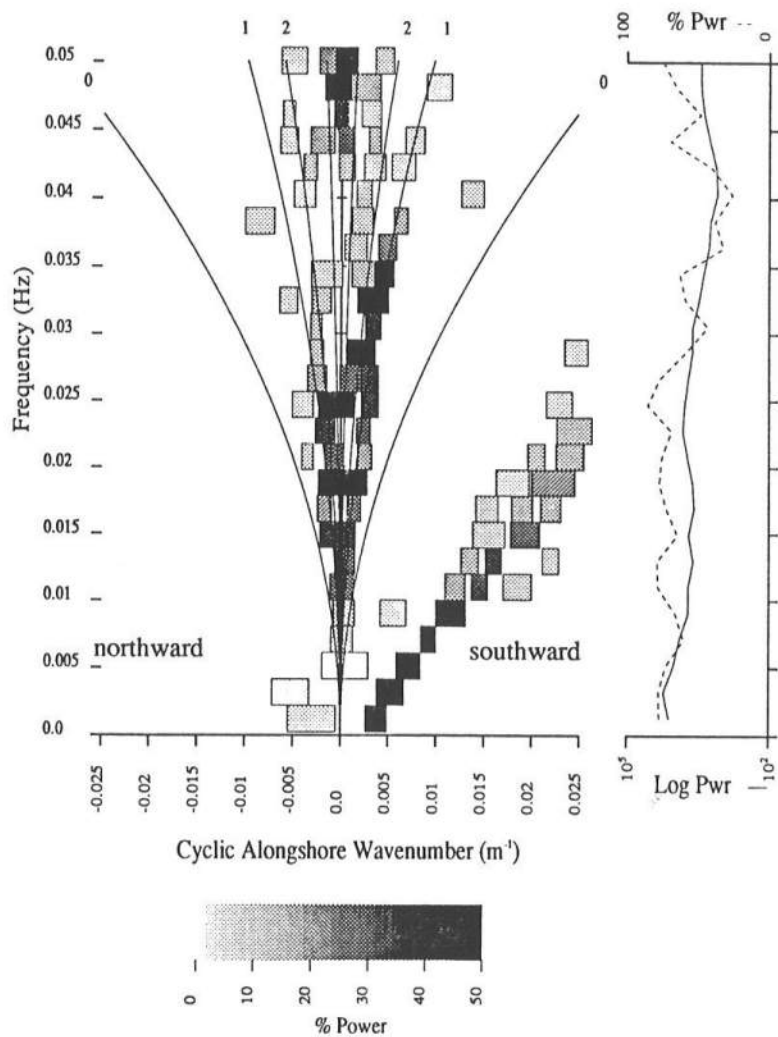
Figure 2.4: Wave number–frequency spectrum derived from cross–shore velocity measurements in the surf zone. Duck, North Carolina, U.S.A. (Fig. 6b of Oltman–Shay, Howd and Birkemeier, 1989.)

relationship between the low frequency energy and the offshore significant wave height.

Oltman–Shay *et al.* named the kinematically distinct, low frequency band of energy the "far infra–gravity (FIG) band," and in a companion paper, Bowen and Holman (1989), it was suggested that the observed motions were generated by shear instabilities in the mean longshore current. Bowen and Holman proposed that these instabilities lead to the formation of longshore progressive "shear waves." The restoring force for these waves is vorticity rather than gravity, which provides an explanation for the wave lengths being shorter than the minimum required for gravity waves (mode zero edge waves) at these frequencies. Oltman–Shay *et al.* concluded that shear waves were a common phenomenon in the nearshore region and suggested that they were responsible for the very low frequency motion observed at Torrey Pines Beach by Tang and Dalrymple.

2.4 Summary

All these previous studies have highlighted the importance of wave groups to the dynamics of the nearshore circulation system. Three different forms of low frequency motion have been associated with wave groups: forced long waves accompanying incident wave groups, edge waves generated by interactions between incoming waves, and finally, far infra–gravity motions strongly correlated with offshore incident wave groups and linked with the presence of slowly migrating rip currents in the surf zone. Discussions about far infra–gravity motions, in particular, have provided a strong incentive to examine, in more detail, the effects of wave group forcing on the nearshore circulation system.

Chapter 3

THEORETICAL DEVELOPMENT OF A MIGRATING RIP
CURRENT GENERATION MECHANISM

3.1 Introduction

The theoretical examination of the response of the nearshore circulation system to forcing by wave groups is initiated by studying the simplest form of wave groups. This is achieved by considering the intersection of two sinusoidal, incident wave trains with different frequencies. In order to keep the theoretical development simple, the two wave trains are represented using linear theory.

Consider the two incident wave trains impinging on a planar beach as shown in figure 3.1. The wave trains have wave number vectors k_1 and k_2, and angles of incidence θ_1 and θ_2. Note from the figure that the x–axis is positive onshore, and the y–axis is parallel to the beach. From linear wave theory the total velocity potential and total water surface elevation are given by

$$\phi_t(\mathbf{x}, z, t) = \frac{ga_1}{\omega_1} \frac{\cosh k_1(h + z)}{\cosh k_1 h} \cos \psi_1 + \frac{ga_2}{\omega_2} \frac{\cosh k_2(h + z)}{\cosh k_2 h} \cos \psi_2 \qquad (3.1)$$

and

$$\begin{aligned} \eta_t(\mathbf{x}, t) &= \eta_1 + \eta_2 \\ &= \left. \frac{1}{g} \frac{\partial \phi_t}{\partial t} \right|_{z=0} = a_1 \sin \psi_1 + a_2 \sin \psi_2 \end{aligned} \qquad (3.2)$$

where $\psi_i = (\mathbf{k_i} \cdot \mathbf{x} - \omega_i t)$, phase function of wave train, $i = 1, 2$

$\mathbf{k}_i = |\mathbf{k}_i| \cos \theta_i = k_i \cos \theta_i$, wave number of wave train, $i = 1, 2$

ω_i = frequency of wave train, $i = 1, 2$

a_i = amplitude of wave train, $i = 1, 2$

14
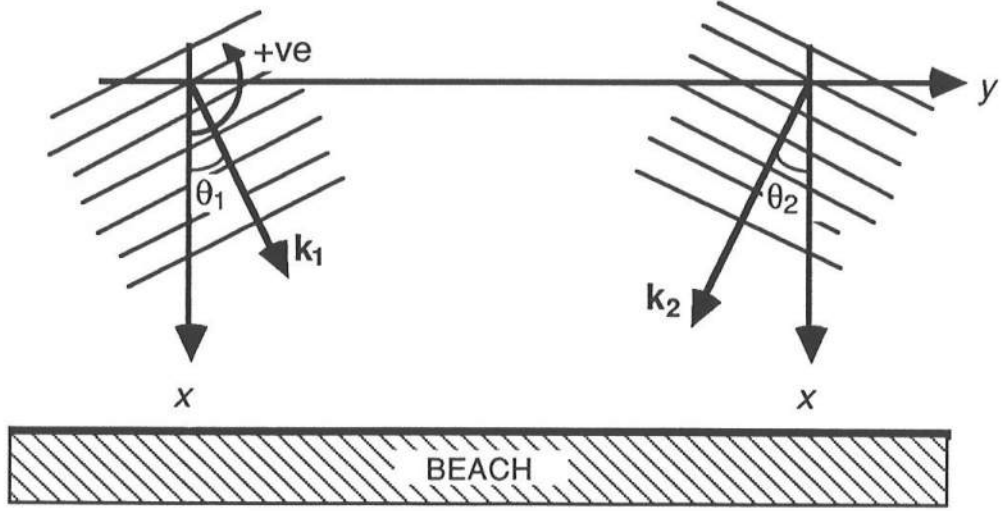
Figure 3.1: Coordinate system and sign conventions.

$$g \; = \text{acceleration due to gravity}$$

$$h \; = \text{water depth}$$

$$\mathbf{x} \; = \begin{pmatrix} x \\ y \end{pmatrix}$$

The wave numbers, $\mathbf{k_i}$, are related to the angular frequencies of the waves by the linear dispersion relationship,

$$\omega_i{}^2 = g|\mathbf{k}_i|\tanh|\mathbf{k}_i|h \qquad \text{for } i = 1,2 \qquad (3.3)$$

3.2 Development

Through the use of various trigonometric identities, the expression for the total water surface elevation can be rewritten as

$$\eta_t(\mathbf{x}, t) = 2a_1 \sin\left(\frac{\psi_1 + \psi_2}{2}\right)\cos\left(\frac{\psi_1 - \psi_2}{2}\right) + (a_1 - a_2)\sin\psi_2 \qquad (3.4)$$

which is the sum of a modulated sine wave and a plane wave train (the difference term). Expressions for the average wave number vector and the average frequency of the two wave
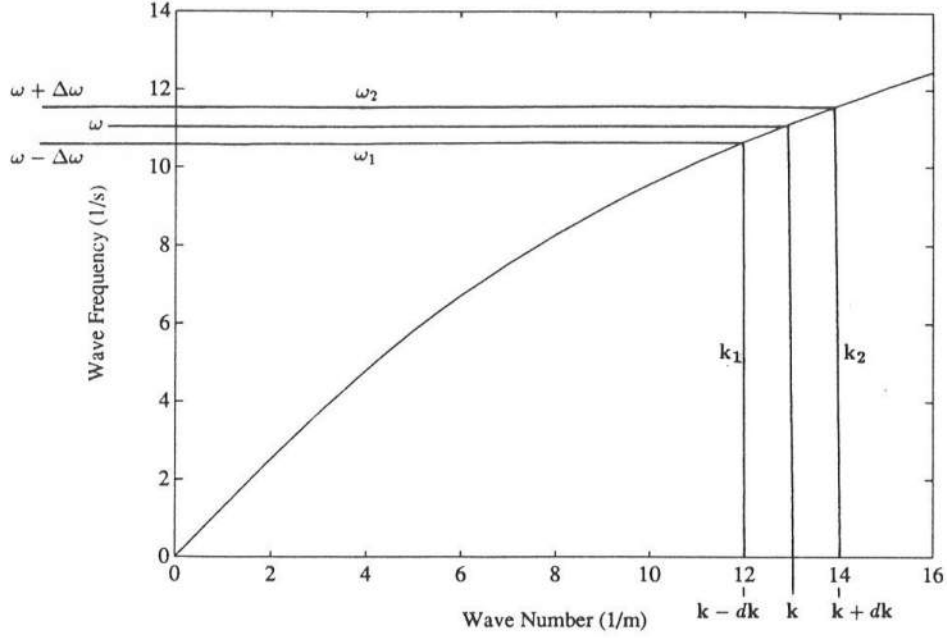
Figure 3.2: Linear dispersion relationship curve for a given water depth, h.

trains are now introduced. Figure 3.2 shows a graph of the linear dispersion relationship on which the wave number vectors, $\mathbf{k}_1$ and $\mathbf{k}_2$, are represented as

$$\mathbf{k}_1 \;=\; \mathbf{k} - d\mathbf{k} \tag{3.5}$$

$$\mathbf{k}_2 \;=\; \mathbf{k} + d\mathbf{k} \tag{3.6}$$

and where the average wave number vector is defined as

$$\mathbf{k} = \frac{\mathbf{k}_1 + \mathbf{k}_2}{2} \tag{3.7}$$

Corresponding expressions for the wave frequencies are obtained via the Taylor series:

$$\omega_1 \;=\; \omega - \frac{\partial \omega}{\partial \mathbf{k}} d\mathbf{k} + \frac{\partial^2 \omega}{\partial \mathbf{k}^2} \frac{(d\mathbf{k})^2}{2} - \cdots \cdots \tag{3.8}$$

$$\omega_2 \;=\; \omega + \frac{\partial \omega}{\partial \mathbf{k}} d\mathbf{k} + \frac{\partial^2 \omega}{\partial \mathbf{k}^2} \frac{(d\mathbf{k})^2}{2} + \cdots \cdots \tag{3.9}$$

which, assuming $d\mathbf{k}(= \Delta \mathbf{k}) \ll 1$, are truncated after the second term, giving

$$\omega_1 \;=\; \omega - \Delta\omega \tag{3.10}$$

$$\omega_2 \;=\; \omega + \Delta\omega \tag{3.11}$$

By adding these two expressions, the average angular frequency is developed,

$$\omega = \frac{\omega_1 + \omega_2}{2} \tag{3.12}$$

In addition, expressions for the difference frequency and difference wave number vector are obtained,

$$2\Delta\omega = \omega_2 - \omega_1 \tag{3.13}$$

$$2\Delta\mathbf{k} = \mathbf{k}_2 - \mathbf{k}_1 \tag{3.14}$$

The total water surface elevation, η_t, can now be written in terms of ω, $\mathbf{k}$, $\Delta\omega$ and $\Delta\mathbf{k}$,

$$\eta_t(\mathbf{x}, t) = 2a_1 \underbrace{\sin \overbrace{(\mathbf{k} \cdot \mathbf{x} - \omega t)}^{\psi}}_{\text{carrier wave}} \underbrace{\cos \left(\frac{1}{2} \overbrace{(\Delta\mathbf{k} \cdot \mathbf{x} - \Delta\omega\, t)}^{\Delta\psi} \right)}_{\text{wave envelope}}$$

$$+ (a_2 - a_1) \sin \left(\underbrace{(\mathbf{k} \cdot \mathbf{x} - \omega t) - \left(\frac{1}{2}(\Delta\mathbf{k} \cdot \mathbf{x} - \Delta\omega t) \right)}_{\psi_2} \right) \tag{3.15}$$

which is composed of a carrier wave, a wave envelope and an additional plane wave train (the difference term) which disappears for $a_1 = a_2$. From this equation, expressions are developed for the direction and speed of propagation of the carrier wave and the wave envelope. For the carrier wave,

$$\text{direction of propagation } (= \text{grad } \psi) = \frac{\mathbf{k}_1 + \mathbf{k}_2}{2} \tag{3.16}$$

$$\text{speed of propagation } \left(= \frac{\omega}{\mathbf{k}} \right) = \frac{\omega_1 + \omega_2}{|\mathbf{k}_1 + \mathbf{k}_2|} \tag{3.17}$$

and for the wave envelope,

$$\text{direction of propagation } (= \text{grad } \Delta\psi) = \frac{\mathbf{k}_1 - \mathbf{k}_2}{2} \tag{3.18}$$

$$\text{speed of propagation } \left(= \frac{\Delta\omega}{\Delta\mathbf{k}} \right) = \frac{\omega_1 - \omega_2}{|\mathbf{k}_1 - \mathbf{k}_2|} = Cg \tag{3.19}$$

These are represented in the form of vector diagrams, for one particular set of incident wave conditions, in figure 3.3.
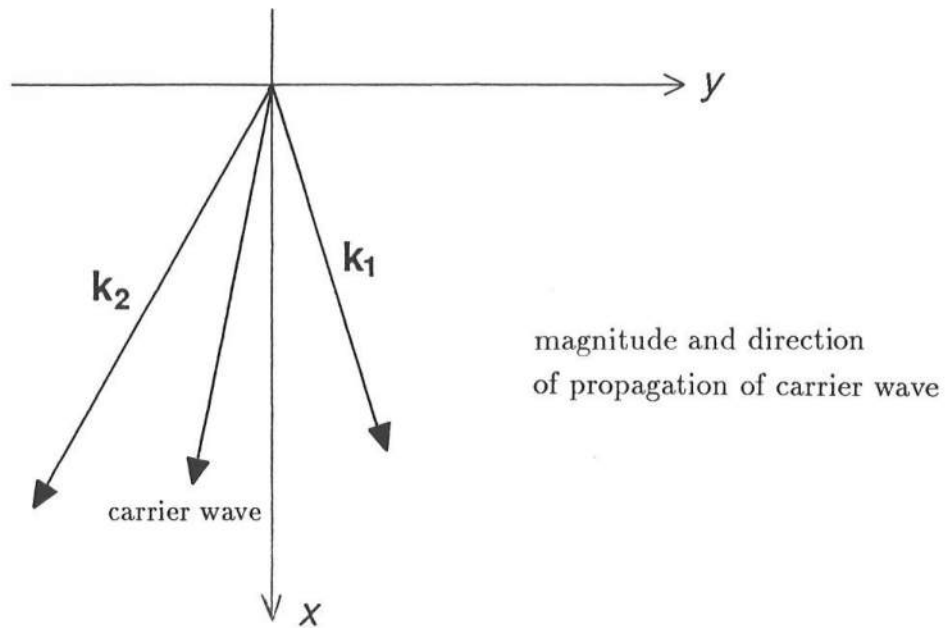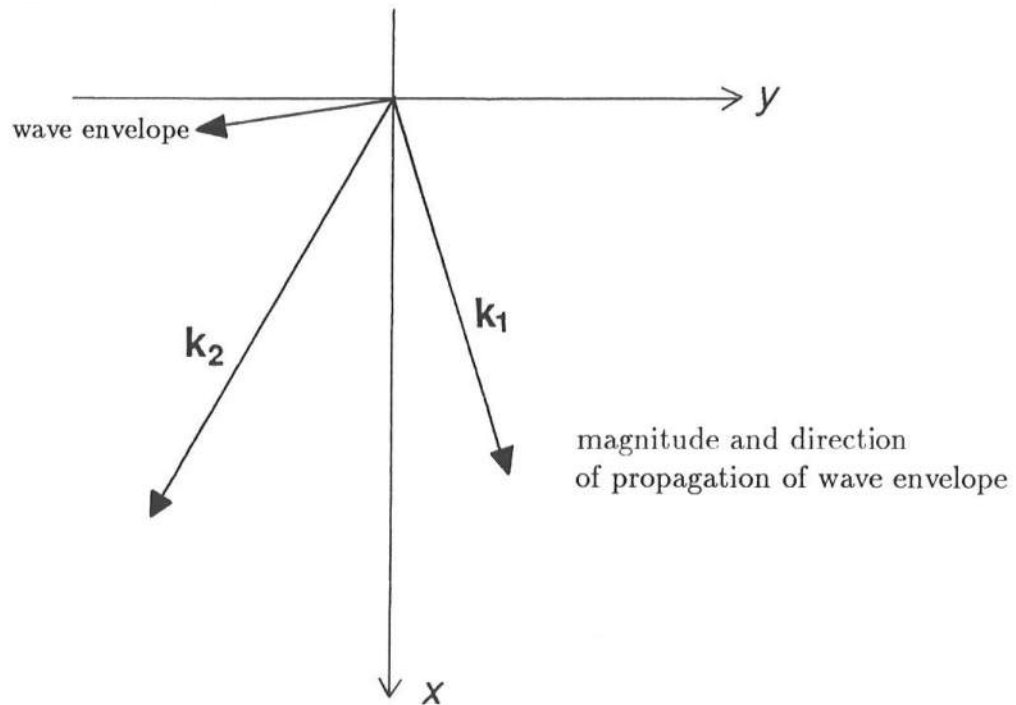
Figure 3.3: Vector representation of the speed and direction of propagation of the carrier wave and the wave envelope for a selected set of incident wave conditions.

By multiplying equation 3.19 by a unit vector and dotting it with the unit vector in the y (longshore) direction, an expression for the longshore component of the speed of propagation of the wave envelope is developed,

$$\mathbf{Cg} = \frac{(\omega_1 - \omega_2)}{|\mathbf{k}_1 - \mathbf{k}_2|} \cdot \frac{(\mathbf{k}_1 - \mathbf{k}_2)}{|\mathbf{k}_1 - \mathbf{k}_2|} \tag{3.20}$$

$$Cg_y = Cg \frac{\mathbf{k}_1 - \mathbf{k}_2}{|\mathbf{k}_1 - \mathbf{k}_2|} \cdot \mathbf{j} \tag{3.21}$$

Expanding the $\mathbf{k}_1 - \mathbf{k}_2$ term gives

$$\mathbf{k}_1 - \mathbf{k}_2 = (k_1 \cos \theta_1 \mathbf{i} + k_1 \sin \theta_1 \mathbf{j}) - (k_2 \cos \theta_2 \mathbf{i} + k_2 \sin \theta_2 \mathbf{j}) \tag{3.22}$$

$$= (k_1 \cos \theta_1 - k_2 \cos \theta_2)\mathbf{i} + (k_1 \sin \theta_1 - k_2 \sin \theta_2)\mathbf{j} \tag{3.23}$$

and taking the absolute value,

$$|\mathbf{k}_1 - \mathbf{k}_2| = \sqrt{(k_1 \cos \theta_1 - k_2 \cos \theta_2)^2 + (k_1 \sin \theta_1 - k_2 \sin \theta_2)^2} \tag{3.24}$$

$$= \sqrt{k_1^2 + k_2^2 - 2k_1 k_2 \cos(\theta_1 - \theta_2)} \tag{3.25}$$

Equations 3.19, 3.23 and 3.25 are then substituted into the expression for the longshore speed of propagation of the wave envelope,

$$Cg_y = Cg \frac{[(k_1 \cos \theta_1 - k_2 \cos \theta_2)\mathbf{i} + (k_1 \sin \theta_1 - k_2 \sin \theta_2)\mathbf{j}]}{|\mathbf{k}_1 - \mathbf{k}_2|} \cdot \mathbf{j} \tag{3.26}$$

$$= Cg \frac{(k_1 \sin \theta_1 - k_2 \sin \theta_2)}{|\mathbf{k}_1 - \mathbf{k}_2|} \tag{3.27}$$

$$= \frac{(\omega_1 - \omega_2)}{|\mathbf{k}_1 - \mathbf{k}_2|} \frac{(k_1 \sin \theta_1 - k_2 \sin \theta_2)}{|\mathbf{k}_1 - \mathbf{k}_2|} \tag{3.28}$$

The final expression for the longshore propagation of the wave envelope becomes

$$Cg_y = \frac{(\omega_1 - \omega_2)(k_1 \sin \theta_1 - k_2 \sin \theta_2)}{(k_1^2 + k_2^2 - 2k_1 k_2 \cos(\theta_1 - \theta_2))} \tag{3.29}$$

which is written in terms of the wave numbers, frequencies and angles of incidence of the two individual wave trains.

3.3 Longshore and Cross–Shore Velocities

From the total velocity potential, equation 3.1, expressions for the longshore and cross–shore velocities can be developed. For the cross–shore velocity,

$$u(\mathbf{x}, z, t) \quad = \quad -\frac{\partial \phi_t}{\partial x} \tag{3.30}$$

$$= \quad \frac{ga_1}{\omega_1} \mathbf{k}_1 \cos\theta_1 \frac{\cosh k_1(h+z)}{\cosh k_1 h} \sin\psi_1 \tag{3.31}$$

$$+\frac{ga_2}{\omega_2} \mathbf{k}_2 \cos\theta_2 \frac{\cosh k_2(h+z)}{\cosh k_2 h} \sin\psi_2 \tag{3.32}$$

The two "cosh" terms in this expression are functions of the wave number vectors, $\mathbf{k}_1$ and $\mathbf{k}_2$. These can be expressed as functions of the average wave number vector, $\mathbf{k}$, via the Taylor series:

$$f(\mathbf{k}_1) \quad = \quad f(\mathbf{k}) - \frac{\partial f(\mathbf{k})}{\partial \mathbf{k}} d\mathbf{k} + \frac{\partial^2 f(\mathbf{k})}{\partial \mathbf{k}^2} \frac{(d\mathbf{k})^2}{2} - \cdots\cdots \tag{3.33}$$

$$f(\mathbf{k}_2) \quad = \quad f(\mathbf{k}) + \frac{\partial f(\mathbf{k})}{\partial \mathbf{k}} d\mathbf{k} + \frac{\partial^2 f(\mathbf{k})}{\partial \mathbf{k}^2} \frac{(d\mathbf{k})^2}{2} + \cdots\cdots \tag{3.34}$$

which are truncated after the second term, assuming $d\mathbf{k}(= \Delta\mathbf{k}) \ll 1$, and where

$$f(\mathbf{k}) = \frac{\cosh \mathbf{k}(h+z)}{\cosh \mathbf{k} h}$$

The definitions of $\mathbf{k}$ and ω are incorporated, and taking $a_1 = a_2$, equation 3.32 becomes

$$u(\mathbf{x}, z, t) \quad = \quad ga\frac{\left(\mathbf{k} - \frac{\Delta\mathbf{k}}{2}\right)}{\left(\omega - \frac{\Delta\omega}{2}\right)} \cos\theta_1 \left(f(\mathbf{k}) - \frac{\partial f}{\partial \mathbf{k}} d\mathbf{k}\right) \sin\psi_1$$

$$+ga\frac{\left(\mathbf{k} + \frac{\Delta\mathbf{k}}{2}\right)}{\left(\omega + \frac{\Delta\omega}{2}\right)} \cos\theta_2 \left(f(\mathbf{k}) + \frac{\partial f}{\partial \mathbf{k}} d\mathbf{k}\right) \sin\psi_2 \tag{3.35}$$

Using a binomial expansion to eliminate the ω term in the denominator, a final expression for the cross–shore velocity is obtained,

$$u(\mathbf{x}, z, t) \quad = \quad ga\mathbf{k}f(\mathbf{k})(\cos\theta_1 \sin\psi_1 + \cos\theta_2 \sin\psi_2) + \text{Higher Order Terms in } d\mathbf{k}, d\omega \tag{3.36}$$

Similarly for the longshore velocity,

$$v(\mathbf{x}, z, t) \quad = \quad -\frac{\partial \phi_t}{\partial y} \tag{3.37}$$

$$= \quad ga\mathbf{k}f(\mathbf{k})(\sin\theta_1 \sin\psi_1 + \sin\theta_2 \sin\psi_2) + \text{Higher Order Terms in } d\mathbf{k}, d\omega \tag{3.38}$$

The total water surface elevation, longshore and cross–shore velocities for one particular set of incident wave conditions are plotted in figure 3.4. It can be seen that the water surface elevation (η_t) and cross–shore velocity (u) are in phase at both the incident wave and the wave group frequencies. However, the longshore velocity (v) moves in and out of phase with the cross–shore velocity at the incident wave frequency, being 180° out of phase at the nodal and antinodal points of the groups in the cross–shore velocity. At the group frequency the longshore velocity is a constant 180° out of phase. The maximum longshore velocities coincide with zero cross–shore velocities and water surface elevation. Similar phase differences at the wave group frequency were observed in the field by Kim and Huntley (1986). From velocity data acquired during a field experiment performed at Queensland Beach in St. Margaret's Bay, Nova Scotia, they found time lags between on/offshore velocity and longshore velocity of the order of 20 seconds. This is clearly seen in figure 3.5, which shows sample segments of time series from the field data. Kim and Huntley noted that the phase differences between the signals varied linearly with frequency implying that the time delay was non–dispersive. They also found some evidence that the time–delayed motions were contributing to low frequency motions in the surf zone. Several reasons for the observed time lags were proposed, such as the presence of waves reflected or diffracted by a structure or topographic form further along the shore, but no firm conclusions were made.

3.4 Necessary Conditions for Rip Current Generation

Returning to the expression for the speed of propagation of the wave envelope (equation 3.19), the special case where the intersecting wave trains have the same frequency is initially investigated. From this, the evolution to wave trains of different frequencies, and a generation mechanism for migrating rip currents is proposed.

3.4.1 Stationary Rip Currents

For intersecting wave trains of the same frequency, $\omega_1 = \omega_2$, it can be seen from equation 3.19 that

$$Cg = \frac{\omega_1 - \omega_2}{|\mathbf{k}_1 - \mathbf{k}_2|} = 0 \qquad (3.39)$$
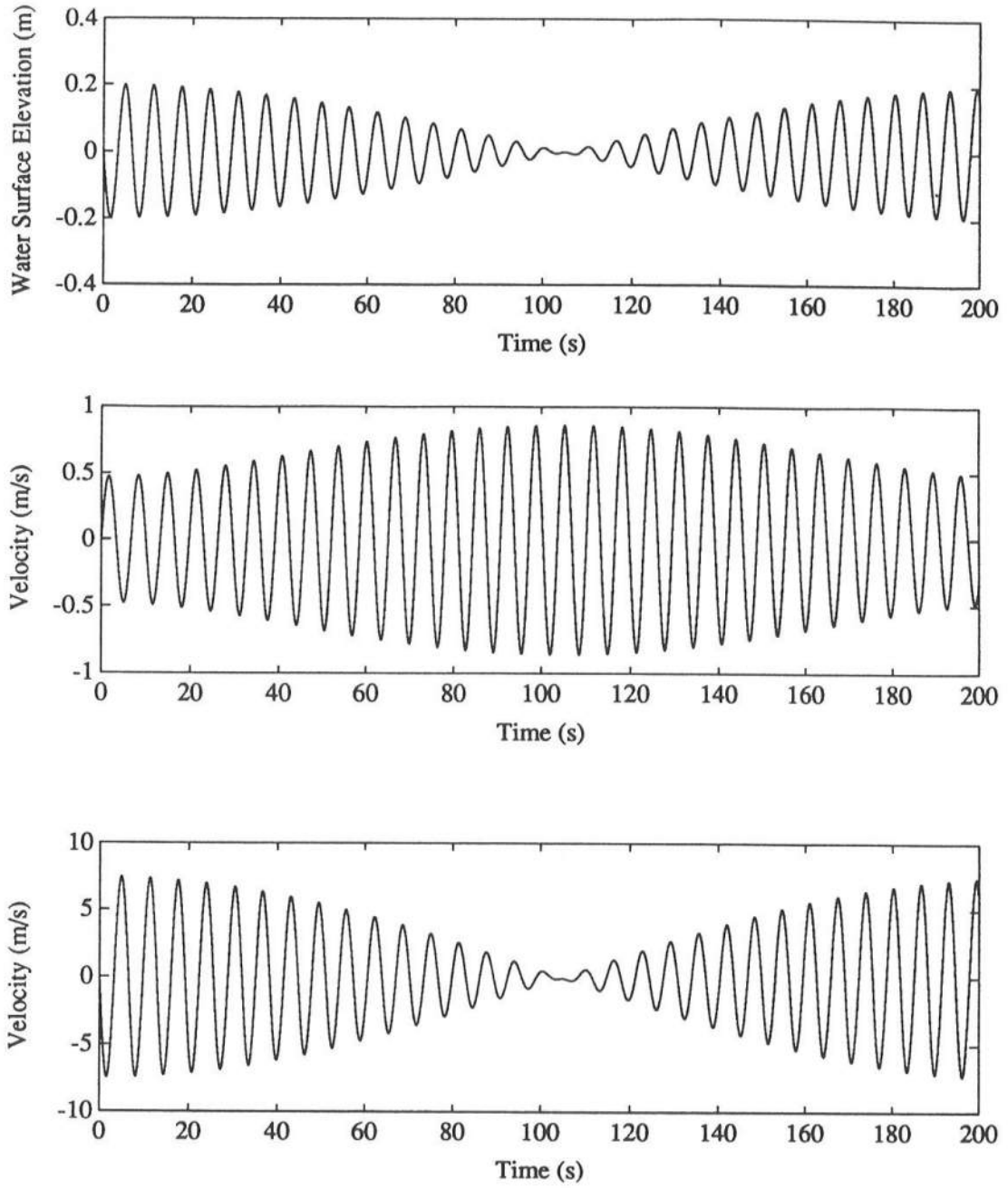
Figure 3.4: Theoretical water surface elevation (η_t), longshore velocity (v), and cross–shore velocity (u) for a selected set of incident wave conditions.

23
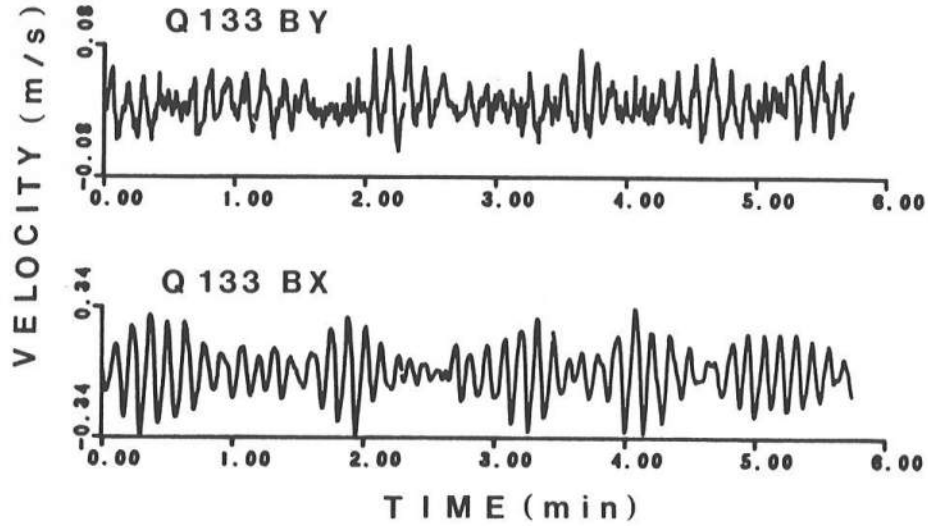
Figure 3.5: Sample segments of time series showing time lag between longshore (top) and cross–shore (bottom) velocities from Queensland Beach, Nova Scotia. (Fig. 3 of Kim and Huntley, 1986.)

and correspondingly, $Cg_y = 0$. Under these conditions, the groups in the wave field do not propagate. As the incident waves propagate towards the shore, they alternatively reinforce and cancel each other out, creating periodic, stationary longshore variations in wave height which describe the wave group envelopes. This incident wave interaction is shown diagrammatically in figure 3.6. In the general cross–shore direction there are lines of constant η_t. Note in particular, the lines of cancellation, or nodal lines, in the wave field, where $\eta_t = 0$. For incident wave trains of identical frequency these nodal lines are stationary. Dalrymple (1975) discussed this phenomenon in terms of spatial variations in set–up and set–down. He stated that minimum set–up occurs along the nodal lines in the surf zone. Furthermore, he proposed that the longshore spatial variations in wave height and set–up lead to the development of nearshore circulation cells. Due to the unbalanced hydrostatic forces, currents flow from regions of high waves and maximum set–up to regions of minimum set–up and zero wave height, i.e., where the nodal lines in the wave field intersect the beach. Two currents traveling in opposite directions meet at this point and flow offshore in the form of a rip current. For two wave trains with equal
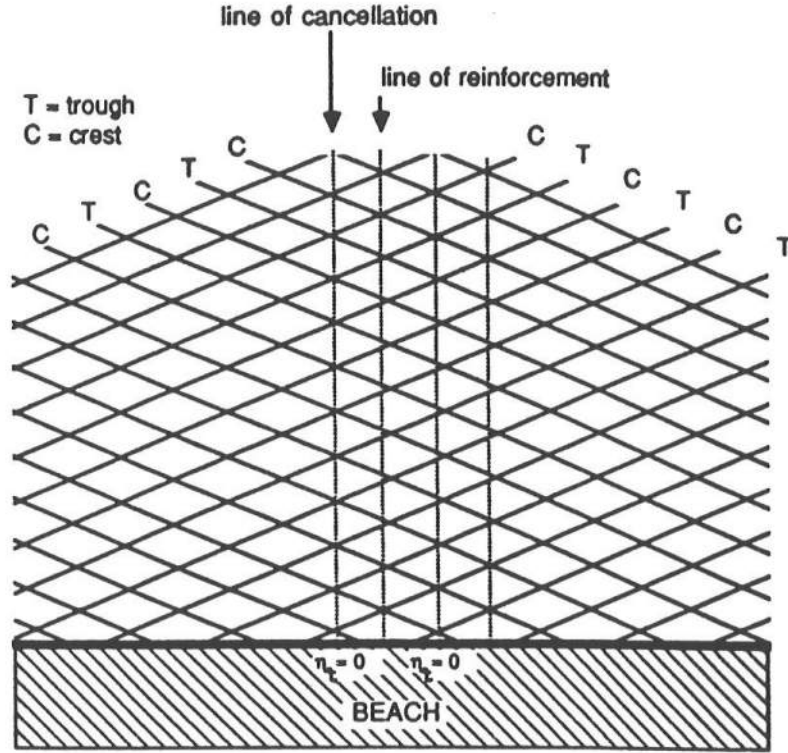
Figure 3.6: Theoretical incident wave field showing intersection of two wave trains and the resulting lines of reinforcement and cancellation.

but opposite angles of incidence, the lines of constant η_t, and hence the circulation cells, are perpendicular to the shoreline. Otherwise, the cells are slanted to the beach normal. Dalrymple predicted the longshore spacing of the rip currents by the equation

$$Lg_y = \frac{2\pi}{k_2 \sin\theta_2 - k_1 \sin\theta_1} \tag{3.40}$$

where θ_i = angle of incidence wave train, i=1,2

k_i = modulus of the wave number of the wave train, i=1,2

Dalrymple subsequently proved this rip current generation mechanism in a simple laboratory experiment where the two incident wave trains were formed by reflecting one generated wave train off a wall. He observed well defined rip currents on the beach, and found the measured longshore spacing of the rip currents agreed with the predicted value to within ±5%. Dalrymple and Lanan (1976) further demonstrated that the intersecting

wave trains and associated rip currents provided suitable conditions for the evolution of beach cusps. The apices, or horns, of the cusps formed at the points where the rip currents flowed offshore. The measured longshore spacing of the rip currents, and hence the cusps, again agreed very well with the predicted values.

3.4.2 Migrating Rip Currents

Returning to the general case where there are two incident wave trains with $\omega_1 \neq \omega_2$, it is seen from equation 3.29 that the longshore speed of propagation of the wave envelope is no longer zero. Consequently, the lines of constant η_t in the wave field are not stationary. Since it is recognised that rip currents can develop in the surf zone where stationary nodal lines intersect the beach, it is now proposed that, for small Cg_y, i.e., small longshore speeds of wave envelope propagation, rip currents will develop and move slowly along the beach as the nodal lines migrate through the wave field.

In order to *predict* suitable wave field conditions leading to the generation of migrating rip currents, it is preferable to have a general, dimensionless expression for Cg_y. Instead of requiring Cg_y to have an absolute value, we can now require Cg_y to be small with respect to another important wave parameter, thus enabling a broad assessment of various dimensionless wave field conditions. The expression for the longshore speed of propagation of the wave envelope (equation 3.29) is therefore divided by $C_2 = \omega_2/k_2$, the celerity of the second wave train,

$$\frac{Cg_y}{\omega_2/k_2} = k_2 \left(\frac{\omega_1}{\omega_2} - 1 \right) \frac{k_1 \sin \theta_1 - k_2 \sin \theta_2}{k_1^2 + k_2^2 - 2k_1 k_2 \cos(\theta_1 - \theta_2)} \tag{3.41}$$

To reduce the number of variables on the right-hand side of the above expression, shallow water conditions are assumed,

$$\frac{\omega_1}{\omega_2} = \frac{k_1}{k_2}$$

and the ratio of the two wave numbers, $k_r = k_1/k_2$, is defined. Through algebraic manipulation, equation 3.41 can be rewritten as

$$\frac{Cg_y}{C_2} = \frac{(k_r - 1)(k_r \sin \theta_1 - \sin \theta_2)}{k_r^2 + 1 - 2k_r \cos(\theta_1 - \theta_2)} \tag{3.42}$$

which is a quadratic equation in k_r. This equation can be solved for k_r for given values of Cg_y/C_2, θ_1 and θ_2.

Graphical representation of equation 3.42 is presented in figure 3.7 for the case where θ_1 is fixed at $+10°$. The angle of incidence of the second wave train, θ_2, varies along the vertical axis, and the ratio of the two wave numbers, k_r, is represented on the horizontal axis. The lines plotted on the graph represent contours of Cg_y/C_2. The graph shows two families of solutions, one oriented vertically and the other horizontally. The latter of these two solution sets represents conditions when the nodal lines are propagating in the on/offshore direction, at large angles to the beach normal. These conditions do not lead to the development of rip currents on the beach, but instead create a surf beat effect. The vertically oriented family of solutions represent conditions when the nodal lines are oriented close to the beach normal and *do* lead to the development of rip currents. The vertical, dashed line depicts the conditions necessary for stationary rip currents. Values of $Cg_y/C_2 = \pm 0.2$ were arbitrarily selected as limits for the development of migrating rip currents. Within these limits, several test cases were selected for the experimental investigations in the laboratory.
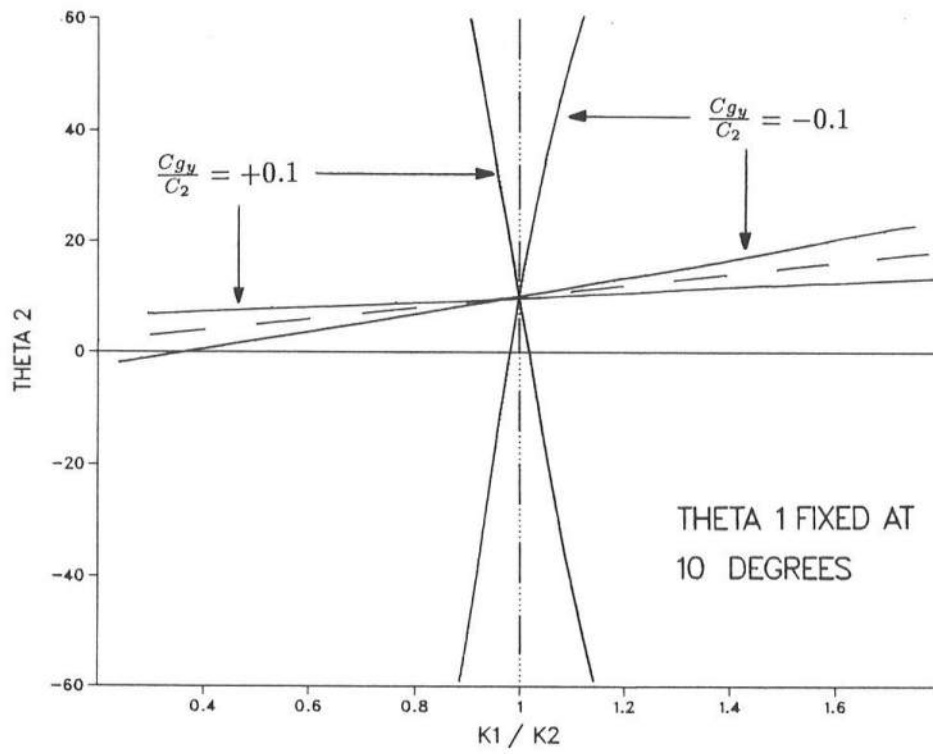
Figure 3.7: Graphical representation of equation 3.42, showing the incident wave conditions suitable for the development of migrating rip currents.

Chapter 4

EXPERIMENTAL FACILITIES AND DESIGN

4.1 Laboratory Facilities

The migrating rip currents were simulated in the University of Delaware's multi-directional, multispectral wave basin situated in the Ocean Engineering Laboratory. The basin measures 20 m by 20 m with a depth of 1.1 m. For the duration of the experimental work, the water depth in the basin was maintained at 81 cm $\pm$ 0.5 cm.

Installed along one wall of the basin is a segmented wavemaker, composed of thirty individually actuated paddles. The paddles are 0.51 m wide and have gaps between them of approximately 0.015 m. Water can flow freely behind and between the paddles. Each paddle is hinged 0.1 m above the floor of the wave basin and is driven by a 1 hp motor connected to a mechanical system of wires and pullies. The wavemaker can create any desired wave field from monochromatic waves to realistic 3-dimensional sea states. A Hewlett–Packard 1000 A700 mini–computer, with a real–time operating system, performs the dual functions of controlling the wavemaker and data acquisition. The computer sends paddle stroke information, in the form of voltages, to each paddle via thirty D/A channels. Paddle positions are specified every 0.2 s; this signal is then smoothed to provide an analogue input to the wavemaker. The wave basin is equipped with forty A/D channels used to collect data from any instrument with an analogue output voltage over the range of ± 10.24 V. Further, more specific details of the wavemaker system can be found in Harkins (1991).

For the purpose of the experimental work described herein, a wooden beach, 14.65 m in length, was installed in the wave basin opposite the wavemaker. This provided an idealized planar slope of 1:10 from elevations $+12.0$ cm to -38.5 cm with respect to a

reference level, SWL = 0 cm, changing to a slope of approximately 1:1 from -38.5 cm to -81.0 cm, the bottom of the tank. A schematic plan and cross–section of the wave basin, including the beach, is presented in figure 4.1.

The wave generation programs, which will be described later, required closed basin conditions, i.e., the wavemaker and beach extending across the full width of the tank, and reflecting side walls. As the beach (and wavemaker) did not extend across the full width of the wave basin, a temporary wall was built perpendicular from the wavemaker to the end of the beach. This reduced the number of paddles available for wave generation from 30 to 27. In an attempt to reduce large scale circulations in the basin during the experiments, manifestations of the finite width of the tank, part of the wall was removed along the upper third of the beach, see figure 4.2. All the experimental test cases were designed so that the underlying longshore current flowed towards and through this gap in the wall. This reduced the volume of flow reflected back towards the wavemaker, or along the beach, by the side wall, which could distort the nearshore circulation system.

All the instruments used for data collection were mounted on a metal framework, which straddled the beach. Data collection was restricted to the central portion of the beach to further avoid any adverse effects of the side walls on the circulation system.

4.2 Instruments for Data Collection

Wave height and direction information was acquired using an array of twin wire resistance wave gauges. The bias, gains, and windows of operation of the wave gauges were adjusted for use in the shallow water on the beach. The analogue output voltage from the gauges was in the approximate range of ± 10 V. Each wave gauge was connected to an A/D channel and data were sampled at a specified rate by the HP computer. The wave gauges were calibrated three times during the 11 consecutive hours of wave data collection. Further details of the experimental procedures used when collecting wave data are presented in the following chapter.

Longshore and cross–shore velocity data were collected using two Marsh–McBirney, model 523M, electromagnetic (EM) current meters. Each current meter is equipped with
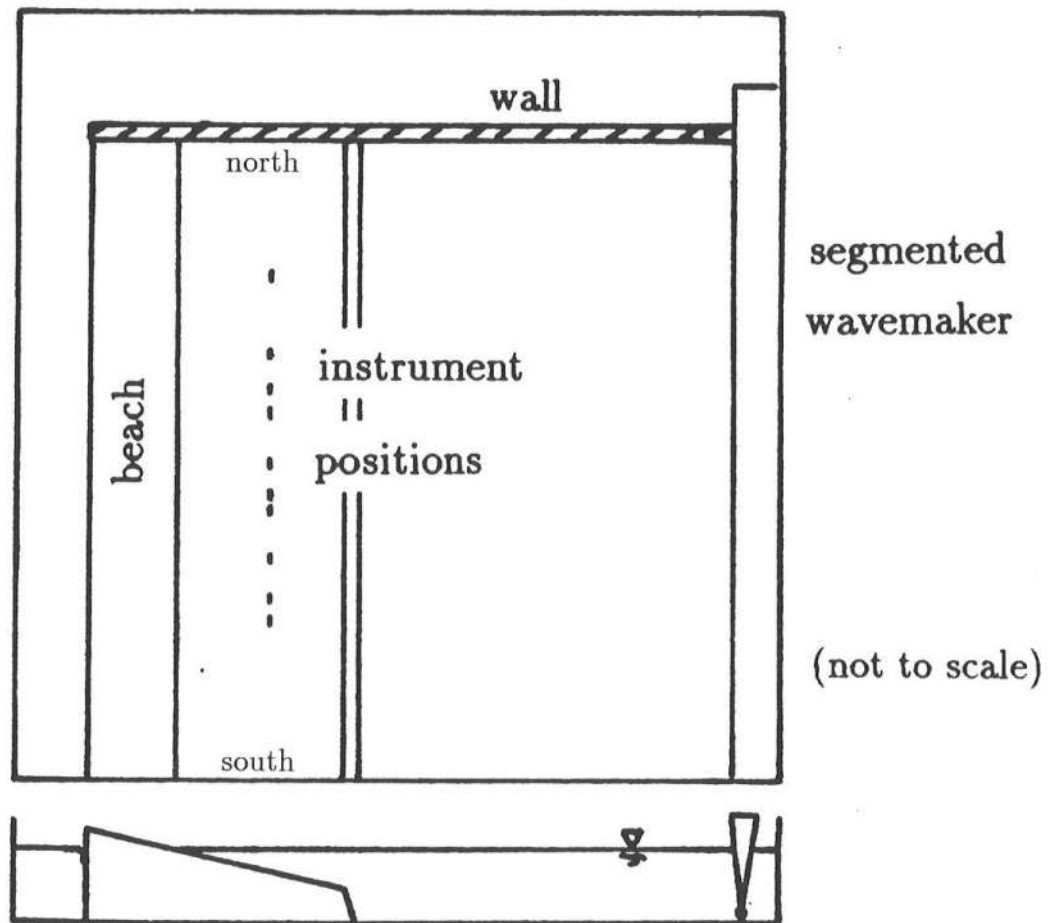
Figure 4.1: Schematic plan and elevation of the directional wave basin at the University of Delaware.
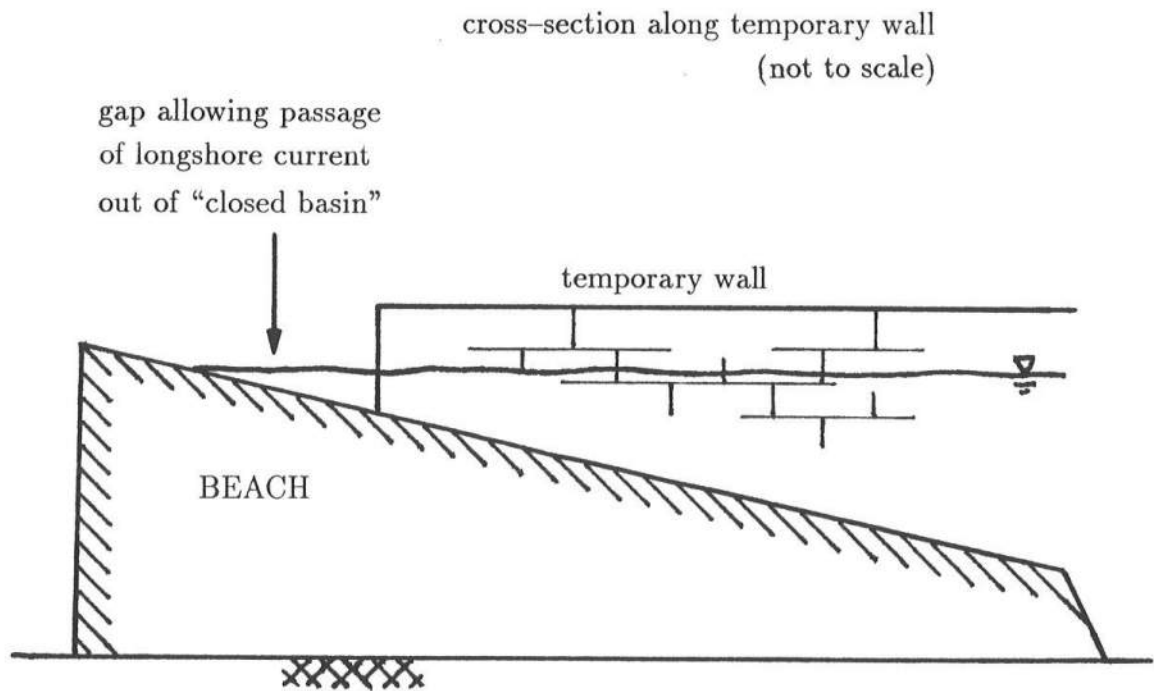
Figure 4.2: Details of the temporary wall at its abutment to the end of the beach.

a solid–state electromagnetic sensor and a signal processor. The sensor, mounted at the end of a rod, is spherical with two pairs of orthogonally protruding electrodes. The model 523M current meter has a 1 cm diameter sensor. The current meters were connected to AC power and grounded to minimize electrical noise. Some noise was picked up from the wavemaker, but it did not significantly impair the data from the current meter sensors.

The current meter operation is based on Faraday's principle of electromagnetic induction. When the current meter is in operation, an electromagnetic field is generated around the sensor, parallel to the longitudinal axis of the sensor. Water (an electrical conductor) flowing in a plane normal to the magnetic field induces voltages. The electrodes detect these voltages and send them to the signal processor. The voltages are linearly proportional to the water velocity. If the current meters are positioned with the electrodes oriented along the previously defined x and y axes, then the horizontal components of cross–shore and longshore velocities can be measured.

The signal processor is equipped with meters giving direct readings of x and y velocities, but for the purpose of these experiments, their analogue output was fed to the A/D channels (one channel each for longshore and cross–shore velocity per instrument) and sampled at a specified rate by the HP computer. The current meters have a range of approximately ± 1 V $= \pm 3.00$ m/s, but typical voltages/velocities measured during the experiment were in the range ± 0.1 V $= \pm 0.30$ m/s.

Both current meters (S/N 9071/$WE\,27$ and S/N 10195/$WE\,62$) were equipped with low-pass, analogue filters which provided selective signal improvement by attenuating high frequency noise. The filters installed in both the instruments had time constants of 0.1 s which provide a 3 dB bandwidth of 1.59 Hz. Therefore, frequencies of 1.59 Hz and greater (periods < 0.6 s) would be attenuated. The choice of such a small time constant allowed recording of unattenuated signals over the whole range of oscillatory flows generated during the experiments in the directional wave basin. Current meter S/N 9071/$WE\,27$ was also fitted with an enhanced low velocity capability option which lowered noise levels and provided a more stable zero.

The HP computer is equiped with a HP12060A analogue input card which is programmed to read voltages in the range of ±10.24 V with a resolution of 5 mV. This degree of resolution was considered too small for reading voltages from the current meters which were in the range ±100 mV. One solution to this problem was to re–set the input card to its maximum resolution of 0.625 mV, but then the full scale range of the card would have been only ±1.28 V, too small to record data from the wave gauges which had an output range of ±10 V. Instead, it was decided to use a simple electronic amplifier system which multiplied the current meter signals by 35 before they were read by the computer. It should be noted here that the amplifier system also reversed the sign of the current meter voltages. Both this and the amplification were reversed before the data analysis was performed.

4.3 Calibration of Current Meters

Although details of static calibration tests for the electromagnetic current meters are provided by the manufacturers, Marsh-McBirney Inc., it was decided that *dynamic* calibration checks should be made. The static calibration tests performed by the manufacturers are conducted using unidirectional, recirculating flow facilities. In contrast, we wished to calibrate the instruments in an oscillatory flow in order to examine their response to changes of current magnitude and direction.

The current meter calibration experiments were conducted in the Department of Civil Engineering's tow tank at the University of Delaware. The tow tank is 30 m long, 2.5 m wide and 1.5 m deep, with a hydraulically driven, piston-type wavemaker at one end and an arrangement of wave absorbers at the other end. Electrical noise was minimized by grounding the signal processor to the AC mains supply outlet casing. For the duration of the calibration experiments the depth of water in the tow tank was 0.6 m. The output voltage from the current meters was calibrated against velocity readings from a laser doppler anemometer. The laser doppler anemometer (LDA) was a DANTEC 100 mW Argon laser equiped with a fiber optic probe. During the course of the calibration experiments one of two sets of laser beams was used, having wavelengths of either 514.5 nm

(green beam) or 488.0 nm (blue beam). The focal length of the laser beams was 66.59 mm, and their separation was 8.0 mm.

Each current meter was individually calibrated against the LDA. The fiber optic probe and the current meter sensor were aligned in the same cross–tank plane, perpendicular to the wavemaker. The horizontal and vertical laser beams emitted from the fiber optic probe were used to ensure accurate alignment of the current meter probe. Initially, the laser probe was lowered to the water surface and adjusted so that the horizontal beams projected across the water surface and were level with the water line on the side of the tank. The laser probe was then submerged to a depth of approximately 0.15 m. The current meter sensor was mounted vertically in the tow tank, beyond the focal point of the laser beams, and submerged to the same depth. It was then adjusted so that the two horizontal laser beams intersected the upstream and downstream electrodes, and the top vertical beam intersected the stem of the current meter sensor. The depth of submergence of the two probes was chosen to ensure that they were not exposed when the trough of a wave passed.

Calibration data was required over the whole range of wave frequencies that would be encountered later in the directional wave basin. To achieve this, a series of deep water breaking waves were generated in the tow tank. Each breaking wave was formed from 33 component waves of varying frequencies which propagated down the tank at correspondingly varying speeds before all arriving at a specified location, X_b, at one point in time, to form a breaking wave. By generating such a spectrum of waves, the LDA and EM current meter were able to record water velocities over a specified frequency range at one time. This method was therefore quicker than running single wave train tests at many different frequencies.

Each wave train that was generated had a specified central frequency, f_c, and band width, Δf. The 33 component waves each had a frequency within this band width. The sampling frequency, f_s, used for data collection was either 50 Hz or 100 Hz. Full details of each calibration experiment are presented in Appendix A. For each calibration test, records of 14336 (7×2^{11}) data points were collected from the current meter and the LDA

simultaneously. This data was then band averaged and passed through a fast Fourier transform (FFT).

The calibration parameter for each current meter, in each direction, was measured as a function of frequency and given by

$$c(f) = \frac{|\text{FFT(velocity record from LDA)}|}{|\text{FFT(voltage output record from current meter)}|}$$

According to the manufacturer's (static) calibration tests, this constant should be,

$$c = 3.00$$

$$\text{or, } \pm 1\text{V} = \pm 3.00\text{m/s}$$

over all unattenuated frequencies. A graph of calibration parameter vs. frequency was plotted for each calibration run and the values within the specified band frequency of that run were extracted. The data outside of this range were discarded because they would not provide a true representation of the calibration parameter. (The current meters and the LDA were fitted with different filters so the current meters started to attenuate the input signal at a lower frequency than the LDA.) For both the x and y axes on each current meter, the selected data points from each calibration run were passed through a least squares fit routine to produce a calibration curve. All four calibration curves are presented in Appendix A.

The calibration curves should have been applied to the current meter voltage output signals in the Fourier domain, as the calibration parameters were dependent on frequency. However, the calibration curves closely approximated horizontal, straight lines, indicating, as the manufacturers suggest, a calibration *constant* of ≈ 3.00. Therefore, for each current meter, in each direction, the value of the calibration parameter at the approximate frequency of the migrating rip current cells was selected as the calibration constant.

4.4 Wave Generation Program

All the wave generation programs previously used in the directional wave basin have been based on wavemaker theory which assumes the basin and wavemaker are of infinite length, and the water is of constant depth. This is adequate for generating waves

with normal incidence or when performing experiments in the middle of the basin, not too distant from the wavemaker. However, when waves are generated at an angle, the wave field far from the wavemaker becomes contaminated by reflection of the generated wave from one side wall, and diffraction in the region adjacent to the opposite side wall. This is illustrated in figure 4.3. Consequently, the wave field in the nearshore region does not resemble that which was required.

As the nature of the incident wave field is very important for the proposed generation of migrating rip currents, it was considered necessary to eliminate the problem of wave field contamination. Therefore, a new wave generation program was developed, based on Dalrymple's (1989) "designer waves" wavemaker theory. This new theory accounts for reflection from the side walls, diffraction, and shoaling over a non–constant depth bottom. It provides a clean wave field across the entire width of the basin, at any desired location, X_m. Once the required wave field and location have been specified, it is propagated back to the wavemaker, thereby providing the paddle stroke information. Figure 4.4 repeats the wave conditions of figure 4.3, but with the clean wave field specified at the beach. A computer program based on this designer wavemaker theory was developed for use with the rip current experiments. Although the program has not been extensively tested in the laboratory, it does appear, on visual inspection, to give good results.

BEACH

WAVEMAKER

Figure 4.3: Regular wavemaker theory: instantaneous water surface elevations for a planar, monochromatic wave train with a 30° angle of incidence. (Fig. 2 of Dalrymple, 1989.)
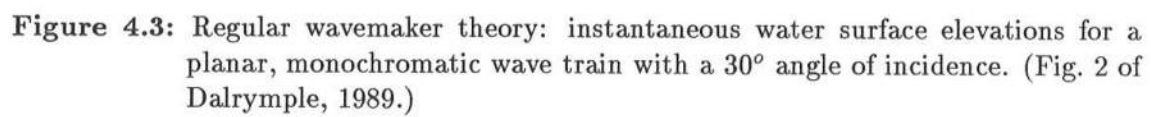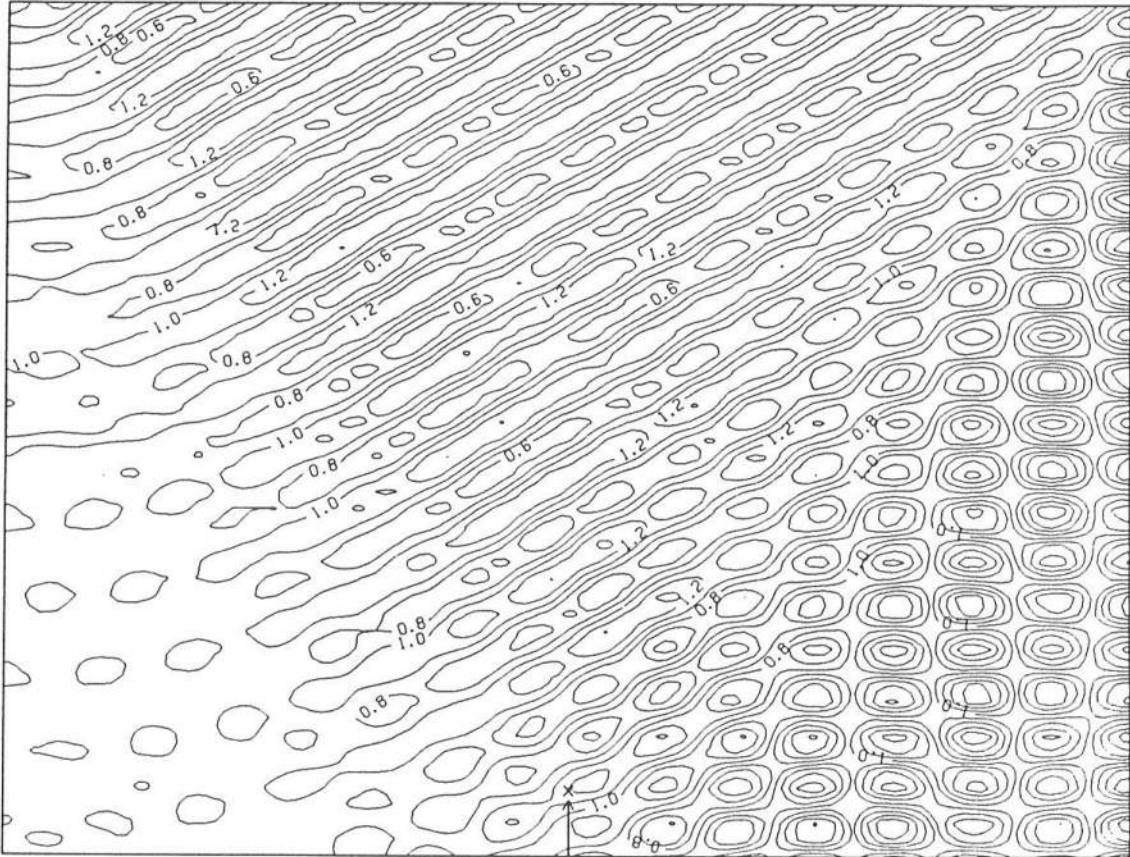
BEACH

WAVEMAKER

Figure 4.4: Designer wavemaker theory: instantaneous water surface elevations for a planar, monochromatic wave train with a 30° angle of incidence and $X_m =$ beach. (From fig. 2 of Dalrymple, 1989.)

Chapter 5

EXPERIMENTAL TEST CASES AND PROCEDURES

5.1   Current Meter and Wave Gauge Locations

For each rip current system investigated in the laboratory, wave heights and cross–shore and longshore current velocities were measured at various positions in the nearshore region. The cross–shore and longshore velocities were measured at selected locations which formed a ten–point linear, longshore array. The minimum distance between instruments in a linear array, to avoid aliasing problems, is governed by

$$\text{minimum separation distance} \leq \frac{\text{smallest wavelength to be measured}}{2} \qquad (5.1)$$

For the experiments described herein, the rip cell lengths were expected to be in the range of $3 - 8$ m, so the minimum separation distance was required to be ≤ 1.5 m. However, the total length of the array was restricted to the length of the instrument support framework, which was approximately 7 m. As a result, the minimum separation distance of any two points in the array was set at 0.08 m, well within the limit to resolve the rip current cells and, if necessary, the incident waves. The configuration of the ten–point array was obtained from Leech (1956), and is illustrated in figure 5.1. Note, the x–axis (on/offshore axis) passes through the first instrument location.

The experimental test cases were divided into two sets. For the first set, the current meter array was located 1.69 m offshore and centered approximately halfway along the beach. For the second set of experiments, the array was located closer to the breaker line at 0.975 m offshore, and displaced 0.81 m towards the temporary wall. This second adjustment was made to avoid inconsistencies in the incident wave field, caused by the restricted circulation near the side wall, which were observed to be stronger at the southern

39

unit spacings between instruments
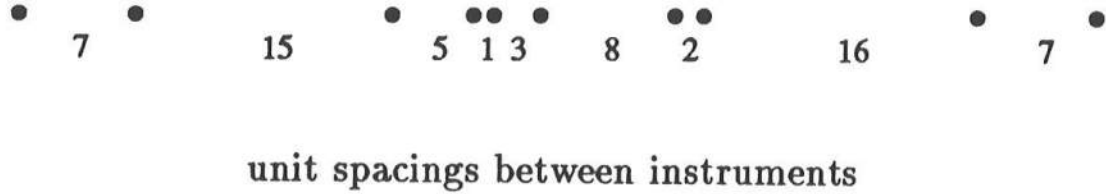
Figure 5.1: Optimal configuration for a ten–point linear array as proposed by Leech (1956).

end of the beach. Details of the current meter array locations on the beach are presented in figure 5.2.

To obtain information about the heights and directions of the incident waves, the wave gauges were arranged in a three–point linear, longshore array with the configuration shown in figure 5.3. The minimum incident wave length expected to be measured was 0.8 m, so the minimum gauge separation distance, according to equation 5.1, was set at 0.4 m. The wave gauge array was located within the current meter array so that one wave gauge and current meter position were colocated. This enabled direct comparison of current and wave data at one location. The wave gauge locations are indicated in figure 5.2 by the symbol "WG". The wave gauge array locations were displaced with the current meter locations for the second set of experiments.

5.2   Experimental Test Cases Selected

Initially, four experimental test cases were selected and run in the wave basin. As the results from these were analysed, it was decided to select and run a second set of experiments. Details of the first four test cases are presented in table 5.1. The vector

41

Figure 5.2: Current meter and wave gauge locations in the directional wave basin for the first and second set of experimental test cases.

BEACH

SWL

N1 N2
4.44 m to wall of wave basin
0.56 m
1.20 m

N3
N4 N5
N6
N7 N8
WG
WG N9
N10
WG

0.08 m
1.52 m
0.16 m
0.80 m
0.40 m
0.80 m
0.56 m
1.28 m

L1 L2
5.25 m to wall of wave basin
0.56 m
1.20 m

L3
L4 L5 L6
L7 L8
WG L9
L10 WG
WG

0.08 m
1.52 m
0.16 m
0.80 m
0.40 m
0.40 m
0.56 m
0.80 m
1.28 m

1st set of experiments: depth of current meters = 15.5 cm

    water depth = 17 cm

    locations L1 – L10

    1.69 m offshore

2nd set of experiments: depth of current meters = 6.8 cm

    water depth = 9.8 cm

    locations N1 – N10

    0.98 m offshore

(approx. to scale)

●　　　　　　　　　　●　　　　　　　　　　　　　　●

1　　　　　　　　　　　　2

unit spacings between instruments

Figure 5.3: Optimal configuration for a three–point linear array.

diagrams provide an idea of the direction of the incident wave trains. The direction of propagation of the wave envelopes, and hence the rip current cells, is also indicated.

The first case, QTEST, was selected because it has a slow speed of propagation; the ratio Cg_y/C_2 was small. Representation of the incident wave conditions for this test case on the graph predicting the theoretical values of Cg_y/C_2 is shown in figure 5.4. As for all the experimental test cases selected, the height of the individual wave trains was specified in terms of paddle stroke voltage. Therefore, it should be noted that for two wave trains of equal paddle stroke voltage but different frequencies, their wave heights will be slightly different.

The second and third test cases, RTEST and PTEST, have higher values of Cg_y/C_2 and therefore, the rip currents are expected to migrate faster along the beach. These two test cases are identical except for their paddle stroke lengths and hence wave heights. PTEST was selected in order to observe the differences in the rip currents due to larger wave heights. These two cases are represented graphically in figure 5.5. Finally, the fourth test case, STEST, is particularly interesting because the wave envelope theoretically propagates in the opposite general direction to that of the incident wave trains, both of

Table 5.1: Details of the first set of four experimental test cases.

RTEST & PTEST	QTEST	STEST
$\theta_1 = +3.0^\circ$ $\theta_2 = -10.0^\circ$ $k_1 = 5.51$ m^{-1} $k_2 = 5.70$ m^{-1}	$\theta_1 = +10.0^\circ$ $\theta_2 = -1.0^\circ$ $k_1 = 5.89$ m^{-1} $k_2 = 6.01$ m^{-1}	$\theta_1 = -10.0^\circ$ $\theta_2 = -30.0^\circ$ $k_1 = 5.72$ m^{-1} $k_2 = 5.89$ m^{-1}
$Cg_y/C_2 = -0.15$ (predicted)	$Cg_y/C_2 = -0.10$ (predicted)	$Cg_y/C_2 = 0.08$ (predicted)
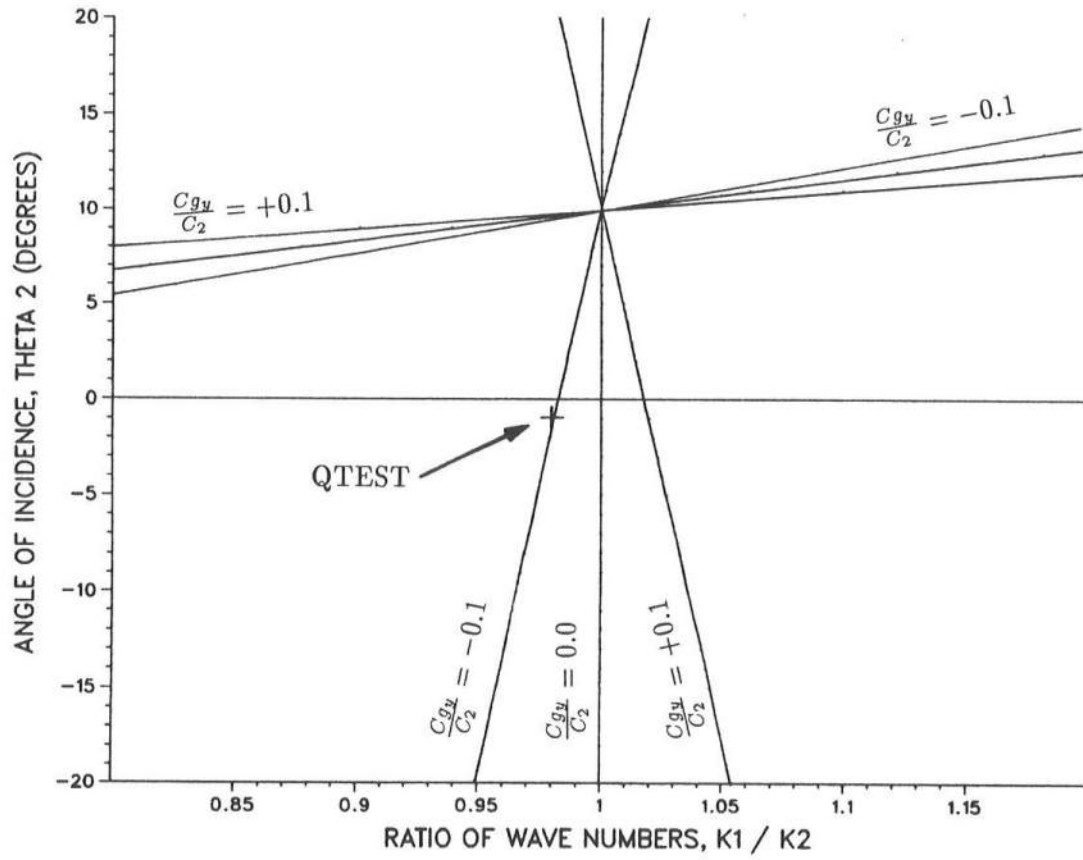
Figure 5.4: Theoretical incident wave conditions selected for experimental test case QTEST.

which have negative angles of incidence (with reference to the coordinate system defined in chapter 3, figure 3.1). This test case is represented in figure 5.6.

Care was taken in selecting each of these four experimental test cases to avoid incident wave conditions that would engender edge waves. Each case was checked using the edge wave dispersion relationship from Bowen and Guza (1978),

$$\sigma_e{}^2 = |\sigma_1{}^2 \sin \alpha_1 - \sigma_2{}^2 \sin \alpha_2| \sin(2n + 1)\beta \tag{5.2}$$

where σ_e= frequency of the generated edge wave

$\quad\quad = \sigma_1 - \sigma_2, \quad\quad\quad$ for $\sigma_2 > \sigma_2$

σ_1= frequency of the first wave train

σ_2= frequency of the second wave train

α_1= angle of incidence of the first wave train

α_2= angle of incidence of the second wave train

β = slope of the beach

n = mode number of the edge wave, $\quad\quad n = 0, 1, 2 \cdots$

(NB. The definitions above do not follow the same coordinate system as used in chapter 3.) The results of the edge wave resonance checks for each of the four test cases in the first set of experiments are presented in Appendix B.

The second set of experimental test cases was based on PTEST. A summary of these test cases is presented in table 5.2. Note that the clean wave field for these cases was required to coincide with the new location of the instrument arrays. P2TEST is identical to PTEST but, because the current meter array was closer inshore, the longshore and cross–shore velocities were measured much closer to the breaker line and were therefore expected to be higher. This case provided a comparison with PTEST, enabling evaluation of the features of a migrating rip current system at different distances offshore.

Following on from P2TEST, the robustness of the migrating rip current generation was investigated by introducing random waves into the incident wave field. Both P2RAND and P2DIRAND consist of random waves superimposed on the incident wave field for P2TEST. The nature of the random waves was based loosely on a TMA spectrum
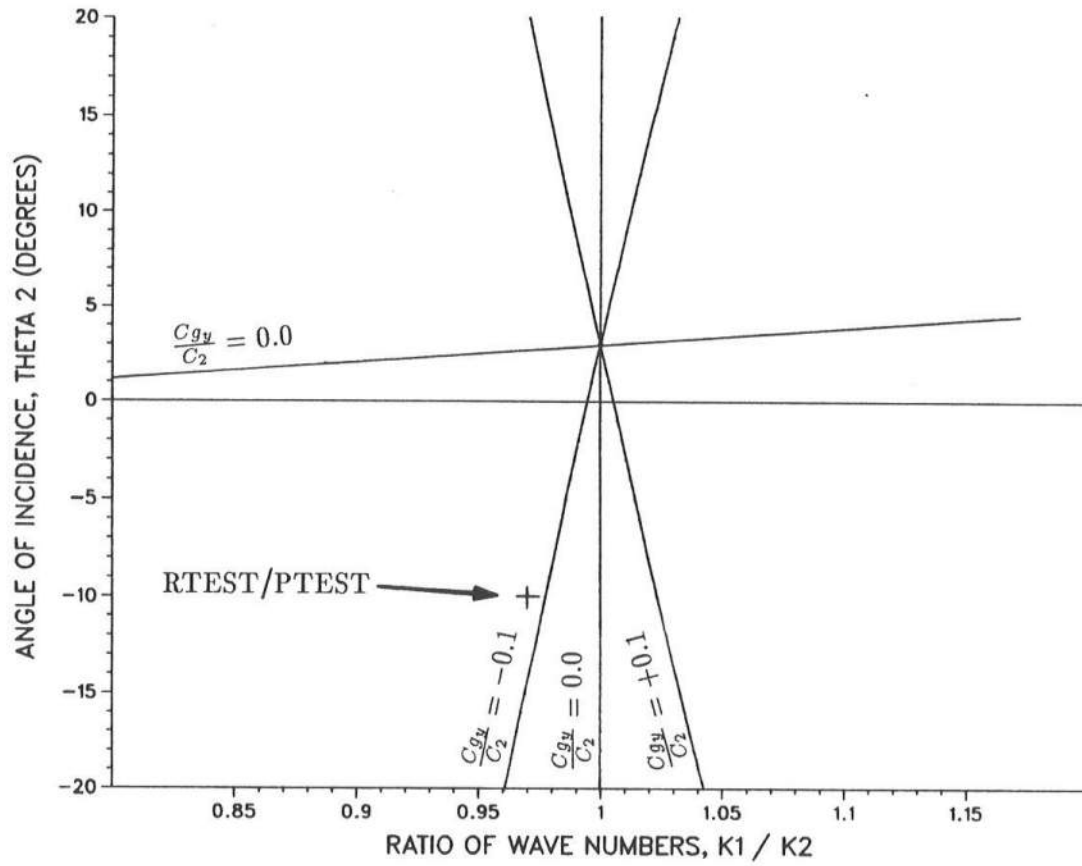
Figure 5.5: Theoretical incident wave conditions selected for test experimental cases RTEST and PTEST.
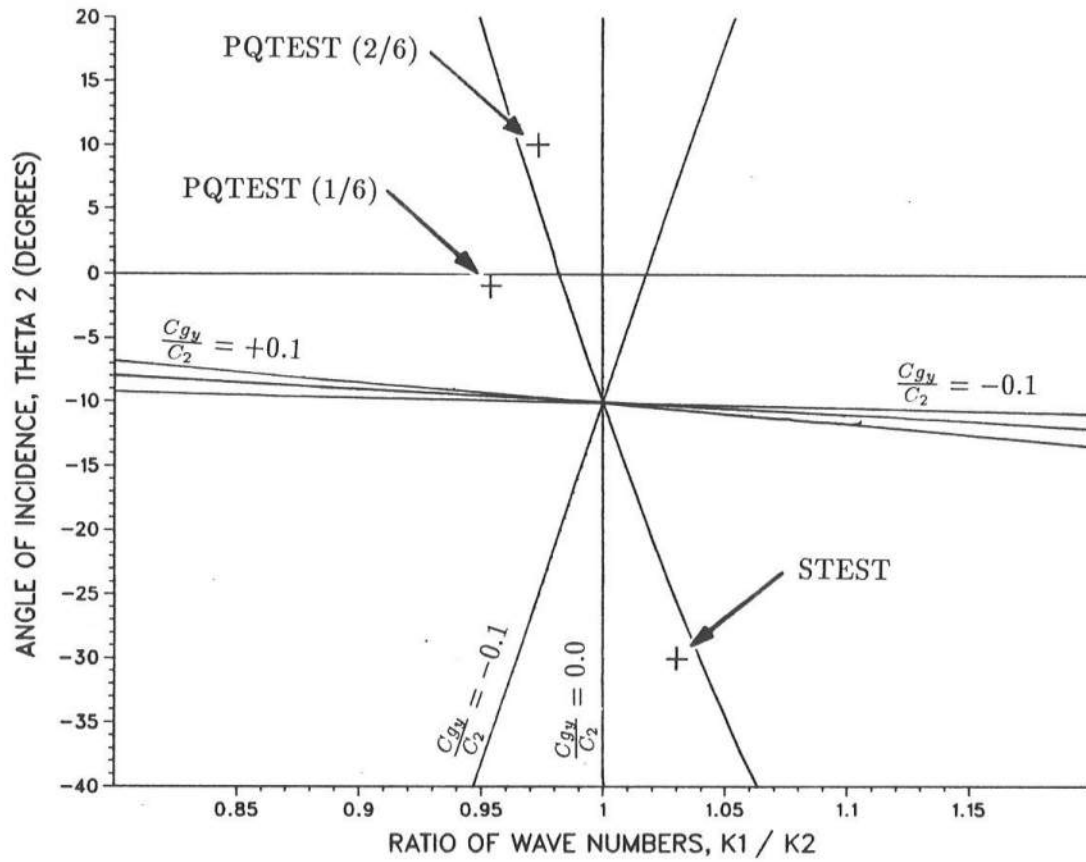
N.B. The order of the wave trains has been reversed for STEST to enable representation on this graph. The value of Cg_y/C_2 will be the same.

Figure 5.6: Theoretical incident wave conditions selected for experimental test cases STEST and PQTEST(i).

Table 5.2: Summary of the second set of four experimental test cases.

Experimental Test Case	Description
P2TEST	identical to PTEST in previous set
P2RAND	P2TEST + random waves with frequency spread, no directional spread, random phases
P2DIRAND	P2TEST + random waves with frequency spread and 12° directional spread about each of the two main wave trains, random phases
PQTEST	direct superposition of PTEST and QTEST

with peak frequencies, and in the case of P2DIRAND, peak directions, identical to the frequencies and directions of the two incident wave trains in P2TEST. The random waves were developed using a computer program provided by the U.S. Army Engineer Waterways Experiment Station's Coastal Engineering Research Center (CERC), and based on a method which is discussed in Vincent and Briggs (1989). For P2RAND, the random wave field had 16 components in each of the two P2TEST directions, with no directional spread. The periods of the component waves varied from 1.6 s to 1.02 s (the periods of the two wave trains in P2TEST were 0.97 s and 1.00 s), with the longer period waves having smaller wave heights. The experimental test case P2DIRAND consisted of a total of 26 component waves over a range of frequencies, and with a directional spread of 12° about the direction of propagation of the main wave trains in P2TEST. Details of the component waves for P2RAND and P2DIRAND are in Appendix C and sample wave spectra measured by one of the wave gauges during these two experiments are presented in Appendix D. The measured spectra provide information on the levels of energy in the incident wave field due to the random waves and the two main wave trains.

The final experimental test case, PQTEST, is a direct superposition of two previous cases, PTEST and QTEST. This case was selected to enable observation of the interaction of two proven rip current systems. However, the superposition of two pairs of wave trains leads to other interactions giving a total of six possible rip current systems as defined by equation 3.42 in chapter 3. These are represented in figures 5.6, 5.7 and 5.8 which provide an indication of the different rip current systems that developed in the wave basin. However, it can be seen that some of the predicted rip current systems lie in the horizontal family of solutions, and therefore, have nodal lines approximately parallel to the beach, producing a surf beat effect in the nearshore region. The checks for edge wave generation for each of these different interaction cases are presented in Appendix B.

5.3 Experimental Procedures

Each of the previously described experimental cases was run through the wave generation program, DESIGNPLUS, to create the voltage input files which define the motions of the paddles. The wave train parameter input files for each test case are presented in Appendix C. The voltage input files have a limited length of 1500 lines, which corresponds to 5 minutes of wave generation in the wave basin. Data records of 4096 points were required, and the data sampling frequency, f_s, was set at 10 Hz. Therefore, wave generation of at least 6 minutes and 50 seconds was required, making repetition of the voltage input file necessary at least once for each experimental run. In order to have a smooth transition at the record repeat, the period of the rip cells passing a fixed point on the beach was estimated from preliminary experiments, and input record lengths were generated for a integer number of these periods. For example, the rip current period for QTEST was estimated as 58 s: multiplying by five gives 290 s, or 4.83 mins., which corresponds to an input record length of 1450 lines. This process ensured a relatively smooth transition from the end of the voltage input file back to the beginning, minimizing discontinuity disturbances in the wave field.

The length of the voltage input file was restricted by the available Random Access Memory (RAM) in the HP computer. Similarly the maximum number of data points that could be obtained (which were required to be a power of 2 for the Fourier analysis) was
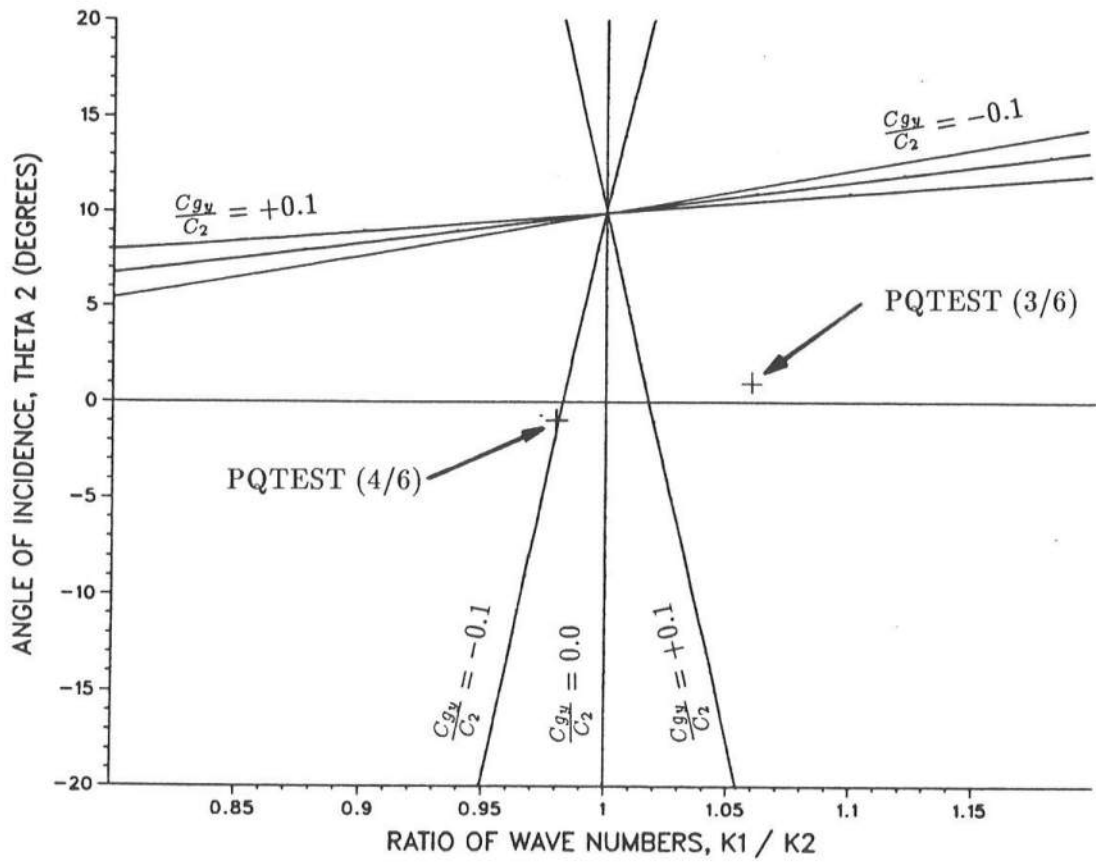
Figure 5.7: Theoretical incident wave conditions selected for experimental test case PQTEST(ii).
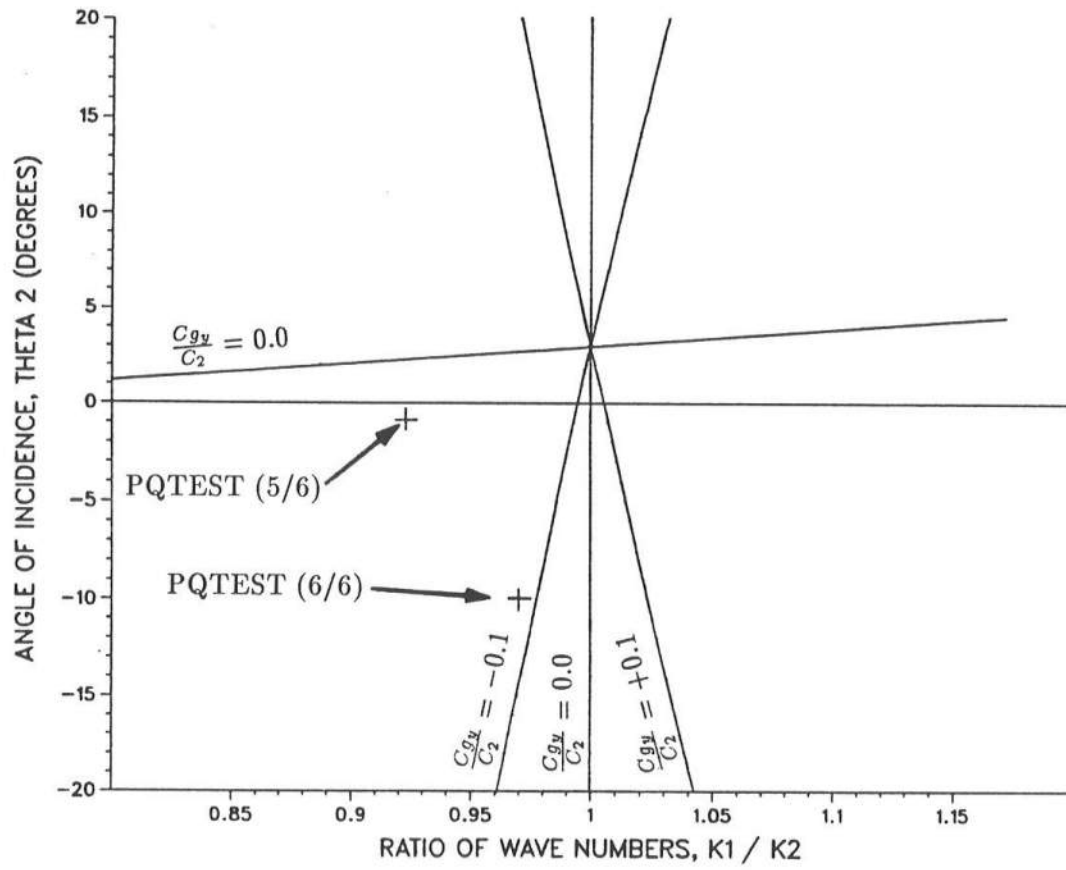
Figure 5.8: Theoretical incident wave conditions selected for experimental test case PQTEST(iii).

4096. The sampling frequency of 10 Hz was restricted by the speed of execution of the wavemaker control programs.

The wavemaker is controlled by the suit of programs: RTMAIN, WAVEP, DATAC and STOP. The wavemaker is run by invoking RTMAIN which controls all the timing and prompts the user for input and output file names, the sampling frequency, and the number of data points required. In turn, RTMAIN calls WAVEP, the paddle control program, every 0.2 s, and DATAC, the data collection program, every 0.1 s (10 Hz). STOP is a short program which halts wave generation and returns all the paddles to their central positions. It can be invoked from the keyboard at any time, but is also automatically called by RTMAIN once the required number of data points have been collected. RTMAIN calculates the time at which WAVEP and DATAC should be called, but if it does not reach the calls to these two programs by the specified times, it will suspend itself and wave generation in the basin will cease. The speed of execution of the control programs therefore governs the maximum frequency at which data can be collected. An additional concern is the time taken for WAVEP to get back to the beginning of the input voltages record once it has been exhausted. If this is not achieved fast enough, a glitch occurs in the paddle motion, or wave generation may cease altogether. Many of the experimental runs had to be repeated because RTMAIN suspended itself, or glitches occurred at the record repeat. This happened on an infuriatingly and illogically inconsistent basis, and the reasons for the inconsistency are as yet unknown.

It has previously been stated that velocity measurements were required at ten different locations along the beach for each experimental case. However, it has also been mentioned that only two current meters were available to make these measurements. Consequently, it was assumed that each experimental run was perfectly repeatable and the current meters were placed at two locations on the longshore array per run. Each test case then had to be run five times in order to obtain data from all ten points. Confidence in the repeatability of the experimental runs was based on several facts. Firstly, the input voltage file sent to the paddles was identical for each run, so theoretically, the paddle motions were identical for each run. Secondly, because one computer controls both the

wavemaker and data acquisition, the data collection began at exactly the same time after generation of waves had started (30 s) for each experimental run. Finally, a minimum of 20 minutes was left between each experimental run to allow water circulations in the wave basin to die. This ensured the initial conditions for each run were identical. Assessment of the repeatability of the experimental runs was made using data from each of the two current meters; the findings are reported in the following chapter.

The sequence of current meter locations along the beach at which measurements were made was (1,2), (3,4), (5,7), (6,8) and (9,10). This was arranged so that data were not recorded at locations 6 and 7 simultaneously. It was thought that a separation distance between the two current meters of only 24 cm might lead to interference between the two instruments. The current meters were positioned at a constant depth along the array. They were aligned using pencil grid markings on the beach and with a plumb–line. Once velocity measurements for a test case had been obtained at all ten array locations, they were amalgamated into one file as if data from all ten array locations had been gathered simultaneously. Each experimental case was run twice, providing a spare set of measurements in case any of the individual data files were bad.

The wave and current data were collected separately, although the facilities existed for recording information from up to 40 instruments simultaneously. The three wave gauges were calibrated in deep water and then mounted on the instrument framework. The gauges were calibrated before and after each set of experimental test cases. All the wave data were obtained in one day, the first set taking 6 hours and the second set taking 5 hours to complete. Calibration of each wave gauge was done by hand as the gauges were not fitted with step motors for computer controlled calibration. Each set of calibration data was passed through a best fit routine to produce a calibration curve. The curves from before and after each experimental test case set were then averaged to take account of any drift in the calibration of the wave gauges.

5.4 Data Analysis Procedures

All the experimental data sets were collected and stored on the HP computer in the Ocean Engineering Laboratory. They were then down loaded onto disks and transferred

onto the Department of Civil Engineering's SUN computer system on which all the analysis was performed.

5.4.1 Analysis of Current Meter Data

Initially, all the current meter data was passed through a routine which reversed the amplification process, dividing by 35 and inverting the signal. The individual records for each experimental test case at each location, in both longshore and cross–shore directions, were reviewed by plotting the velocity time series. Each time series was also passed through a Fast Fourier Transform (FFT) routine to enable review of its frequency spectrum. Any poor records, such as those affected by electrical noise or stronger than acceptable glitches at the time of the paddle input record repeat, were discarded. Finally, ten data records, one from each array location, were selected and amalgamated into one file. They were then analysed using either Barber's (1961) Direct Fourier Transform (DFT) method or the Maximum Likelihood Method (MLM), developed by Capon, Greenfield and Kolker (1967), to produce a wave number–frequency spectrum. In addition, the coherence between the primary and spare records from the P2TEST experimental test case, at two locations (one for each current meter), and in both the longshore and cross–shore directions, were performed to evaluate the repeatability of the experiments.

5.4.2 Analysis of Wave Gauge Data

As the wave gauge calibration curves are not linear, it was considered important to use only the necessary central part of the calibration data to obtain the calibration curve for each experimental test case. The minimum and maximum voltages in the wave gauge output files for each test case were found, and the calibration data beyond these values were discarded. The best fit calibration curve was then calculated. Once this had been accomplished, the calibration curves were used to convert the voltage output files into wave height files. The individual wave data files were then reviewed by plotting their time series and, for the one wave gauge that was colocated with a current meter, compared with their corresponding longshore and cross–shore velocity files. In addition, wave number–frequency spectra were calculated for each test case to compare the nature of the measured

incident wave field with that which was theoretically required. Incident wave directions were calculated from the wave number–frequency spectra, and were reviewed not only for comparison with the theoretically required wave direction, but also to provide some indication of the accuracy of the designer waves generation program.

Chapter 6

PRESENTATION AND DISCUSSION OF
EXPERIMENTAL RESULTS

6.1 Introduction

The experimental results and data analysis are presented and discussed in the order in which they were obtained in the laboratory, i.e., the first set of experimental test cases, QTEST, RTEST, PTEST and STEST, followed by the second set of experimental test cases, P2TEST, P2RAND, P2DIRAND and PQTEST. Visual observations, made for each test case, provide an initial impression of the effect of the incident wave field on the nearshore circulation system. These observations are reviewed before the analysis of the experimental data is presented. Example time series for cross–shore and longshore velocities, and water surface elevations for each case are presented and discussed along with the frequency spectra of the velocity records. Wave number–frequency spectra based on the cross–shore and/or the longshore velocity data are reviewed with reference to the low frequency motions in the nearshore region, whereas the wave number–frequency spectra based on the wave gauge data are used to check the incident wave conditions generated in the wave basin. Comparisons are made between the theoretically predicted rip currents and those observed in the laboratory. Finally, evaluations of the repeatability of the experimental runs are presented and discussed.

6.2 Experimental Test Case: QTEST

The incident waves for this first test case were breaking approximately 0.5–0.6 m offshore, in 5–6 cm depth of water, and were forming spilling or plunging breakers. Nodal lines (lines of constant $\eta_t = 0$) could be seen in the wave field at an angle close to the beach normal. The nodal lines were not straight in the nearshore region due to refraction. Rip

currents developed in the nearshore region soon after the leading edge of the generated wave trains arrived, and were located approximately at the intersection of the nodal lines and the beach. The rip currents migrated slowly to the northern end of the beach. Due to the length of the rip cells for this case, a maximum of only two were seen on the beach at any given time. The length of the rip cells was estimated at 6.5–6.7 m, and their period 58 s. The rip currents, although not very strong, were clearly visible and flowed approximately 1 m offshore before beginning to dissipate. The circulation within the rip cells was observed by injecting potassium permanganate (purple) dye into the water near the shoreline. As expected, the water at the shoreline flowed towards the nearest rip current. The dye also enhanced visual observations of the rip currents themselves.

The water surface elevation, cross–shore and longshore velocity time series from location L9 are presented in figure 6.1. (One of the wave gauges in the three–point linear array was colocated with the current meter at location L9.) Note that the longshore velocities have less than half the magnitude of the cross–shore velocities. All three time series, but in particular the longshore velocity time series, display a prominent low frequency modulation similar to that seen in the time series presented by Oltman–Shay, Howd and Birkemeier (1989), (figure 2.3). The low frequency modulation in the velocity records corresponds to visual observations of the time taken for one rip cell to migrate past a fixed point on the beach, i.e., the period of the rip cell. It is interesting to note that the groups in the cross–shore velocity record are double peaked, this is not seen in the other experimental test cases. There is a visible inconsistency in the cross–shore velocity record and the water surface elevation record at the time when the paddle input voltages file was repeated, at $t \approx 275$ s, although this is only a minor interruption and the general trend of the record is not significantly disturbed. As predicted by the theory, the groups in the cross–shore velocity and the water surface elevation time series are in phase. Also, the maximum longshore velocities approximately coincide with the nodes of the groups in the cross–shore velocity.

Frequency spectra of the cross–shore and longshore velocity time series are presented in figure 6.2. Both spectra clearly display significant energy at the incident wave
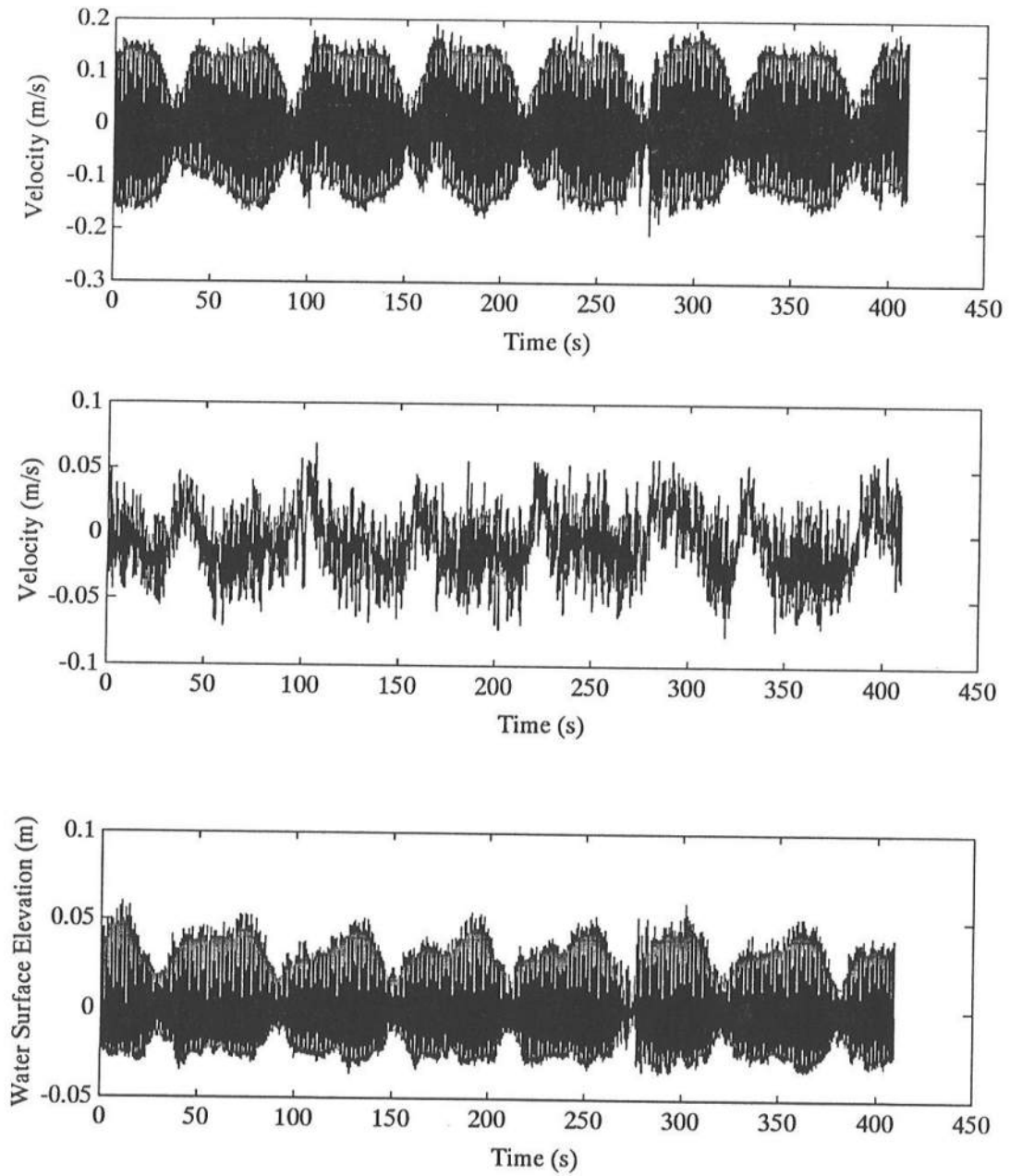
Figure 6.1: QTEST: time series of the cross–shore velocity (top), the longshore velocity (middle), and the water surface elevation (bottom) at location L9, current meter $WE\,62$.

frequencies, at approximately 1 Hz. The second harmonic of the incident wave frequencies is also evident in the cross-shore spectrum. In addition, both spectra show significant energy at low frequencies, at approximately 0.017 Hz. This corresponds to the observed periodicity of the rip cells for QTEST and the low frequency modulation in the time series, thereby proving that the low frequency energy in the spectrum is due to the incident wave groups and the migrating rip currents on the beach.

When all the current meter data for this test case had been reviewed, ten cross–shore files, one from each of the ten array locations, were amalgamated and analysed using the DFT method. This analysis method looks at the spatial lags at each frequency and calculates the energy at each lag. The sum of the energy over all the wave number bins at one frequency is equal to the total energy at that frequency as predicted by the 1–D frequency spectrum.

For this particular test case, the DFT analysis was performed using the full data set of 4096 points as one segment. Breaking the data into several segments and performing Bartlett averaging reduced the frequency resolution of the spectrum and distorted the results making them unclear. The low frequency portion of the wave number–frequency spectrum is presented in figure 6.3. Frequency is represented on the vertical axis, and longshore wave length, defined as $2\pi/L$, where L = longshore component of the wave length, is on the horizontal axis. Within this framework, contour lines of absolute energy are plotted. The contours are based on the maximum energy in the 1–D frequency spectrum. Only the top six out of ten contours have been plotted, the lower contours represent noise and exaggerate the spreading of energy over adjacent wave number bins, a disadvantage of using the DFT analysis method. The curved lines in figure 6.3 represent the theoretical edge wave dispersion relationship for modes 0, 1 and 2. For this case, one hundred frequency bins are shown, with Δf =0.00244 Hz, and, as for all the wave number–frequency spectra presented that are based on current meter data, the longshore wave number increment, Δk, is set at 0.1 m^{-1}.

The wave number–frequency spectrum reveals a strong concentration of energy at 0.0171 Hz $(7\Delta f)$ which corresponds to the visually observed and theoretically predicted
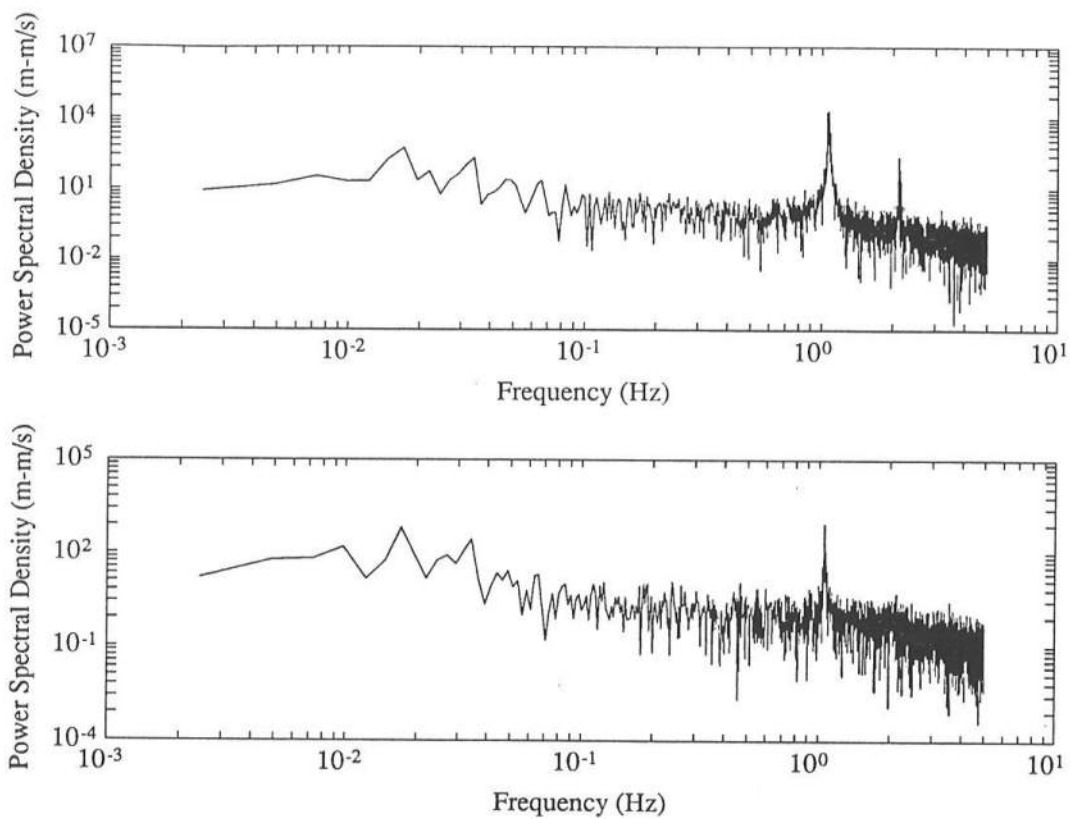
Figure 6.2: QTEST: frequency spectrum of the cross–shore velocity (top) and the longshore velocity time series (bottom) at location L9, current meter $WE\,62$.
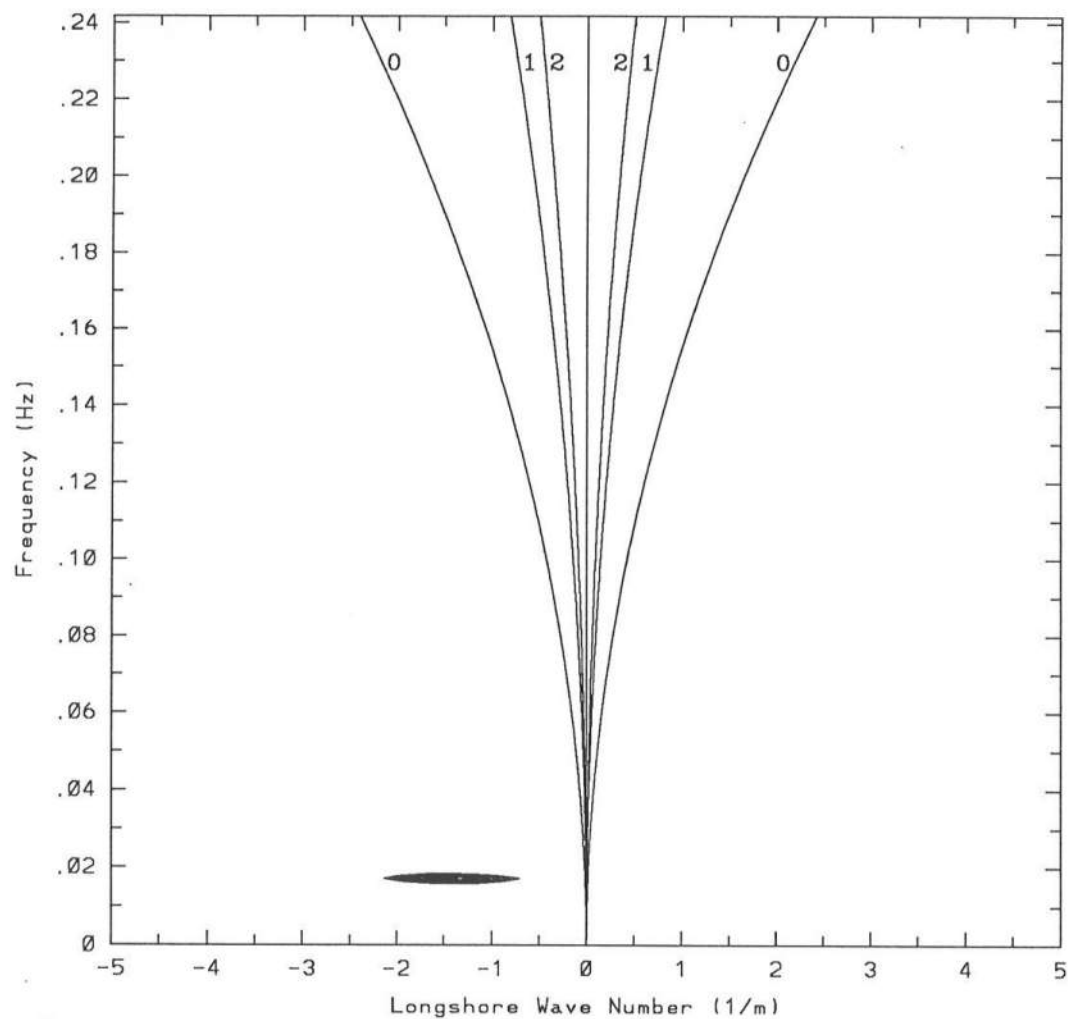
Figure 6.3: QTEST: wave number–frequency spectrum obtained from DFT analysis of cross–shore velocity data from 10 longshore locations. 1 Bartlett segment of 4096 points, $\Delta f = 2.44 \times 10^{-3}$ Hz, $\Delta k = 0.1$ m^{-1}, top 6 out of 10 contours plotted.

Table 6.1: Theoretical, observed and measured values of the rip current cell and incident
wave field parameters for QTEST.

QTEST depth = 0.17 m	Theoretical predictions or requested values	Observed values	Measured values
T_1	0.95 s	-	0.94 s
T_2	0.93 s	-	0.92 s
θ_1	$+10.00°$	-	$+11.41°$
θ_2	$-1.00°$	-	$0.00°$
k_1 (L_1)	5.89 m^{-1} (1.07 m)	-	5.96 m^{-1} (1.05 m)
k_2 (L_2)	6.01 m^{-1} (1.05 m)	-	6.11 m^{-1} (1.03 m)
$k_r = k_1/k_2$	0.98	-	0.98
predicted Cg_y/C_2	-0.10	-	-
$\Rightarrow Cg_y$	-11.60 cm/s	-	-
Lg_y	5.57 m	6.5–6.7 m	4.83 m
Tg	59.84 s	≈ 58 s	58.55 s
Cg_y	-9.31 cm/s	≈ -9 cm/s	-8.20 cm/s

frequency of the migrating rip currents, accurate to within the frequency resolution. The low frequency energy has longshore wave numbers spread over the range of 0.7–2.2 m^{-1}, or 9.0–2.9 m respectively. The central wave number is 1.3 m^{-1}, or 4.8 m, which is lower than the theoretically predicted values and laboratory observations of the rip cell length. Comparisons of theoretical, observed and measured values of the rip cell lengths and periods for the first set of experimental test cases are presented in table 6.1.

The differences between the observed, measured and theoretically predicted rip cell lengths, periods and longshore speed of migration for this test case are due to assumptions made in the theory and the nature of the analysis methods. As discussed in chapter 3, the equations used to predict suitable incident wave field conditions leading to the generation of migrating rip currents are based on linear theory. Shallow water conditions were made to simplify the equations and enable preliminary calculations of Cg_y, the longshore speed

of migration of the rip cells (equation 3.42). Once the incident wave train parameters have been selected, Cg_y can be recalculated without involving the shallow water assumption (equation 3.29). Table 6.1 lists the incident wave train parameters for QTEST, giving both the specified, or requested parameters and those actually generated in the wave tank and measured by the wave gauge array. The initial prediction of Cg_y is also presented along with the recalculated, visually observed, and experimentally measured values of Cg_y, Lg_y and Tg_y (rip cell period).

In the laboratory experiments, the actual waves are invariably non–linear, particularly in shallow water. Differences between the theoretical and measured rip cell parameters are therefore expected. The difference between the predicted and recalculated value of Cg_y give an indication of the inaccuracy of the shallow water assumption and an indirect indication of the validity of the linear wave theory. If the incident waves *were* linear there would be no difference between these two Cg_y values, the use of linear wave theory could be fully justified, and the observed/measured rip cell parameters would be expected to match the theoretical predictions.

Another source of discrepancy is the data analysis methods. The DFT analysis method tends to spread energy over several wave number bins. Unfortunately, peak splitting, due to large directional spread, prohibited the use of the more precise MLM analysis with the velocity data for this and most of the experimental test cases.

Despite the limitations mentioned above, the general result of the wave number–frequency spectrum analysis is clear: there is a strong concentration of low frequency energy in the nearshore region which has a frequency and longshore wave length corresponding to those of the rip current cells migrating along the beach. The low frequency energy is clearly not due to edge wave motions because it does not lie on, or even near any of the edge wave dispersion relationship curves. This low frequency motion has a wave length much shorter than any edge wave at the same frequency, and in this respect it is very similar to the low frequency motions seen by Tang and Dalrymple (1989) and Oltman–Shay, Howd and Birkemeier (1989). However, the low frequency motions observed by Oltman–Shay *et al.* were spread over a range of frequencies and linearly dependent wave

numbers, producing not just one concentration of energy in the wave number–frequency spectrum, but a whole line of energy (see figure 2.4).

The wave data from the three–point linear array were analysed using the MLM technique. This method was more successful with the wave data than with the current data, possibly because the analysis concentrated on the incident waves which had angles of incidence closer to the beach normal. However, the energy peaks in the spectra were much broader than expected. The wave number–frequency spectrum based on the wave data for the QTEST experimental case is presented in figure 6.4. The curved lines on the graph represent the linear dispersion relationship for various angles of incidence and for $h = 0.169$ m, the water depth at the location of the instrument arrays, where the wave heights were measured. These lines indicate limits for the occurrence of surface gravity waves at given frequencies and angles of incidence.

All the wave number–frequency spectra based on wave data were generated by dividing the full records of 4096 data points into four segments of 1024 points, which were then Bartlett averaged. This averaging process was more successful with the wave gauge data than with the current data probably because the incident wave signals were stronger and better defined than the low frequency signals.

For this experimental test case, the energy contours in the wave number–frequency spectrum highlight the two incident wave trains that were generated in the wave basin. The two concentrations are at frequencies which correspond to the theoretically generated frequencies, within the resolution of the spectrum. They are of different intensities, suggesting that one of the two incident wave trains had less energy than the other. This implies that the wave trains had different heights and is probably due to the wave heights being specified on the basis of paddle stroke lengths. As previously mentioned, wave trains with equal stroke lengths but different frequencies will have different heights. The effect of this height difference is magnified in the wave number–frequency spectrum, which is based on a measure of energy, because energy is proportional to the square of the wave height.

By determining the peak longshore wave number of the energy concentrations in
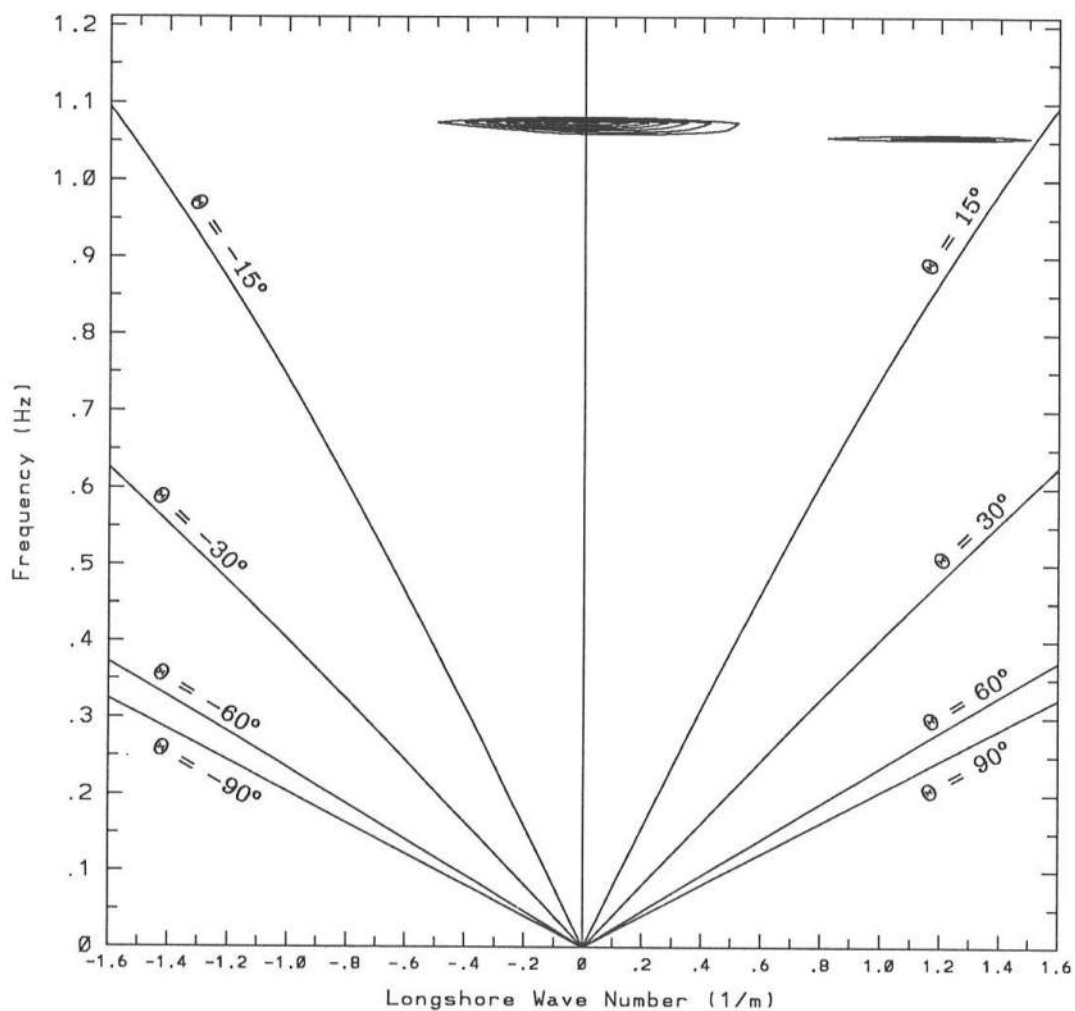
Figure 6.4: QTEST: wave number–frequency spectrum obtained from MLM analysis of wave data from 3 longshore locations. 4 Bartlett segments of 1024 points, $\Delta f = 9.77 \text{x} 10^{-3}$ Hz, $\Delta k = 0.025$ m^{-1}, top 7 out of 10 contours plotted.

the wave number–frequency spectrum, the angle of incidence of the two wave trains can be found from

$$\text{longshore wave number} = |\mathbf{k}| \sin \theta$$

where the wave number vector, $\mathbf{k}$ is known from the measured wave period via the linear dispersion relationship. To assist the determination of the peak longshore wave numbers, the energy spread over all the longshore wave numbers at the two incident wave frequencies was plotted, see figure 6.5. For this test case the measured angles were found to be $+11.4^o$ and 0°. The theoretically required angles of incidence were $+10^o$ and -1°. Table 6.1 provides a summary of the requested and generated incident wave train parameters. Comparing these values gives an indication of the ability of the wavemaker to accurately generate specific wave trains. Values of the rip cell length, period and longshore speed of migration calculated from the measured incident wave train parameters are also given in table 6.1.

6.3 Experimental Test Case: RTEST

The height of the incident waves for this case were identical to those in QTEST, so the observed breaking characteristics were very similar. However, the alternating nature of the waves breaking either side of a rip current was more pronounced. This was probably due to the increased frequency difference between the two incident wave trains. This increased frequency difference was also responsible for the increased speed of migration of the rip currents along the beach. The rip cell length was smaller for this case, estimated at 5.8 m, so a maximum of three rip cells could be seen on the beach at any given time. The rip currents were, again, migrating to the northern end of the beach and were observed to be stronger than those in QTEST. The period of the rip cells was estimated to be 37 s.

The water surface elevation and cross–shore and longshore velocity time series from location L9 are presented in figure 6.6. Each time series displays a low frequency modulation which is reflected in the frequency spectra of each velocity record in the form of significant energy at $f \approx 0.03$ Hz, see figure 6.7. The two velocity time series and the water surface elevation record show phase differences similar to those in QTEST.
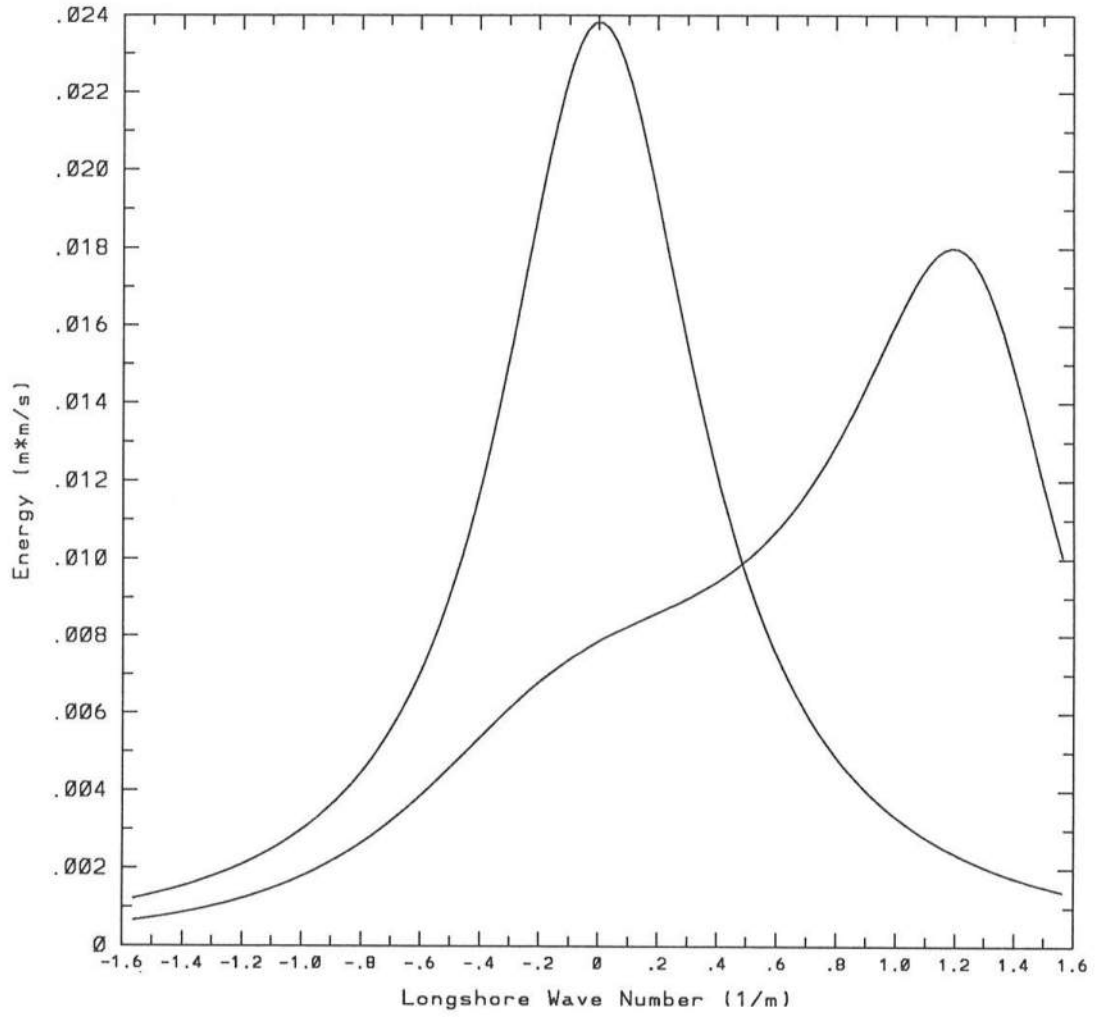
Figure 6.5: QTEST: energy spread over all the longshore wave numbers for the two incident wave frequencies. MLM analysis of wave data from 10 longshore locations. 4 Bartlett segments of 1024 points, $\Delta k = 0.025$ m^{-1}.
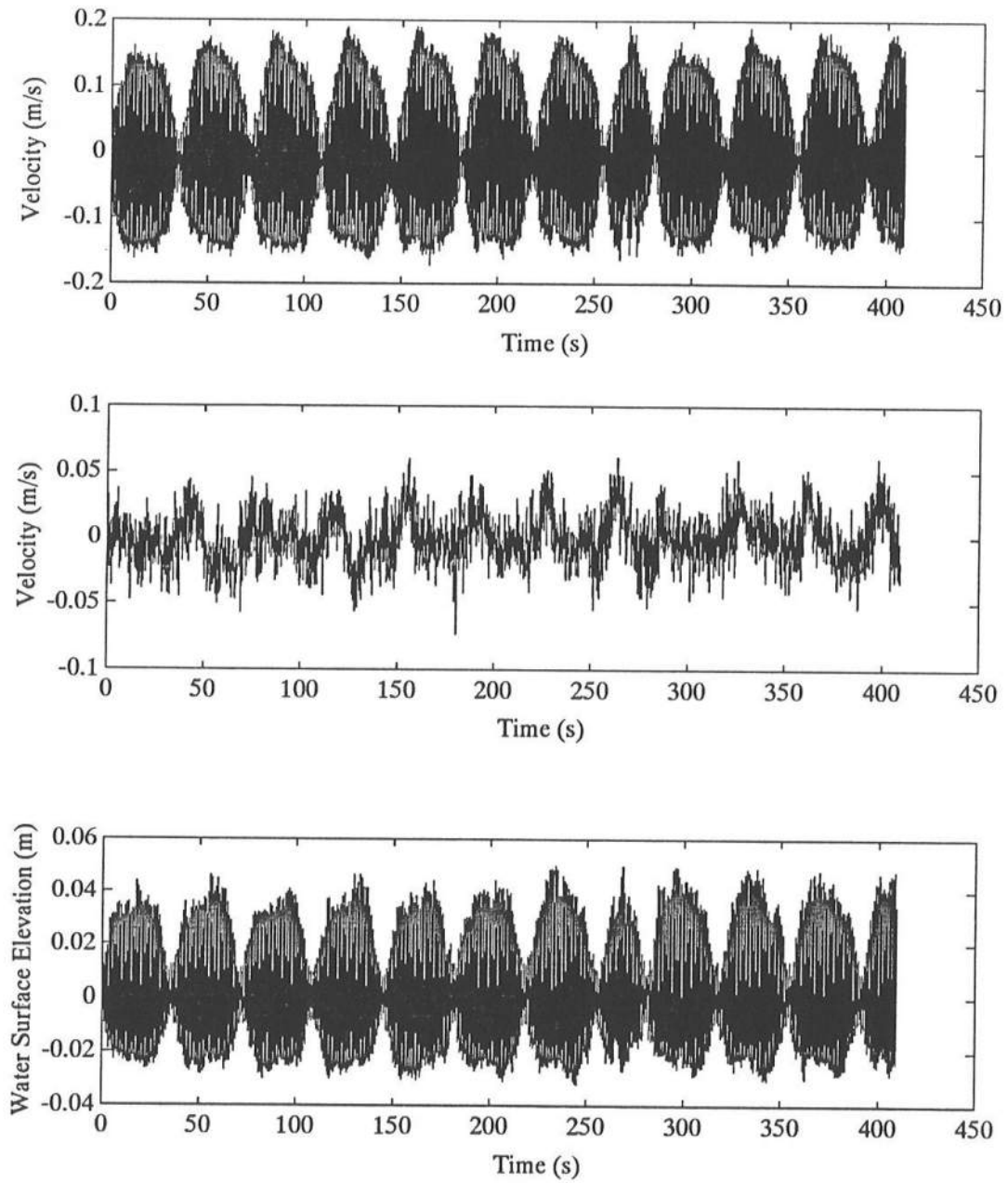
Figure 6.6: RTEST: time series of the cross–shore velocity (top), the longshore velocity (middle), and the water surface elevation (bottom) at location L9, current meter $WE\,62$.
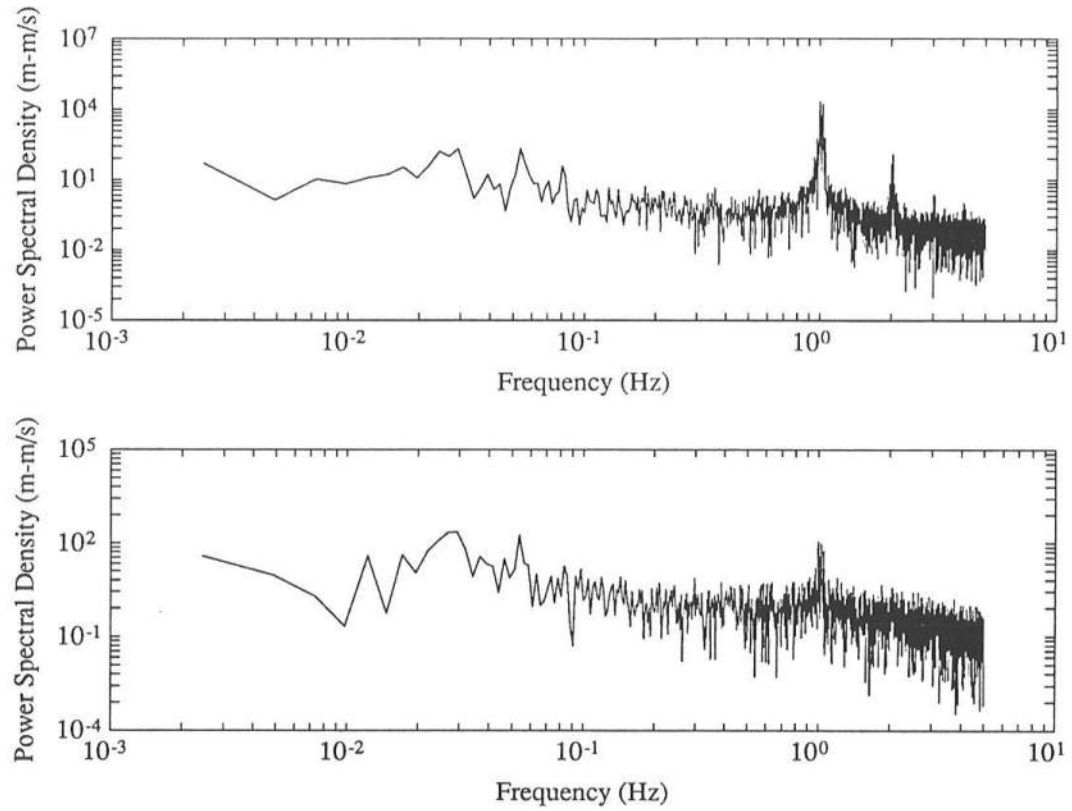
Figure 6.7: RTEST: frequency spectrum of the cross–shore velocity (top) and the long-shore velocity time series (bottom) at location L9, current meter $WE\,62$.

For this experimental test case, cross–shore velocity records from three of the ten array locations were considered unreliable because they displayed excessive electrical noise, or had unexpectedly low energy at the low end of the frequency spectrum. The wave number–frequency spectrum was therefore computed using data from the remaining seven locations, see figure 6.8. Two Bartlett segments of 2048 data points were averaged and passed through the DFT analysis. As for the previous test case, there is a concentration of energy at a low frequency and yet with shorter wave lengths than expected if the motion was due to edge waves. The frequency of the energy is 0.0293 Hz $(6\Delta f)$, and the central wave number corresponds to a wave length of 4.8 m. The observed, measured and predicted rip cell periods correspond very well, within the resolution of the analysis. However, as for the previous test case, the measured rip cell length is shorter than the predicted value. Comparisons between the theoretically predicted rip cell length and period, and the observed and measured values are presented in table 6.2.

Unlike the QTEST results, a second pocket of energy is seen in the wave number–frequency spectrum at twice the frequency and wave number as the first one. This is a harmonic of the primary low frequency motion, a manifestation of the DFT analysis process. The DFT method regards the changing cross–shore velocity as a longshore progressive wave. The maximum offshore velocity in the rip currents corresponds to the crest of the wave, and the maximum onshore velocity corresponds to the trough of the wave where the flow recirculates back towards the shore in the center of the rip cell. It is easily concluded, that the longshore progressive wave is not purely sinusoidal, as the offshore flow in the narrow rip currents is far faster than the return flow between them (see figure 1.1). Rather, the longshore progressive wave resembles a non–linear wave form, with higher, steeper crests, and longer, shallower troughs. When this wave form is analysed and decomposed into its component sine waves, it produces a fundamental frequency and harmonics of that frequency. In wave number–frequency space, the second harmonic has twice the frequency and wave number of the fundamental, as seen in figure 6.8. This phenomenon was not observed in the QTEST results probably because the rip currents were not as strong and the flows had already begun to dissipate by the time they reached
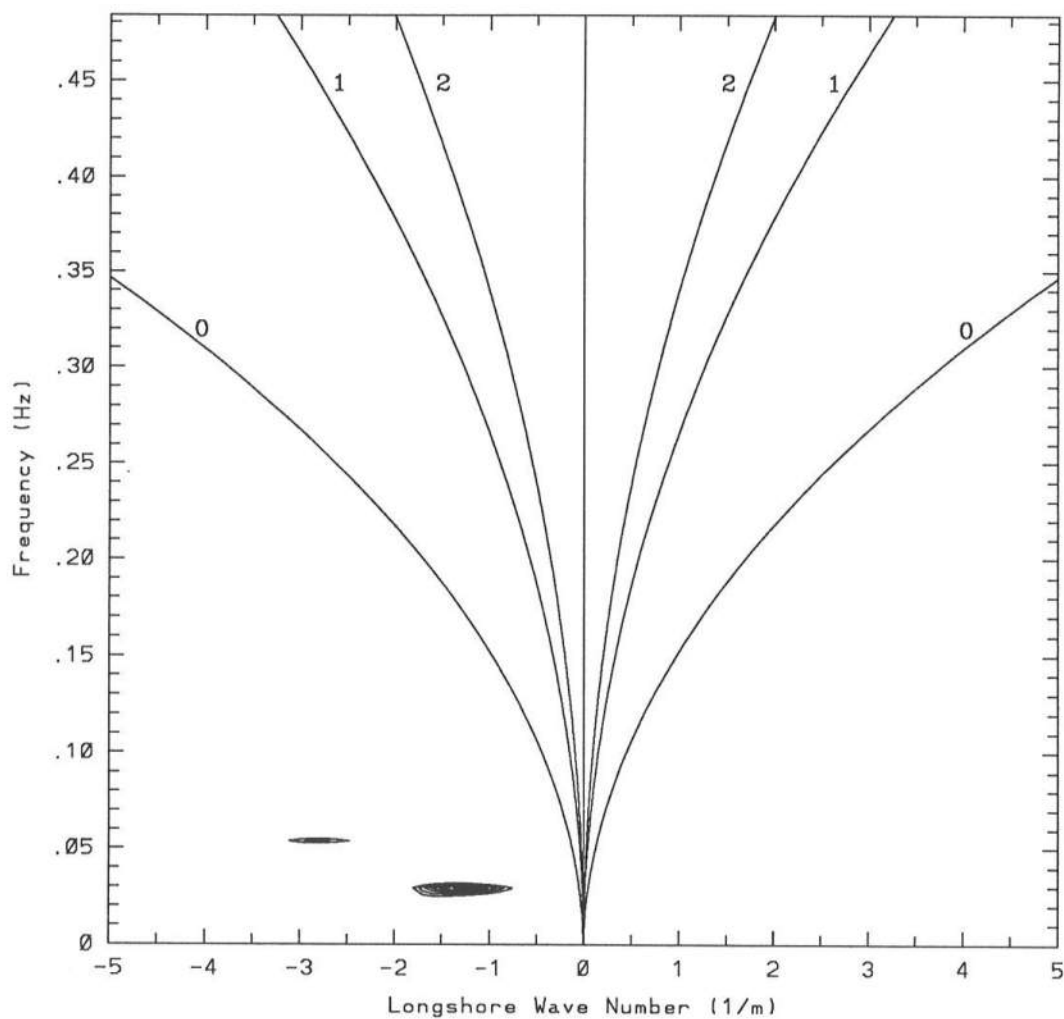
Figure 6.8: RTEST: wave number–frequency spectrum obtained from DFT analysis of cross–shore velocity data from 7 longshore locations (L2, L4, L5, L7, L8, L9 and L10). 2 Bartlett segments of 2048 points, $\Delta f = 4.88\text{x}10^{-3}$ Hz, $\Delta k = 0.1$ m^{-1}, top 6 out of 10 contours plotted.

Table 6.2: Theoretical, observed and measured values of the rip current and incident wave field parameters for RTEST.

RTEST depth = 0.17 m	Theoretical predictions or requested values	Observed values	Measured values
T_1	1.00 s	-	0.99 s
T_2	0.97 s	-	0.97 s
θ_1	$+3.00°$	-	$+2.89°$
θ_2	$-10.00°$	-	$-5.18°$
$k_1 \ (L_1)$	5.51 m^{-1} (1.14 m)	-	5.55 m^{-1} (1.13 m)
$k_2 \ (L_2)$	5.70 m^{-1} (1.10 m)	-	5.75 m^{-1} (1.09 m)
$k_r = k_1/k_2$	0.97	-	0.97
predicted Cg_y/C_2	-0.15	-	-
$\Rightarrow Cg_y$	-16.8 cm/s	-	-
Lg_y	4.92 m	4.9–5.5 m	4.83 m
Tg	36.59 s	≈ 38 s	34.13 s
Cg_y	-13.50 cm/s	≈ -13.5 cm/s	-14.15 cm/s

the current meters. The longshore progressive wave would therefore have had a more sinusoidal shape.

For this experimental test case, the wave number–frequency spectrum was also computed from the longshore velocity data, presented in figure 6.9. There is only one pocket of energy in the spectrum with a frequency and longshore wave number very similar to that of the fundamental feature in figure 6.8. The lack of a second harmonic is probably a result of the smaller magnitude of the longshore currents. In general, wave number–frequency spectra computed from longshore velocity data provided less information about the energetic motions in the nearshore region, so the data analysis concentrated on the cross–shore velocity data.

The MLM analysis of the wave data for this test case is presented in figure 6.10. The two incident wave trains are clearly represented at their theoretically predicted frequencies. However, the angles of incidence calculated from the peak longshore wave numbers are $+2.9^o$ and -5.2^o. The requested angles were $+3^o$ and -10°. These results suggest that the wavemaker has difficulties producing waves at some angles of incidence. Table 6.2 provides a summary of theoretical and measured incident wave train parameters and the values of the rip current spacing and longshore speed of propagation that would be predicted from the measured angles of incidence.

6.4 Experimental Test Case: PTEST

As previously explained in chapter 5, PTEST is identical to RTEST except in wave height. The incident waves for this case broke approximately 0.8–0.9 m offshore, in water depths of 8–9 cm. Due to the increased wave heights, and therefore energy, in the nearshore region, the rip currents were much stronger, travelling 2–2.5 m offshore before slowing and dissipating. Paradoxically, the rip cell length, estimated from visual observations as approximately 6.1 m, was larger than for RTEST; it should have been identical. However, the estimated rip cell period, 37 s, was the same as for RTEST implying that these rip currents were migrating faster along the beach.

The water surface elevation and cross–shore and longshore velocity time series from
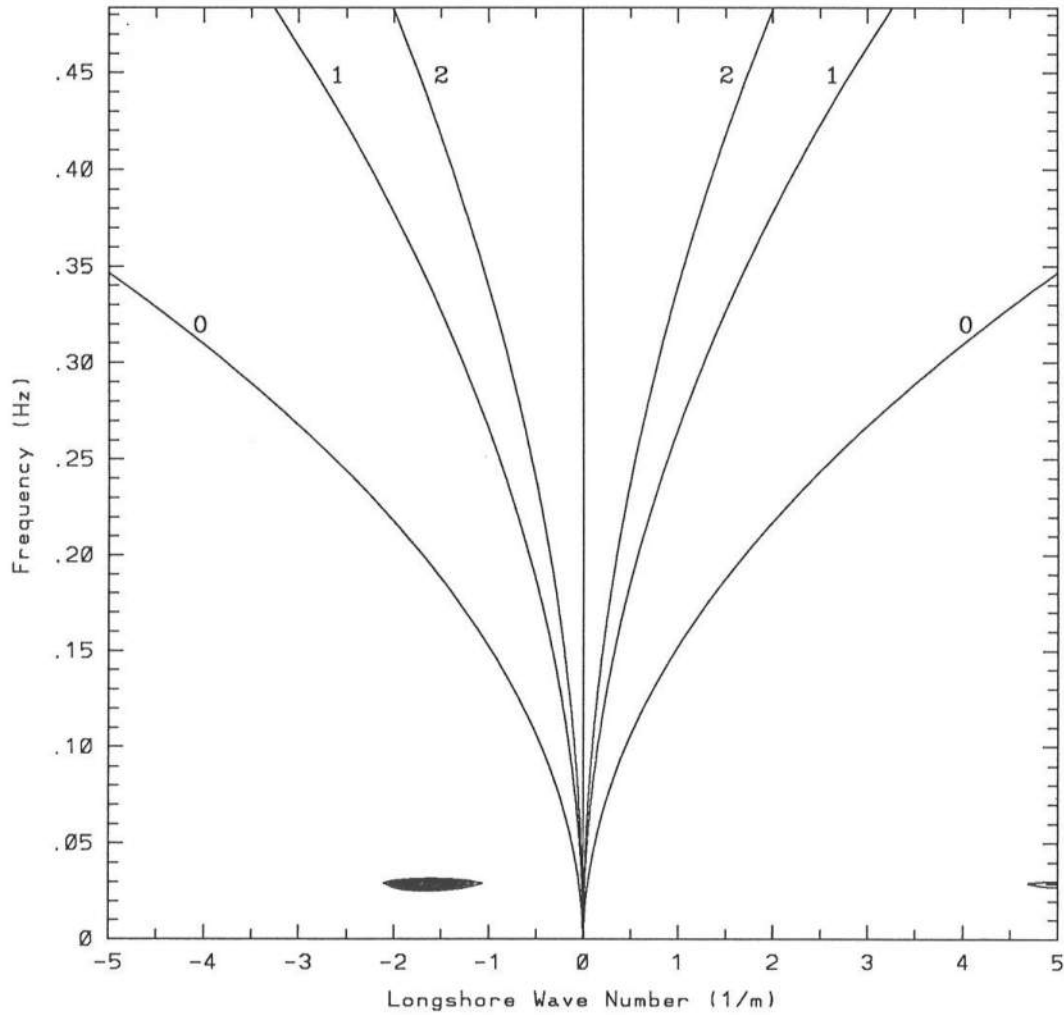
Figure 6.9: RTEST: wave number–frequency spectrum obtained from DFT analysis of longshore velocity data from 7 longshore locations (L2, L4, L5, L7, N8, L9 and L10). 2 Bartlett segments of 2048 points, $\Delta f = 4.88\text{x}10^{-3}$ Hz, $\Delta k = 0.1$ m^{-1}, top 6 out of 10 contours plotted.
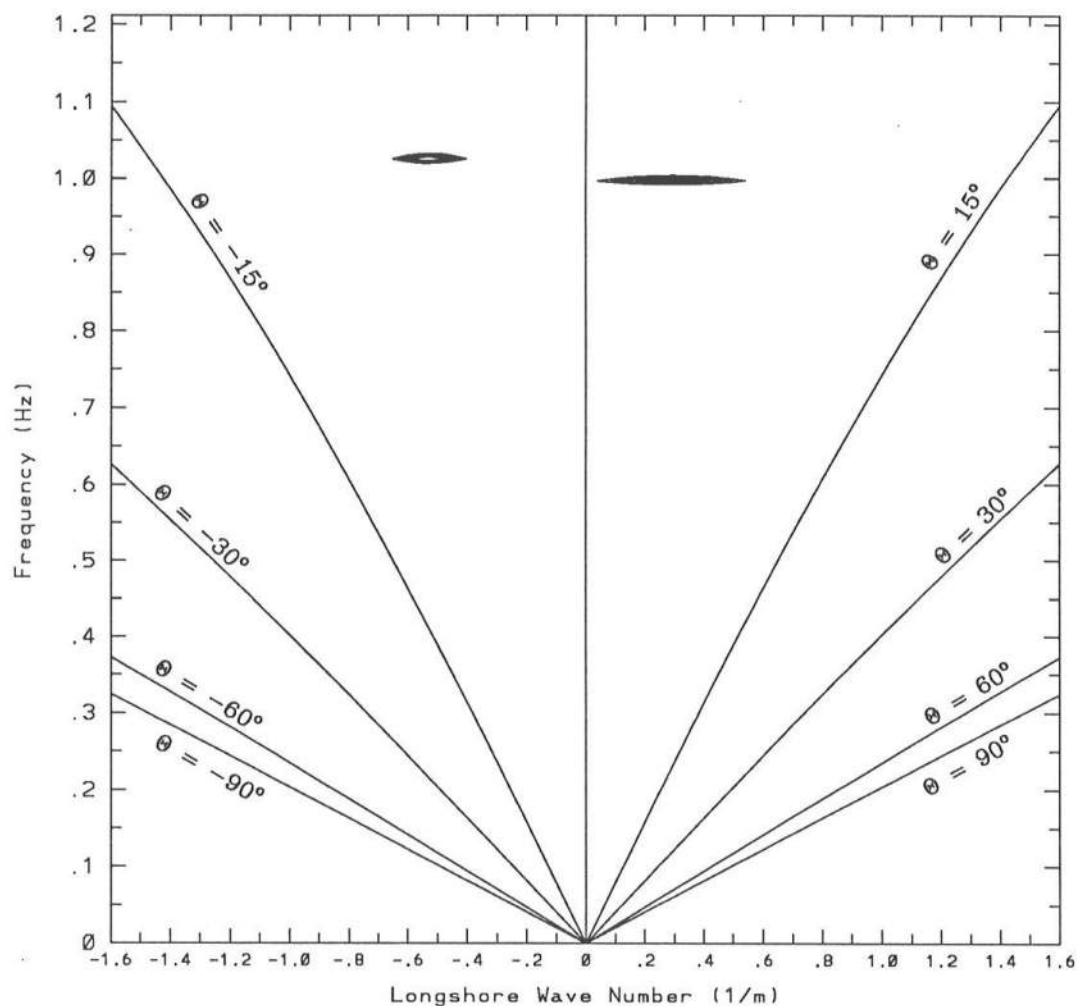
Figure 6.10: RTEST: wave number–frequency spectrum obtained from MLM analysis of wave data from 3 longshore locations. 4 Bartlett segments of 1024 points, $\Delta f = 9.77 \text{x} 10^{-3}$ Hz, $\Delta k = 0.025$ m^{-1}, top 6 out of 10 contours plotted.

location L9 are presented in figure 6.11. The longshore velocities for this experimental test case are noticeably stronger, and the low frequency modulation is more pronounced than for RTEST, due to the increased wave heights. As for the previous two cases, the phase differences between the time series at the group frequency are very similar to those predicted by the theory. As was seen for the previous test cases, the low frequency modulation in the velocity records is translated into a peak of energy at a low frequency in their spectra, figure 6.12. The wave number–frequency spectrum, derived from cross-shore velocity data from all ten locations in the current meter array, is presented in figure 6.13. It is very similar to that of RTEST, and was likewise computed using two Bartlett segments of 2048 points. There are two concentrations of energy, a fundamental feature, which has a frequency of 0.0293 Hz and a central wave number of 1.0–1.1 m^{-1} (6.28–5.7 m respectively), and a strong second harmonic which has approximately twice the frequency and wave number. Comparisons between the theoretically predicted rip cell length and period, and the observed and recorded values are presented in table 6.3.

The wave number–frequency spectrum based on the MLM analysis of the wave data for this test case is presented in figure 6.14. The two incident wave trains are identified at their theoretical frequencies, but again, the incident angles, as calculated from the peak wave numbers, are different from the requested angles. The measured angles are -4.8^{o} and $+2.1^{o}$, whereas the requested angles of incidence were -10° and $+3^{o}$.

6.5 Experimental Test Case: STEST

As noted in chapter 5, this test case is unique because the rip currents migrate in a direction opposite to that of the incoming waves. This phenomenon was confirmed by visual observations made during the experimental runs for this case. The rip currents were not well defined, but it was clear that the wave groups and the nodal lines propagated towards the southern end of the beach. The incident waves were breaking about 0.6–0.7 m offshore in water depths of 6–7 cm. The rip cell length was estimated at 4.3 m, and a maximum of four rip currents were visible on the beach at any given time.

The water surface elevation and cross–shore and longshore velocity time series from
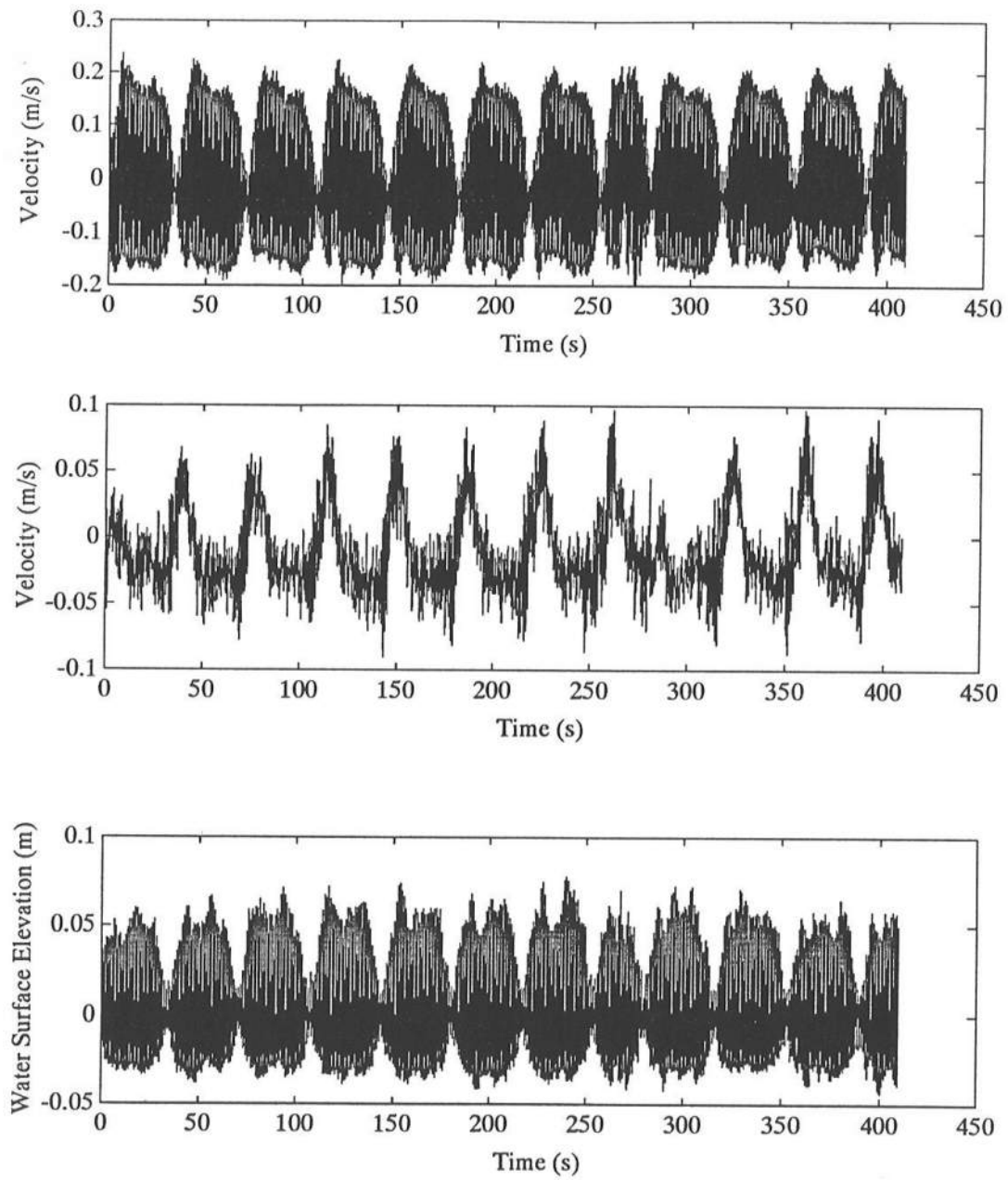
Figure 6.11: PTEST: time series of the cross–shore velocity (top), the longshore velocity (middle), and the water surface elevation (bottom) at location L9, current meter $WE\,62$.
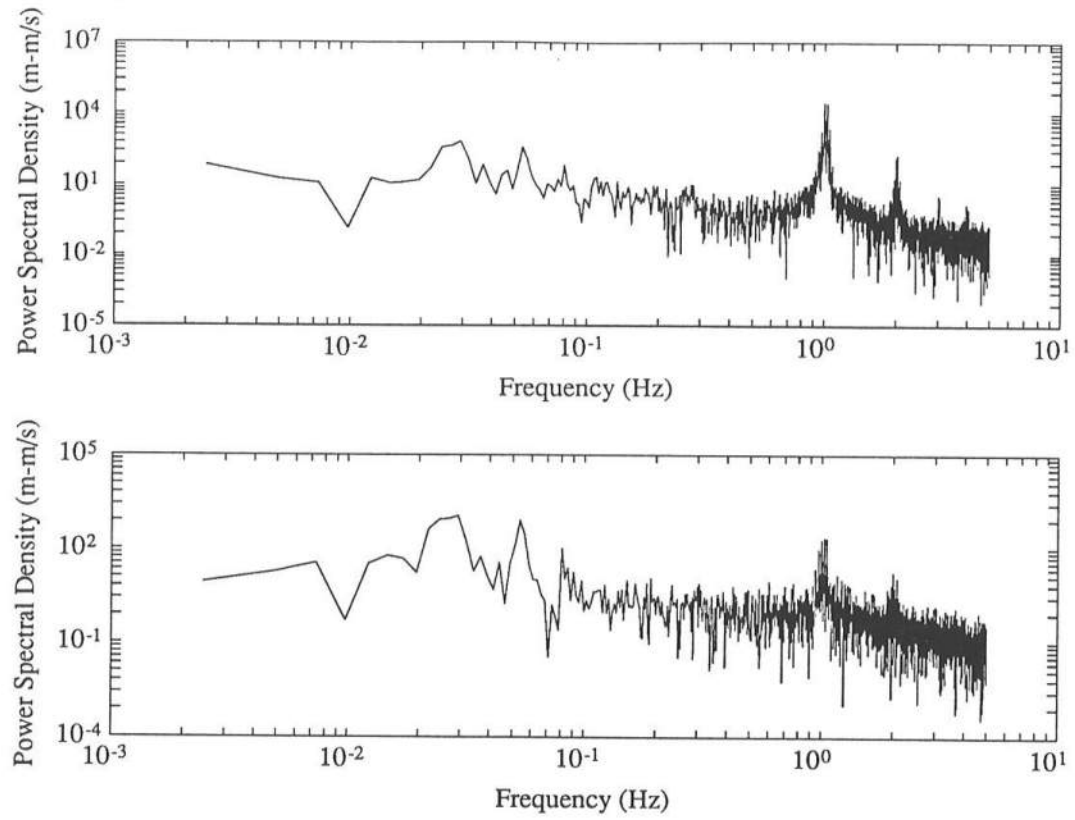
Figure 6.12: PTEST: frequency spectrum of the cross–shore velocity (top) and the long-shore velocity time series (bottom) at location L9, current meter $WE\,62$.
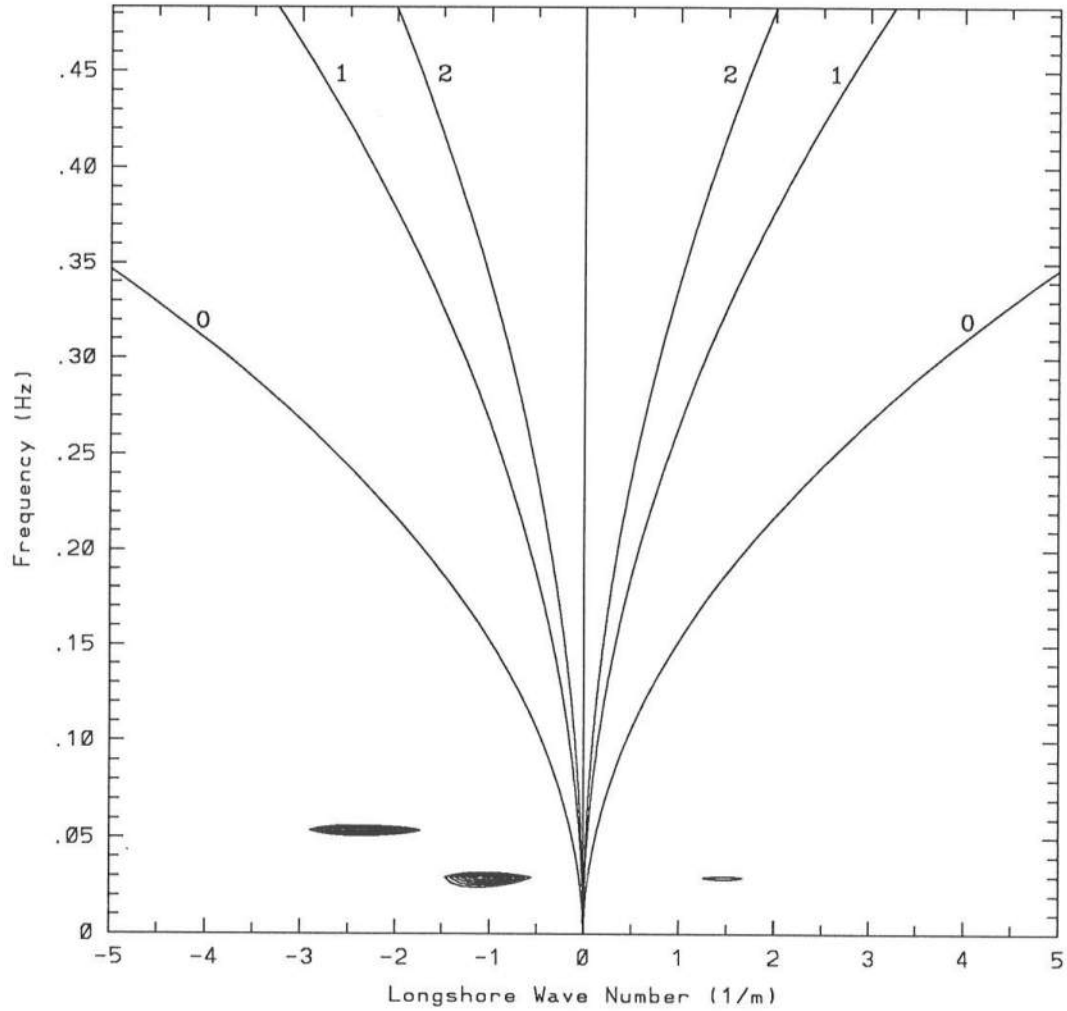
Figure 6.13: PTEST: wave number–frequency spectrum obtained from DFT analysis of cross–shore velocity data from 10 longshore locations. 2 Bartlett segment of 2048 points, $\Delta f = 4.88 \times 10^{-3}$ Hz, $\Delta k = 0.1$ m^{-1}, top 6 out of 10 contours plotted.

Table 6.3: Theoretical, observed and measured values of the rip current and incident wave field parameters for PTEST.

PTEST depth $= 0.17$ m	Theoretical predictions or requested values	Observed values	Measured values
T_1	1.00 s	-	0.99 s
T_2	0.97 s	-	0.97 s
θ_1	$+3.00°$	-	$+2.05°$
θ_2	$-10.00°$	-	$-4.79°$
$k_1\ (L_1)$	5.51 m^{-1} (1.14 m)	-	5.55 m^{-1} (1.13 m)
$k_2\ (L_2)$	5.70 m^{-1} (1.10 m)	-	5.75 m^{-1} (1.09 m)
$k_r = k_1/k_2$	0.97	-	0.97
predicted Cg_y/C_2	-0.15	-	-
$\Rightarrow Cg_y$	-16.8 cm/s	-	-
Lg_y	4.92 m	5.8–6.1 m	5.70–6.28 m
Tg	36.59 s	≈ 44 s	34.13 s
Cg_y	-13.50 cm/s	≈ -13.5 cm/s	-17.50 cm/s

Figure 6.14: PTEST: wave number–frequency spectrum obtained from MLM analysis of wave data from 3 longshore locations. 4 Bartlett segments of 1024 points, $\Delta f = 9.77\text{x}10^{-3}$ Hz, $\Delta k = 0.025$ m^{-1}, top 6 out of 10 contours plotted.

location L9 are presented in figure 6.15. The groupiness of the cross–shore velocity record is not as clean as for the previously presented test cases. The cross–shore velocity does not drop to zero at the "nodes" of the groups. The longshore velocity record displays limited low frequency periodicity, but in a different way from the previous test cases. The longshore velocity time series displays groups similar to, and in phase with, the groups in the cross–shore velocity record. These phase differences are predicted by the theory for incident waves propagating from the same side of the beach normal. The groups in the water surface elevation time series are in phase with those in the cross–shore velocity record, as for all the previous test cases. The frequency spectra of both velocity time series are presented in figure 6.16. The longshore velocity spectrum does not exhibit a significant peak of energy at the rip current frequency, although one is present in the cross–shore velocity spectrum. As for all the test cases, the energy at the incident wave frequencies is easily identified and dominates the high frequency end of the spectrum.

This test case was the only one of all the experimental cases for which MLM analysis of the cross–shore velocity data was successful. As a result, the resolution of energy in the wave number–frequency spectrum, presented in figure 6.17, is higher. Unlike the previous cases, the pocket of low frequency energy is in the positive wave number range because the rip currents were migrating in the opposite direction. The wave number–frequency spectrum was computed using 2 Bartlett segments of 2048 data points, with $\Delta f = 0.00488$ Hz. The frequency of the concentration of energy is 0.0244 Hz ($5\Delta f$), and the wave number is 1.7 m^{-1} (3.7 m). These both correspond very well with the theoretically predicted values, and, as before, the measured longshore wave length is lower than the observed value of the rip cell length. Comparisons between the theoretically predicted rip cell length and period, and the observed and recorded values are presented in table 6.4.

Figure 6.18 shows the wave number–frequency spectrum computed using the wave data collected during this experimental test case. The incident wave trains are represented at their theoretical frequencies, and again, the measured angles of incidence, -7.7^o and -20.1^o, differ from the requested values, -10° and -30°. Unlike the previous spectra

Figure 6.16: STEST: frequency spectrum of the cross–shore velocity (top) and the long-shore velocity time series (bottom) at location L9, current meter $WE\,62$.

Figure 6.15: STEST: time series of the cross–shore velocity (top), the longshore velocity (middle), and the water surface elevation (bottom) at location L9, current meter $WE\,62$.
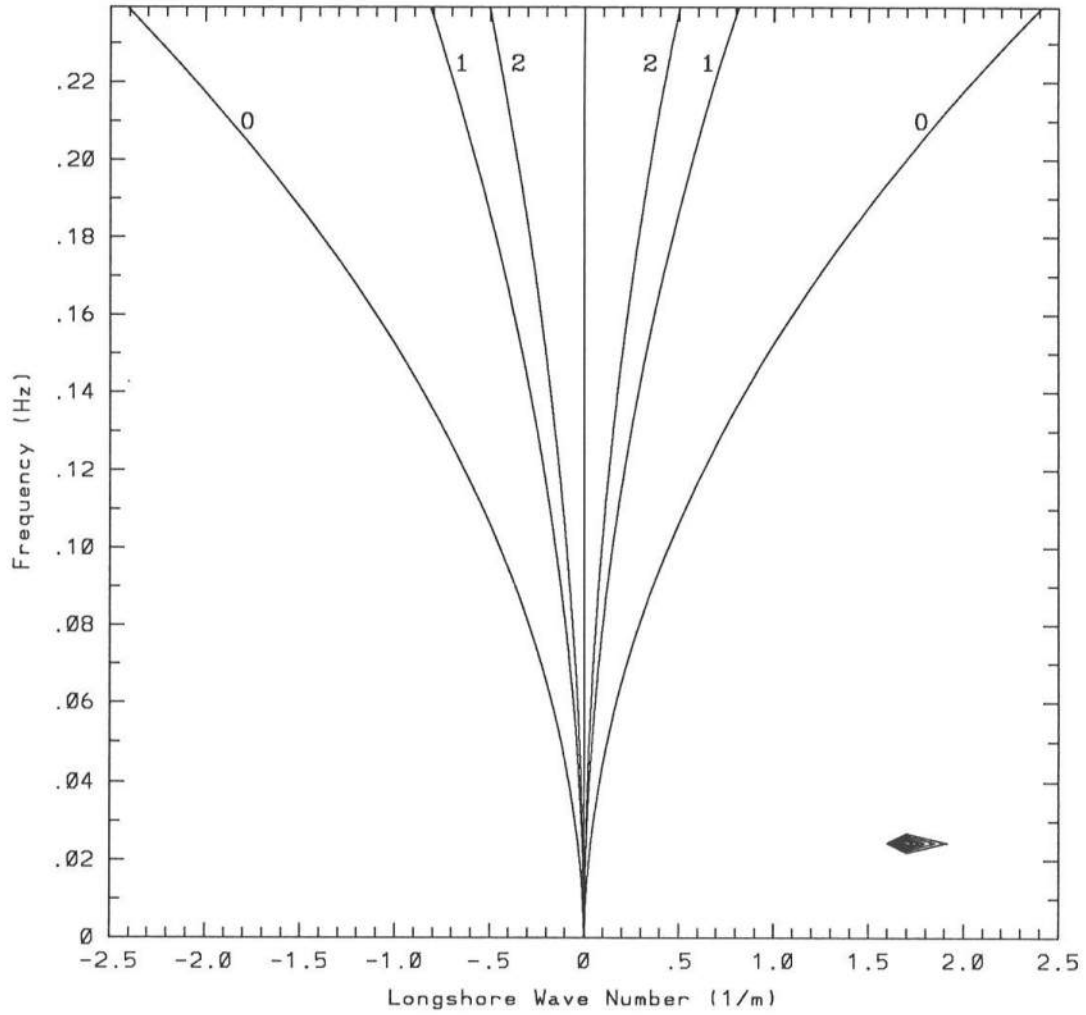
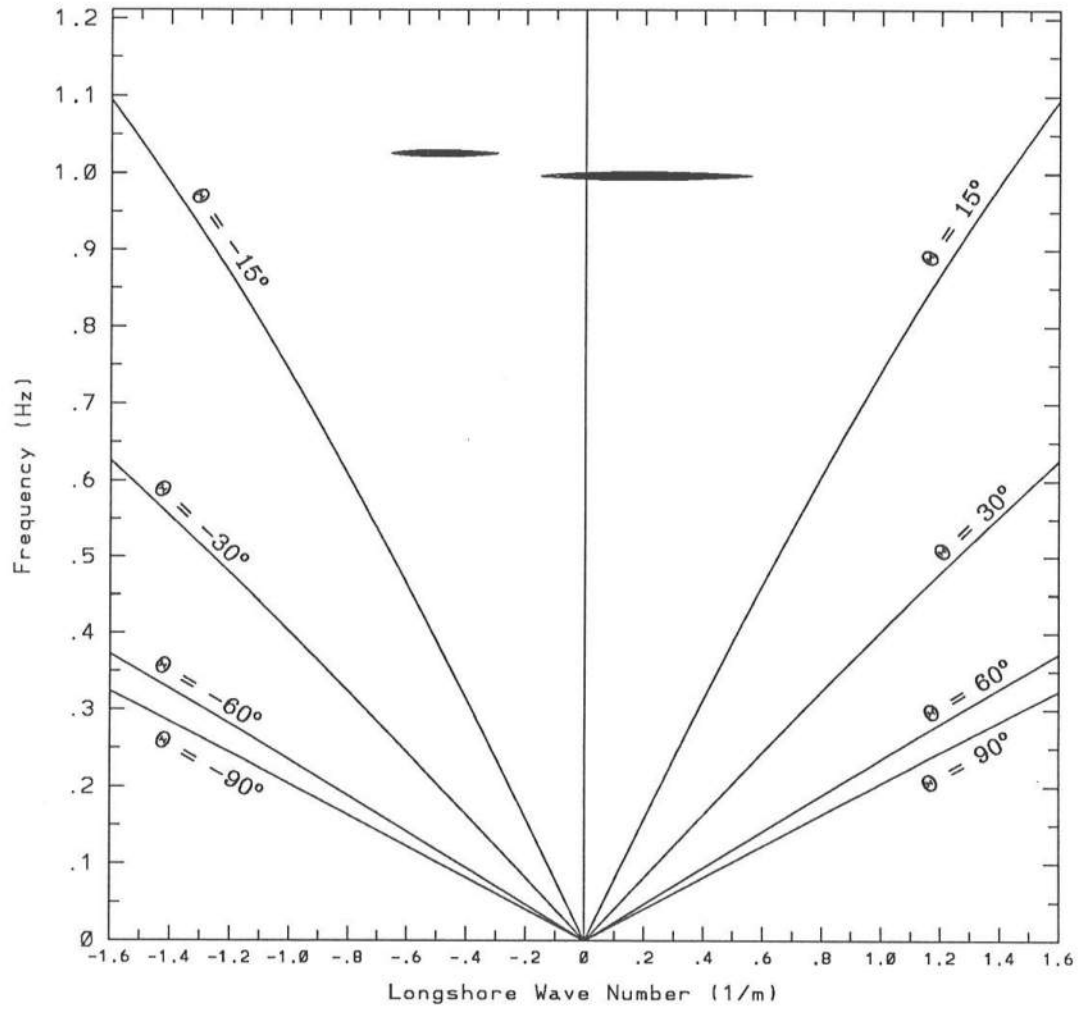**Figure 6.17:** STEST: wave number–frequency spectrum obtained from MLM analysis of cross–shore velocity data from 10 longshore locations. 2 Bartlett segment of 2048 points, $\Delta f = 4.88\text{x}10^{-3}$ Hz, $\Delta k = 0.1$ m^{-1}, top 6 out of 10 contours plotted.

Table 6.4: Theoretical, observed and measured values of the rip current and incident wave field parameters for STEST.

STEST depth = 0.17 m	Theoretical predictions or requested values	Observed values	Measured values
T_1	0.97 s	-	0.96 s
T_2	0.95 s	-	0.94 s
θ_1	-30.00^o	-	-20.1^o
θ_2	-10.00^o	-	-7.70^o
$k_1\ (L_1)$	5.72 m^{-1} (1.10 m)	-	5.82 m^{-1} (1.08 m)
$k_2\ (L_2)$	5.89 m^{-1} (1.07 m)	-	5.96 m^{-1} (1.05 m)
$k_r = k_1/k_2$	0.97	-	0.98
predicted Cg_y/C_2	0.08	-	-
$\Rightarrow Cg_y$	8.54 cm/s	-	-
Lg_y	3.78 m	4.3 m	3.70 m
Tg	42.25 s	$\approx$ 56 s	40.98 s
Cg_y	8.95 cm/s	$\approx$ 7.6 cm/s	9.03 cm/s

derived from wave data, 27 contours were plotted before energy representing the second wave train appeared on the graph. This suggests that one of the wave trains had much less energy than the other, a conclusion that was confirmed by looking at the 1–D frequency spectrum averaged over all three wave gauge locations, presented in figure 6.19. The weaker of the two wave trains was the one with the larger angle of incidence.The inequality between the two wave trains is probably due to the two wave trains being specified with equal paddle stroke lengths. Wave trains with equal paddle stroke lengths but different angles of incidence will have different wave heights.

6.6 Experimental Test Case: P2TEST

Theoretically, the incident wave conditions for this experimental case were identical to those for PTEST, but as the current meter array was located much closer to the breaker line, at 0.975 m offshore, the instruments measured velocities deeper in the throat of the rip currents as they passed, where the currents flow faster before slowing in the rip head. These higher velocities are seen in the cross–shore velocity time series, presented in figure 6.20 along with the longshore velocity and water surface elevation time series. Like the PTEST cross–shore velocity time series (figure 6.11, page 77), the groups in the incident wave field are easily identified, but in addition, high offshore velocities have been recorded between each group, i.e., when the rip currents pass the current meter. Typical maximum offshore velocities in the rip currents are 0.4–0.5 m/s. The low frequency modulation in the longshore velocity time series is very clear. The phase differences between the three time series agree very well, qualitatively, with the theoretical predictions.

The frequency spectra of the cross–shore and longshore velocity records, presented in figure 6.21, clearly show the incident wave energy and its harmonics. As expected, there is also a significant peak of energy at $f \approx 0.03$ Hz, which corresponds well to the predicted rip cell period of 36.6 s. In addition, several harmonics of this low frequency energy can be seen. Comparisons of theoretical, observed and measured values of the rip cell lengths and periods for this test case are presented in table 6.5.

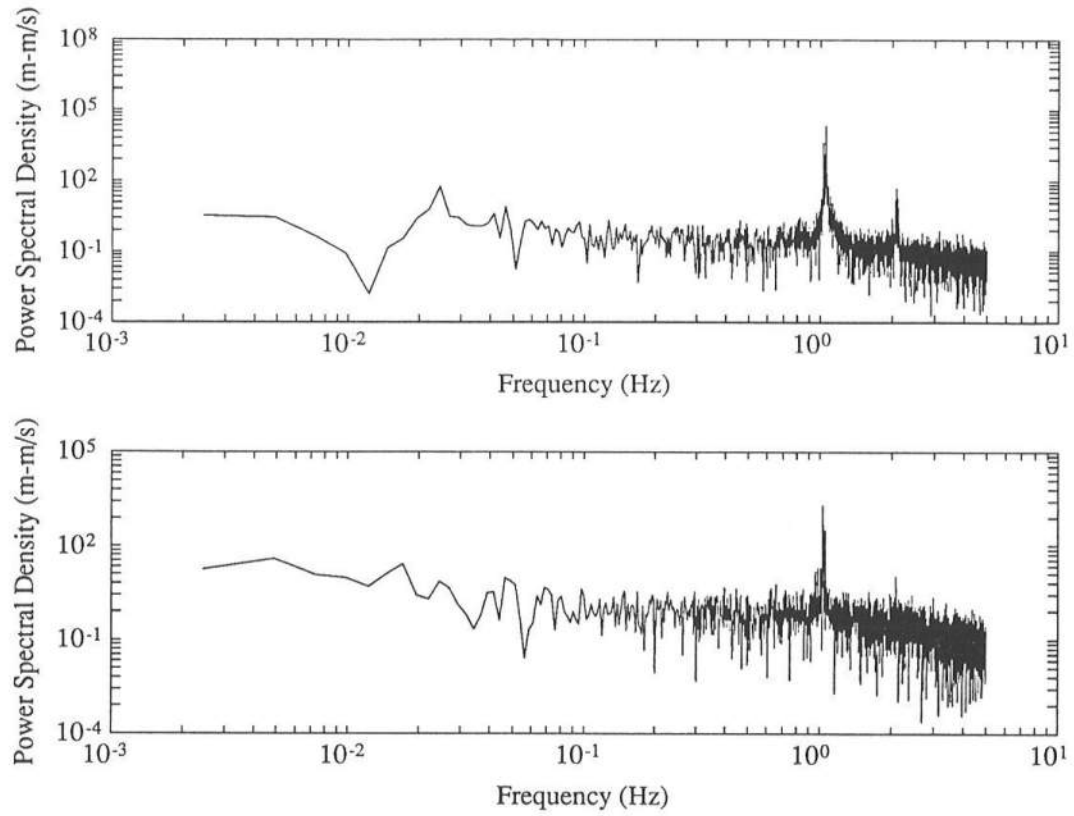Cross–shore velocity data from all ten current meter array locations were combined
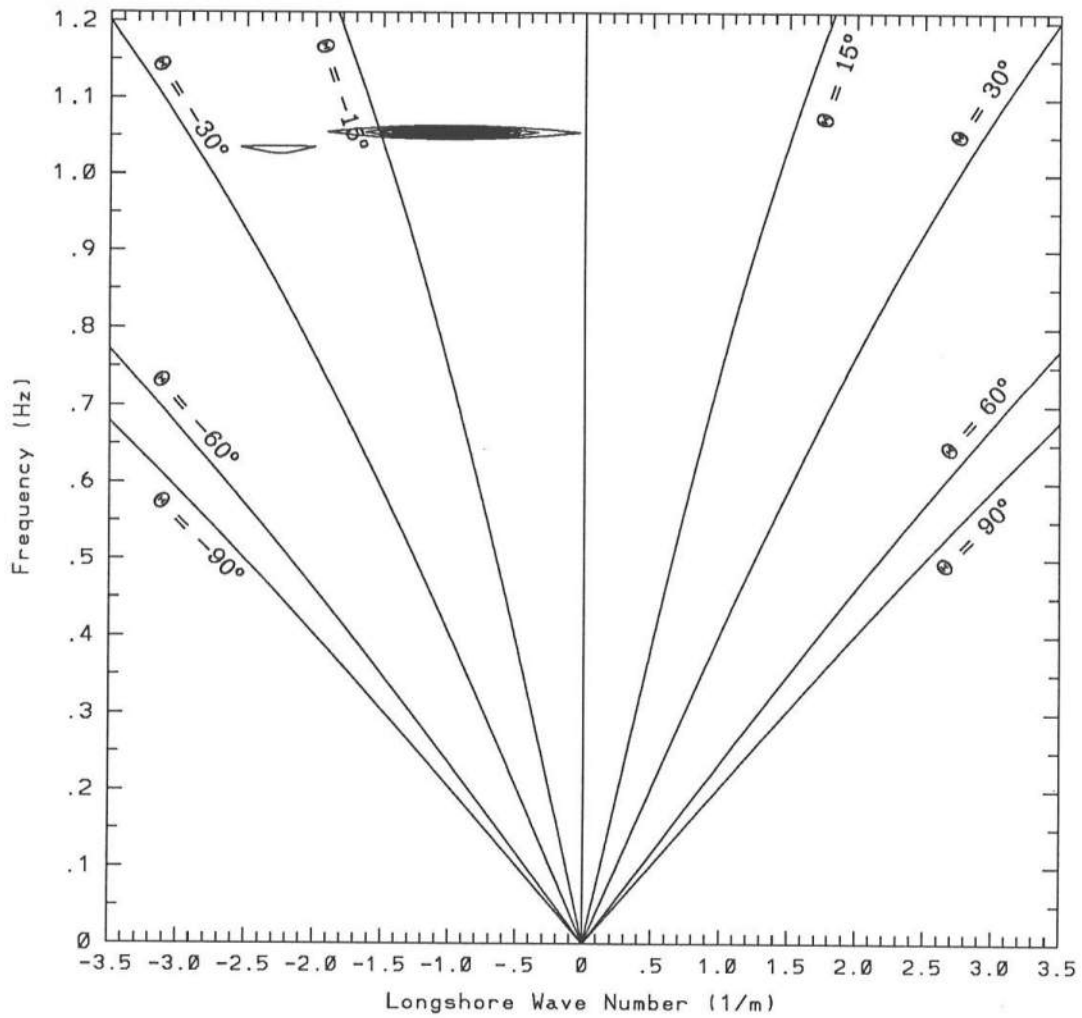
Figure 6.18: STEST: wave number–frequency spectrum obtained from MLM analysis of wave data from 3 longshore locations. 4 Bartlett segments of 1024 points, $\Delta f = 9.67 \times 10^{-3}$ Hz, $\Delta k = 0.05$ m^{-1}, 27 contours plotted.
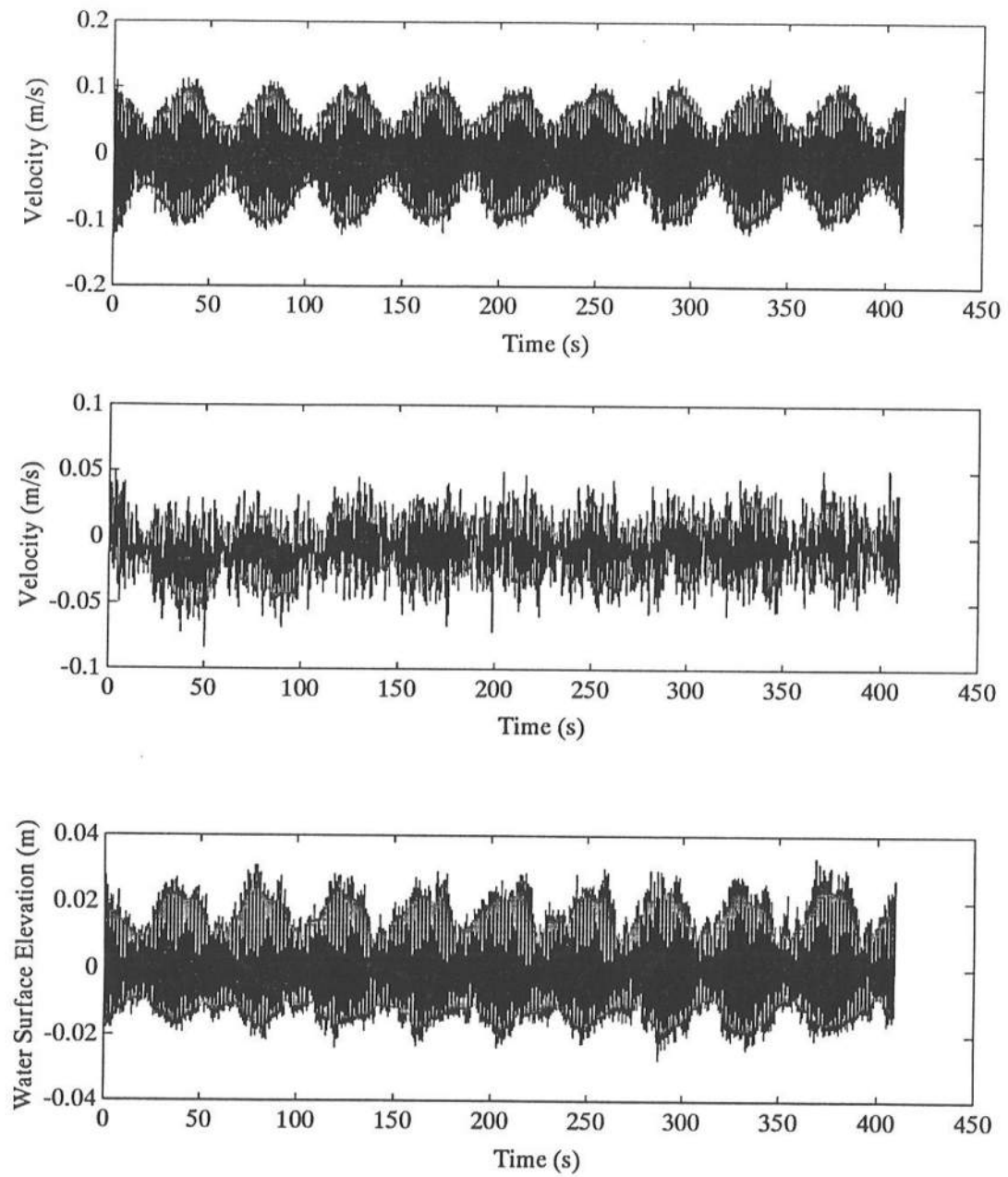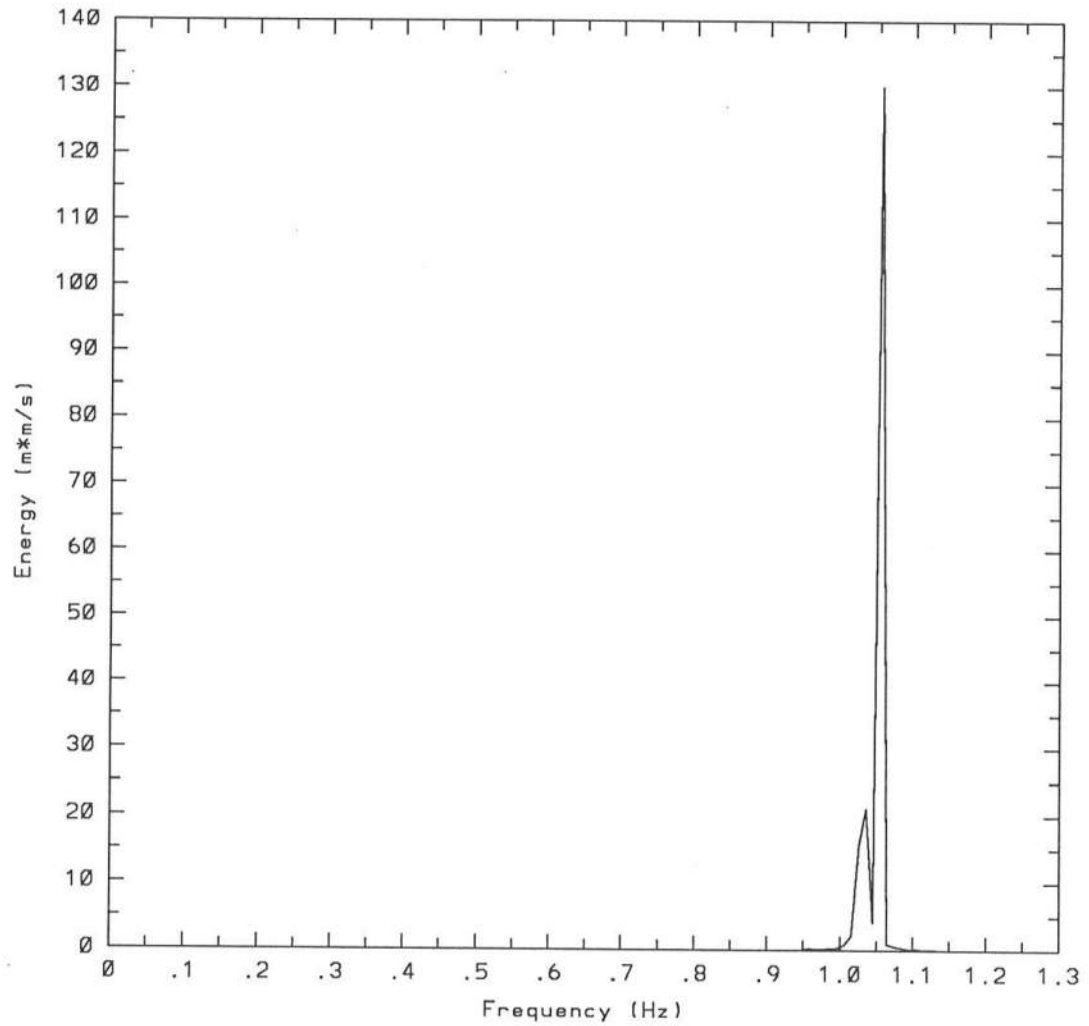
Figure 6.19: STEST: 1–D frequency spectrum obtained from the average of wave data from all 3 longshore locations. 4 Bartlett segments of 1024 points, $\Delta f = 9.67 \times 10^{-3}$ Hz.
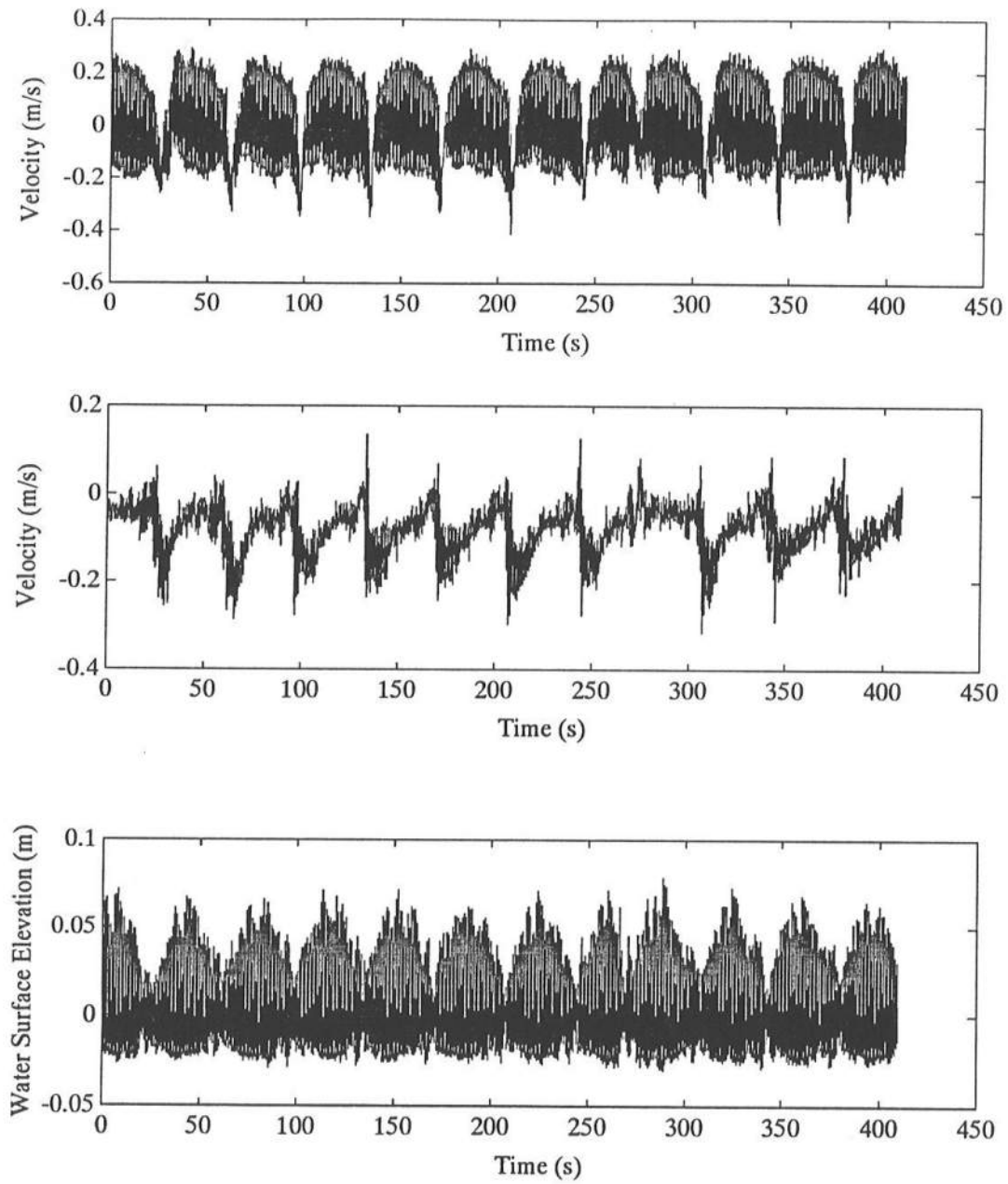
Figure 6.20: P2TEST: time series of the cross–shore velocity (top), the longshore velocity (middle), and the water surface elevation (bottom) at location N8, current meter $WE\,62$.
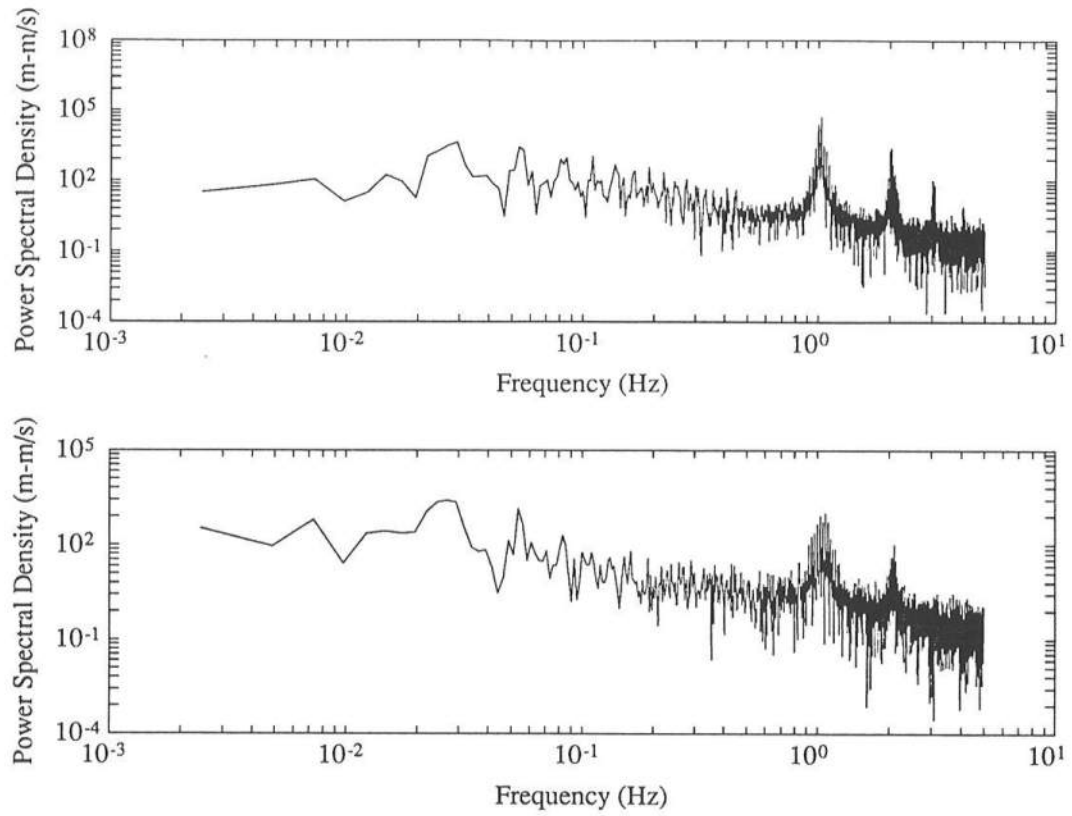
Figure 6.21: P2TEST: frequency spectrum of the cross–shore velocity (top) and the long-shore velocity time series (bottom) at location N8, current meter WE 62.

Table 6.5: Theoretical, observed and measured values of the rip current and incident wave field parameters for P2TEST.

P2TEST depth = 0.10 m	Theoretical predictions or requested values	Observed values	Measured values
T_1	1.00 s	-	0.99 s
T_2	0.97 s	-	0.98 s
θ_1	+3.00°	-	+4.21°
θ_2	−10.00°	-	−11.44°
k_1 (L_1)	6.80 m^{-1} (0.92 m)	-	6.88 m^{-1} (0.91 m)
k_2 (L_2)	7.05 m^{-1} (0.89 m)	-	6.96 m^{-1} (0.96 m)
$k_r = k_1/k_2$	0.97	-	0.99
predicted Cg_y/C_2	−0.18	-	-
$\Rightarrow Cg_y$	−16.2 cm/s	-	-
Lg_y	3.98 m	5.8–6.1 m	3.90–4.20 m
Tg	36.59 s	≈ 44 s	34.13 s
Cg_y	−10.90 cm/s	≈ −13.5 cm/s	−12.30 cm/s

into one file and analysed using the DFT method, with 2 Bartlett segments of 2048 points, $\Delta f = 0.00488$ Hz. The resulting wave number–frequency spectrum is presented in figure 6.22. For this case, all ten contours are plotted and very little noise is apparent because there are four relatively strong concentrations of energy, at a fundamental frequency and its first three harmonics, which dominate the spectrum. The frequency of the fundamental motion is 0.0293 Hz ($12\Delta f$), and the central wave number is 1.4 m^{-1} which gives a wave length of 4.48 m. The second, third and fourth harmonics have wave numbers and frequencies which are twice, three times, and four times that of the fundamental motion. A straight line can be drawn through the four concentrations of energy and the origin, the gradient of which gives a measured longshore speed of propagation of the migrating rip currents, $Cg_y = -0.13$ m/s. The theoretical longshore speed of the migrating rip currents for this test case is -0.14 m/s.

With the appearance of more harmonics, the wave number–frequency spectrum is beginning to resemble those presented in Oltman–Shay, Howd and Birkemeier (1989) (figure 2.4), although the low frequency energy in their results does not seem to display any periodicity which would indicate that it was composed of a fundamental motion and harmonics. However, the low frequency motions in both the field results and the laboratory results display a linear relationship between wave number and frequency.

The wave number–frequency spectrum derived from the MLM analysis of the wave data for this test case is presented in figure 6.23. The two energy concentrations represent the incident wave trains, and are located at the theoretically predicted rip current frequencies. In addition, the peak wave numbers of the energy concentrations give angles of incidence of -11.4° and $+4.2^\circ$, which are close to the requested values of -10° and $+3^\circ$. It is interesting to note that the measured angles of incidence are much closer to the required values for this case than for the PTEST test case. The incident wave fields for these two cases were theoretically identical, with the exception that X_m, the cross–shore location of the "clean" wave field for the designer waves generation program, was further offshore for PTEST. Reasons for this discrepancy are probably related to the wave generation program and the way in which the wave trains are reflected off the side walls and interact to form
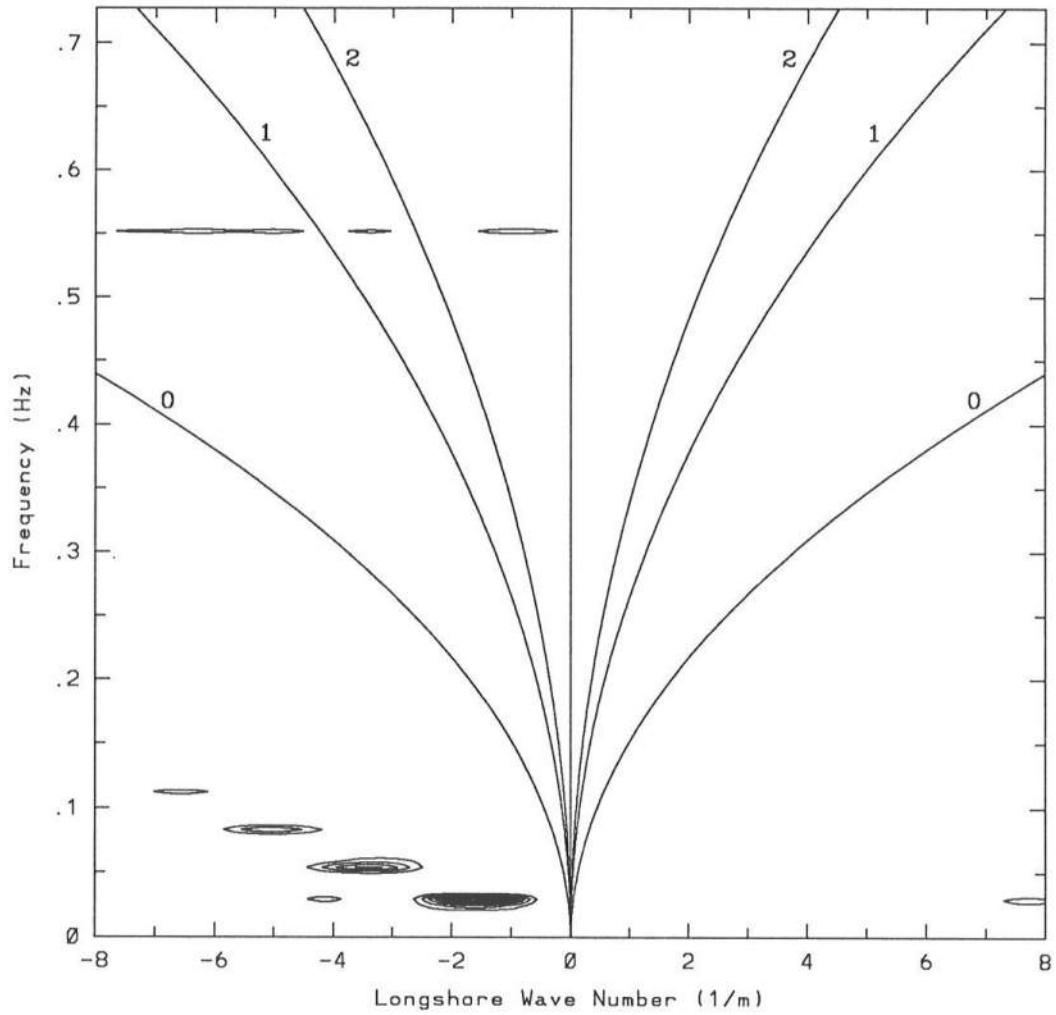
Figure 6.22: P2TEST: wave number–frequency spectrum obtained from DFT analysis of cross–shore velocity data from 10 longshore locations. 2 Bartlett segment of 2048 points, $\Delta f = 4.88 \times 10^{-3}$ Hz, $\Delta k = 0.1$ m^{-1}, 10 out of 10 contours plotted.

the desired wave field. Table 6.5 provides a full summary of theoretical and measured parameters of the incident wave trains, including the values of the rip current spacing and longshore speed of propagation that would be predicted from the measured angles of incidence for this test case.

6.7 Experimental Test Case: P2RAND

As discussed in chapter 5, section 5.2, this test case is identical to the previous one except for the addition of random waves in the same directions as the incident wave trains. The rip currents could still be seen on the beach for the majority of the time, but would occasionally disappear. However, the basic rip cell structure was still evident and the rip currents were fairly strong.

Cross–shore and longshore velocity and water surface elevation time series from one array location, N8, are presented in figure 6.24. The groups in the cross–shore velocity record and the offshore flows in the rip currents between them can still be identified, but overall, the time series is not as clean as for the previous case. The longshore velocity record displays a low frequency modulation at approximately the period of the migrating rip currents, although instead of the longshore velocities increasing gradually towards zero after the passage of a rip current (as seen in the longshore time series for P2TEST, figure 6.20) the record shows a more constant velocity with strong offshore flows occurring periodically and almost instantaneously. The water surface elevation time series displays grouping similar to and in phase with the groups in the cross–shore velocity record.

The frequency spectra of the velocity time series are presented in figure 6.25. The energy at the incident wave frequencies has a larger spread than for the P2TEST case, due to the random waves generated in the wave basin. Both spectra display some energy at low frequencies, although a peak at the predicted rip current frequency is not dominant. Indeed, the longshore velocity spectrum shows almost constant energy over a wide range of frequencies in the rip current range.

The wave number–frequency spectrum, derived from the cross–shore velocity data at all ten current meter array locations, is presented in figure 6.26. The DFT calculations
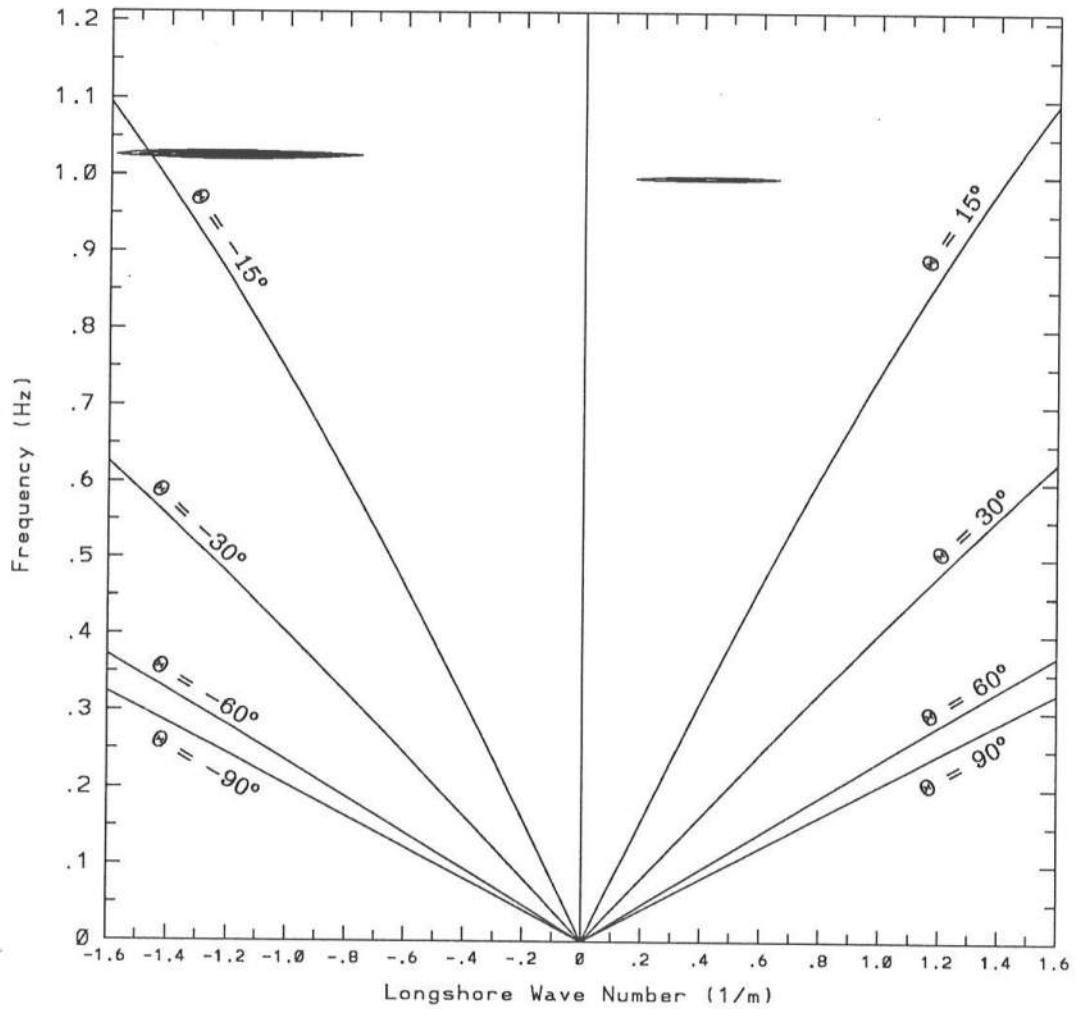
Figure 6.23: P2TEST: wave number–frequency spectrum obtained from MLM analysis of wave data from 3 longshore locations. 4 Bartlett segments of 1024 points, $\Delta f = 9.77 \times 10^{-3}$ Hz, $\Delta k = 0.025$ m^{-1}, top 6 out of 10 contours plotted.
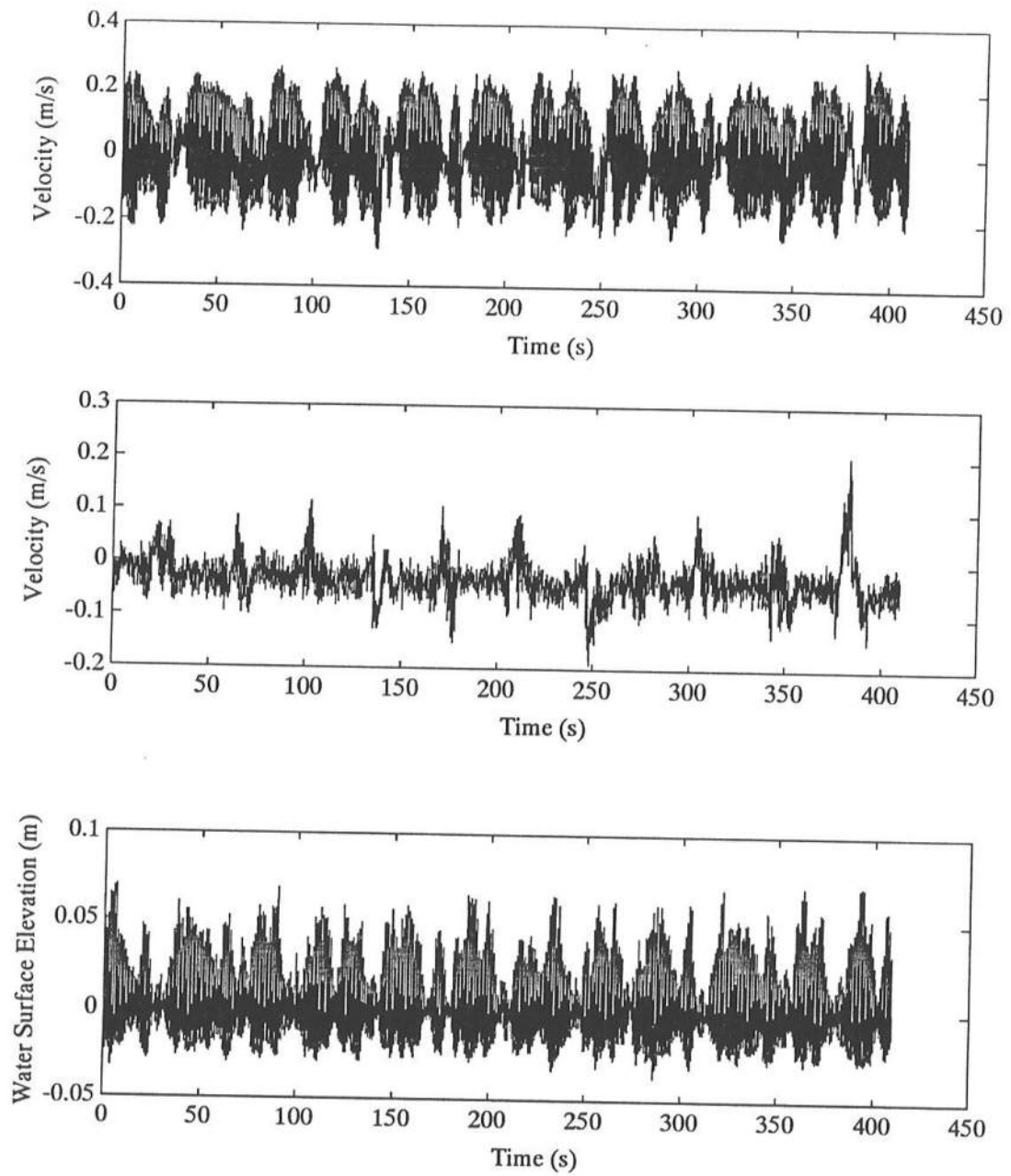
Figure 6.24: P2RAND: time series of the cross–shore velocity (top), the longshore velocity (middle), and the water surface elevation (bottom) at location N8, current meter $WE\,62$.
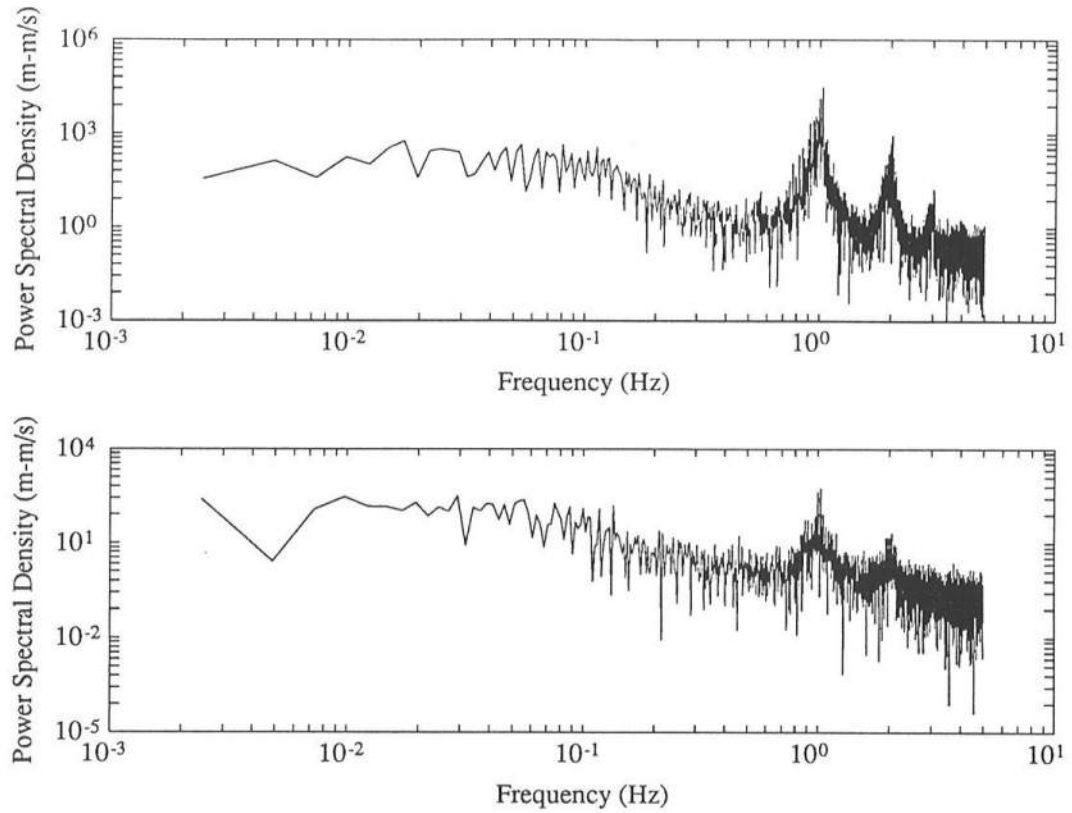
Figure 6.25: P2RAND: frequency spectrum of the cross–shore velocity (top) and the longshore velocity time series (bottom) at location N8, current meter $WE\,62$.

were made using 2 Bartlett segments of 2048 points, with $\Delta f = 0.00488$ Hz. The low frequency energy in the spectrum due to the migrating rip currents is still evident, but there is also other significant low frequency energy present, which is probably due to the interactions of the random waves. However, it is important to note that the migrating rip current generation mechanism survives interference from random waves.

The wave number–frequency spectrum based on the MLM analysis of the wave data is presented in figure 6.27, and is very similar to that of P2TEST. Energy from the random waves does not feature in the spectrum indicating their relative significance compared to the two main wave trains.

6.8 Experimental Test Case: P2DIRAND

This test case was also based on P2TEST, but included random waves with a directional spread. In the wave basin, the basic rip cell structure was still evident, although the strength of the rip currents fluctuated. The cross–shore and longshore velocity and water surface elevation time series for this experimental test case are presented in figure 6.28. Like the previous case, grouping is still evident in the cross–shore velocity record despite the presence of other components in the wave field. Strong offshore flows are present but these do not occur at regular intervals, indicating that the rip currents were not always present in the surf zone during the experiment. This is reflected in the longshore velocity time series, which shows small fluctuations about a mean with occasional increases in the velocity related to the passage of a rip current past the current meter at N8. Groups in the water surface elevation time series correspond approximately to those in the cross–shore velocity record. The frequency spectra of the cross–shore and longshore velocity records are presented in figure 6.29. As for P2RAND, the incident wave energy is spread over a range of frequencies and there are no dominant peaks in the low frequency end of the spectra.

The DFT analysis of the cross–shore velocity data from all ten array locations was computed using 2 Bartlett segments of 2048 points, with $\Delta f = 0.00244$ Hz. The resulting wave number–frequency spectrum is presented in figure 6.30 and has been plotted using
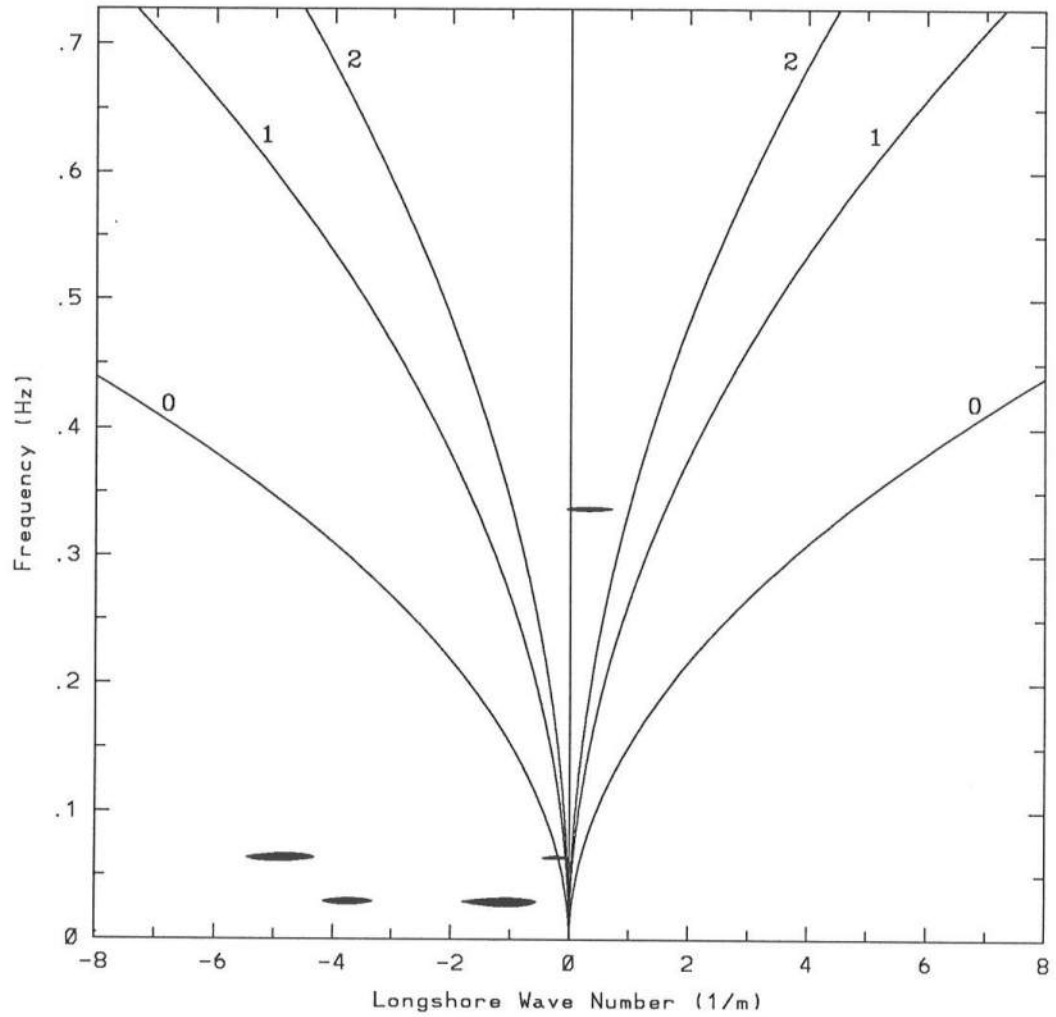
Figure 6.26: P2RAND: wave number–frequency spectrum obtained from DFT analysis of cross–shore velocity data from 10 longshore locations. 2 Bartlett segment of 2048 points, $\Delta f = 4.88 \times 10^{-3}$ Hz, $\Delta k = 0.1$ m^{-1}, top 6 out of 10 contours plotted.
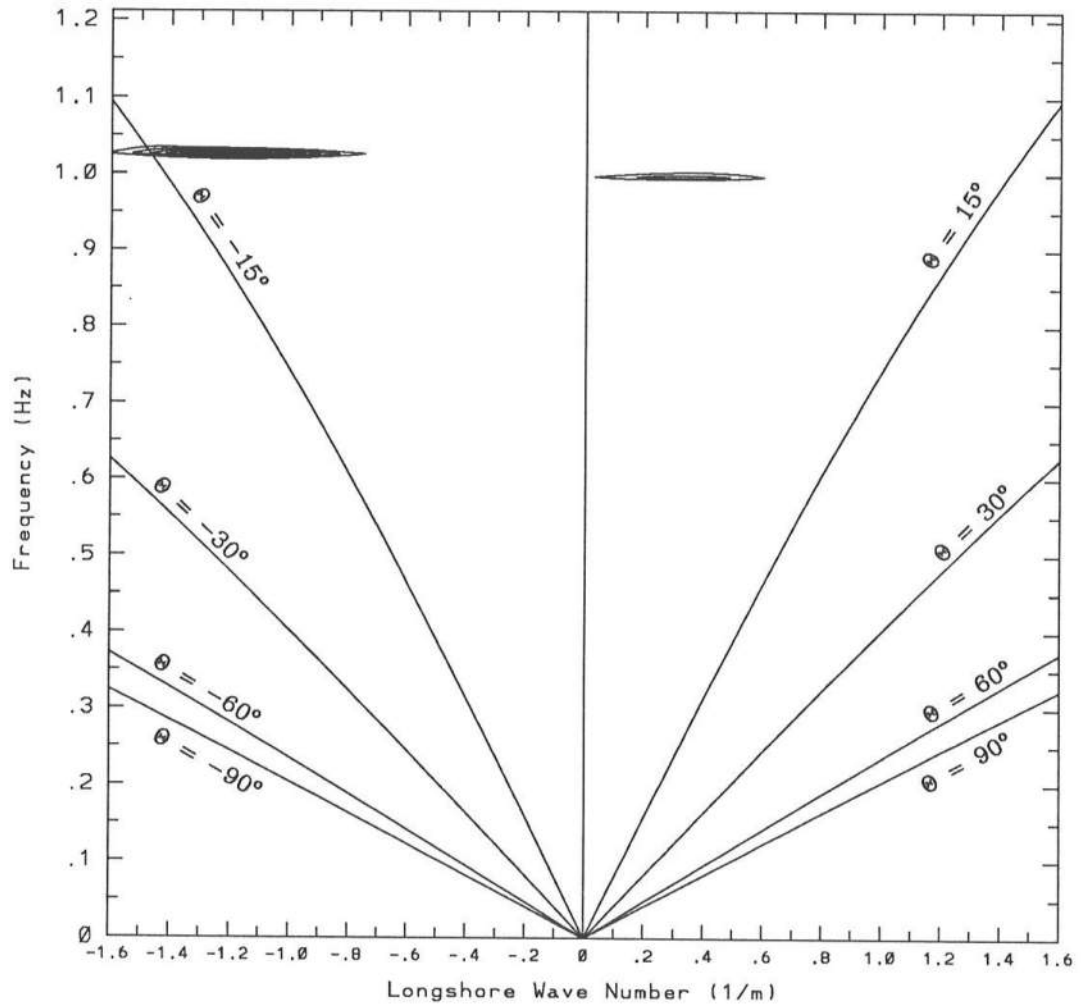
Figure 6.27: P2RAND: wave number–frequency spectrum obtained from MLM analysis of wave data from 3 longshore locations. 4 Bartlett segments of 1024 points, $\Delta f = 9.77 \text{x} 10^{-3}$ Hz, $\Delta k = 0.025$ m^{-1}, top 8 out of 10 contours plotted.
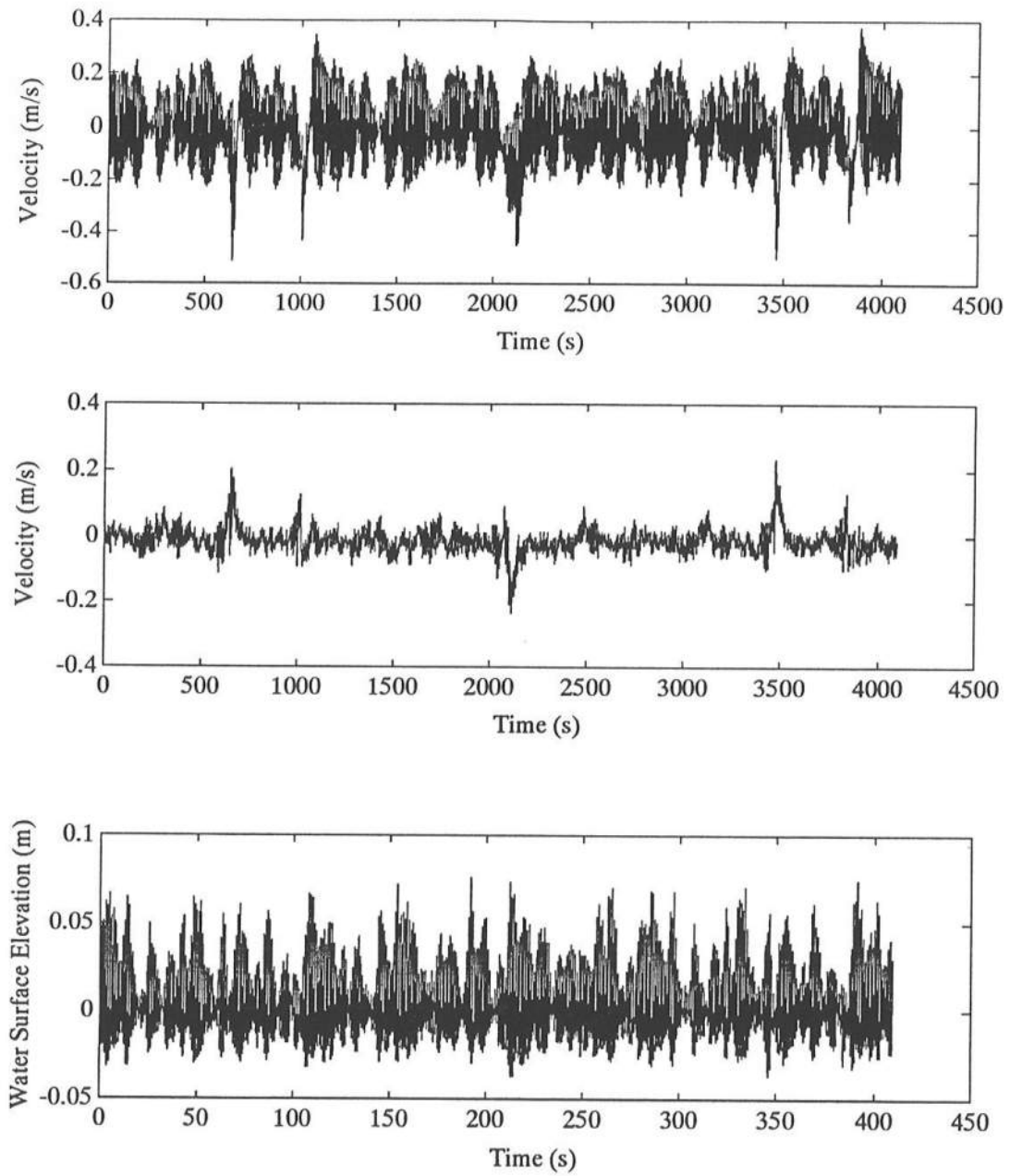
Figure 6.28: P2DIRAND: time series of the cross–shore velocity (top), the longshore velocity (middle), and the water surface elevation (bottom) at location N8, current meter $WE\,62$.
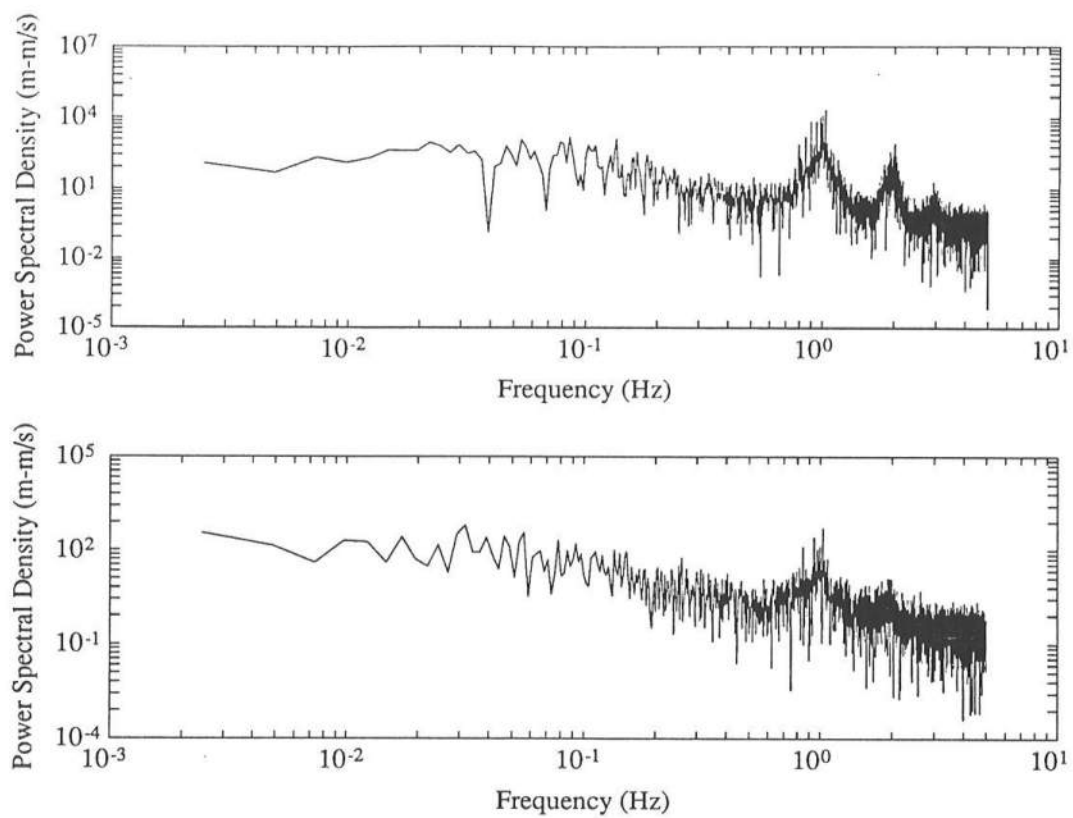
Figure 6.29: P2DIRAND: frequency spectrum of the cross–shore velocity (top) and the longshore velocity time series (bottom) at location N8, current meter $WE\,62$.

10 out of 10 contours to show all the energy concentrations. Once again, the low frequency motion due to the migrating rip currents is easily identified and is seemingly unaffected by the random waves. Indeed, there is also evidence of the second and third harmonics. In addition, there is some possible edge wave motion in the nearshore region, represented by the two concentrations of energy in the center of the graph. There is very little other energy seen in the spectrum.

The wave number–frequency spectrum based on the MLM analysis of the wave data for this test case is presented in figure 6.31. Energy is present at the two main wave train frequencies, and there is also energy at other frequencies and wave numbers which is related to the random waves. These wave components undoubtedly contribute to the generation of the low frequency motions in the nearshore region that are seen in figure 6.30.

6.9   Experimental Test Case: PQTEST

As described in chapter 5, section 5.2, this experimental test case is a direct super-position of PTEST and QTEST. In the wave basin, no clear rip cell structure could be seen, although strong, individual rip currents were observed intermittently. The dominant feature in the nearshore region was a surf beat effect. This was caused by a combination of two of the four incident wave trains lying in the horizontal family of solutions to equation 3.42, which produce nodal lines roughly parallel to the shoreline.

The cross–shore and longshore velocity and water surface elevation records for this test case are presented in figure 6.32. Short groups are seen in both the cross-shore velocity record and the water surface elevation record. However, there is a lower frequency modulation apparent in the longshore velocity record indicating the presence of rip cells in the nearshore region with periods of approximately 60 s. Such a low frequency modulation is not readily seen in the other two time series. The frequency spectra of the velocity records, presented in figure 6.33, display no dominant peaks in the lower frequencies, although there is considerable energy spread over a large range of frequencies.

The surf beat effect dominates the wave number–frequency spectrum, computed
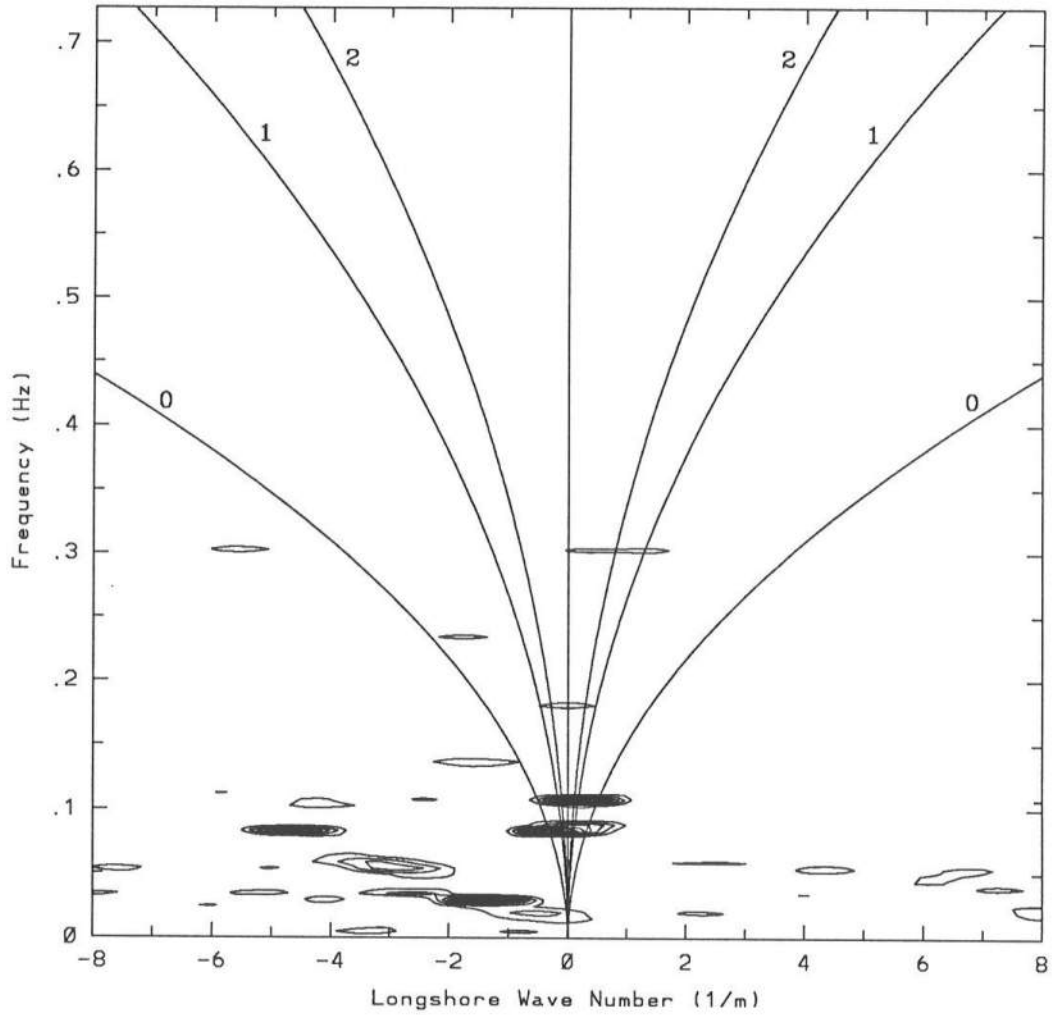
Figure 6.30: P2DIRAND: wave number–frequency spectrum obtained from DFT analysis of cross–shore velocity data from 10 longshore locations. 2 Bartlett segment of 2048 points, $\Delta f = 4.88 \times 10^{-3}$ Hz, $\Delta k = 0.1$ m^{-1}, 10 out of 10 contours plotted.
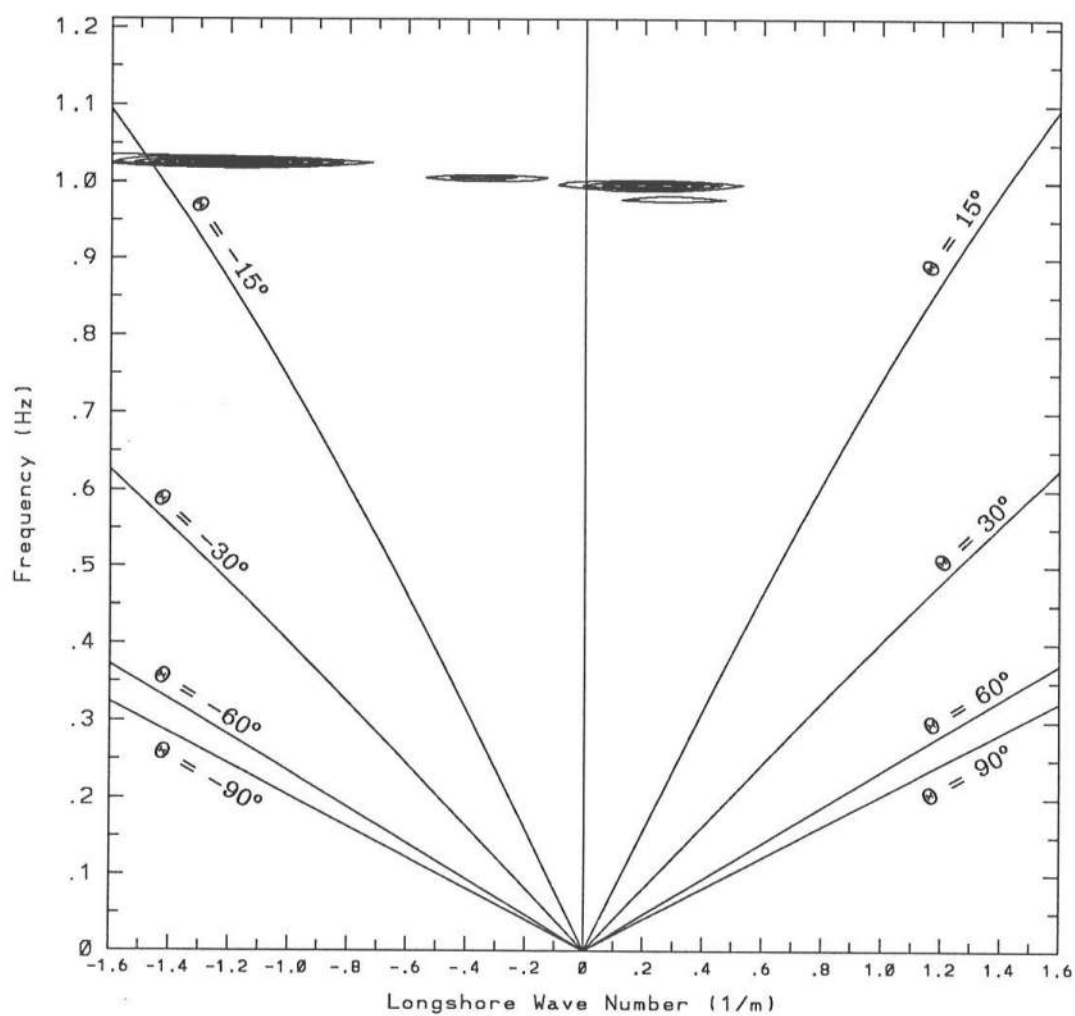
Figure 6.31: P2DIRAND: wave number–frequency spectrum obtained from MLM analysis of wave data from 3 longshore locations. 4 Bartlett segments of 1024 points, $\Delta f = 9.77 \times 10^{-3}$ Hz, $\Delta k = 0.025$ m^{-1}, top 8 out of 10 contours plotted.
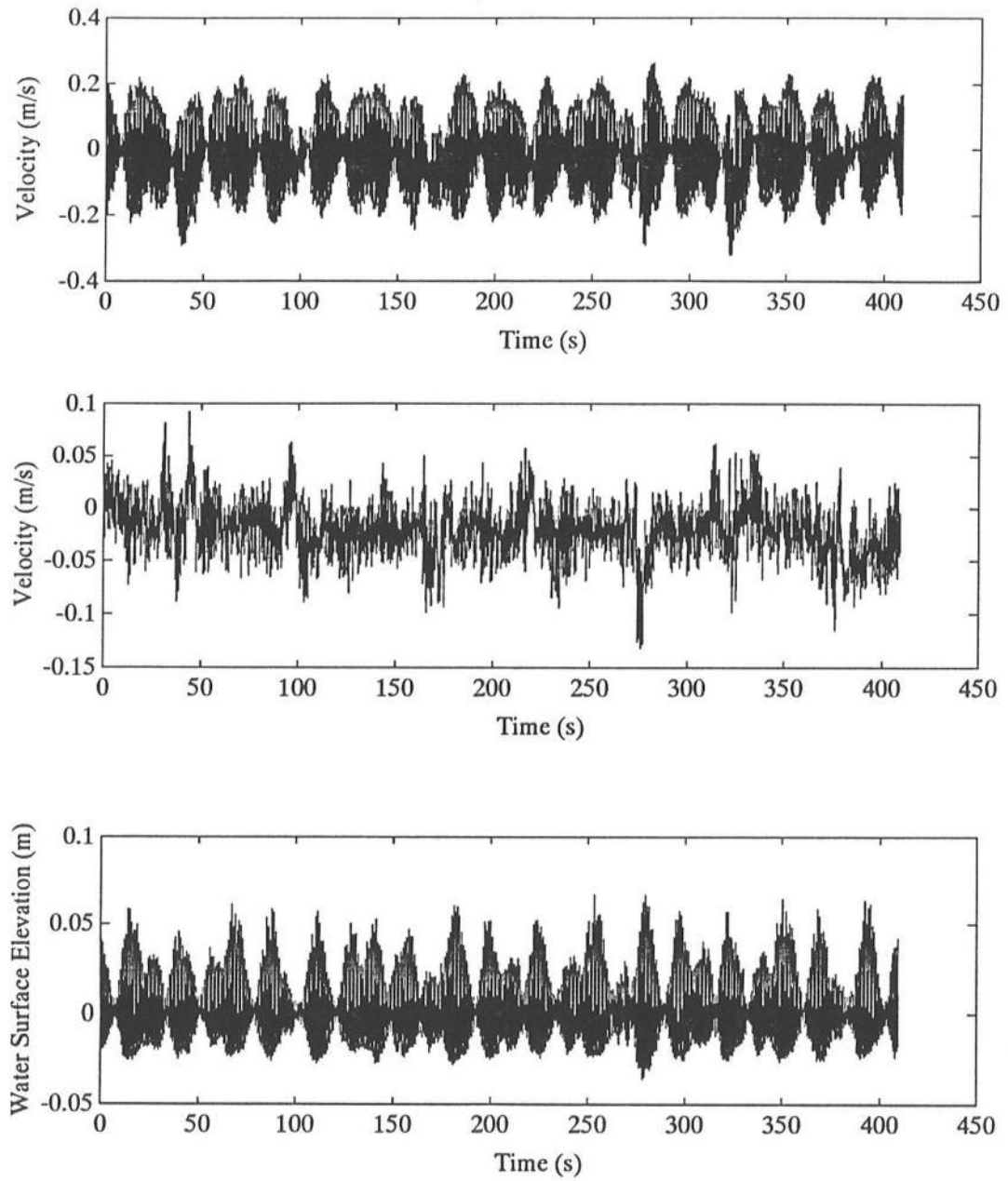
Figure 6.32: PQTEST: time series of the cross–shore velocity (top), the longshore velocity (middle), and the water surface elevation (bottom) at location N8, current meter $WE\,62$.
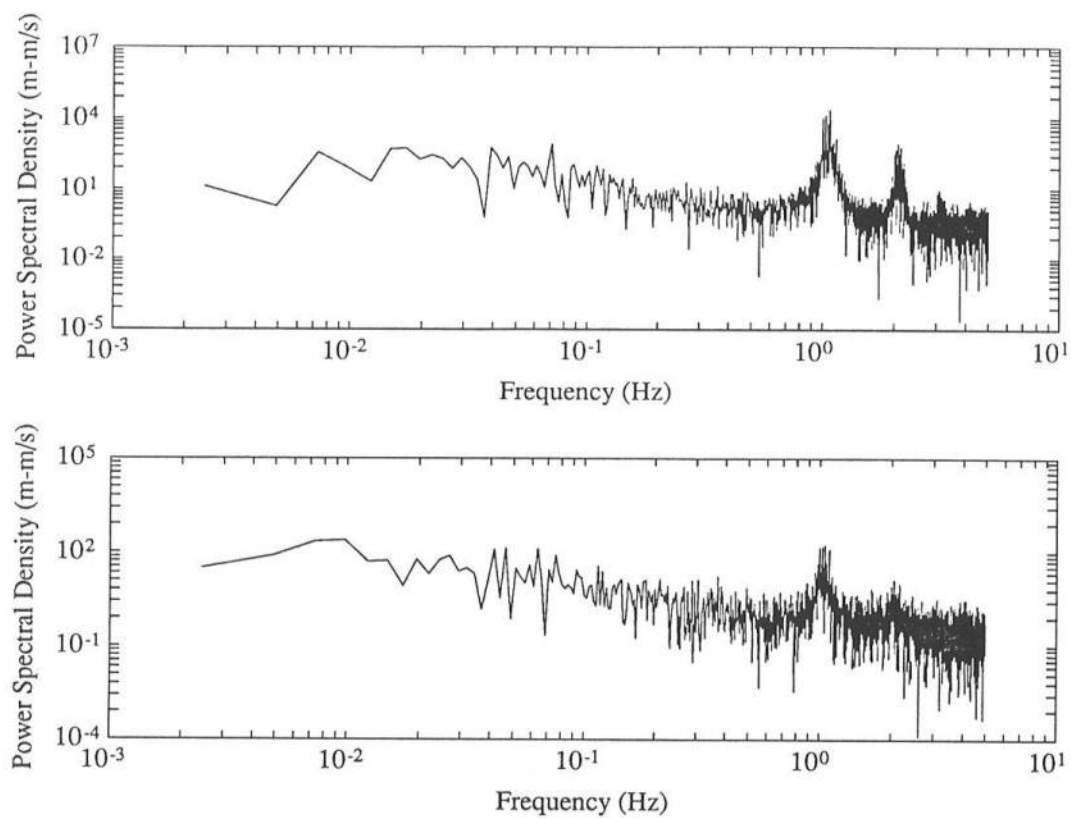
Figure 6.33: PQTEST: frequency spectrum of the cross–shore velocity (top) and the longshore velocity time series (bottom) at location N8, current meter *WE* 62.

from the cross–shore velocity data and presented in figure 6.34. There is a strong concentration of energy with a longshore wave number of almost zero. This suggests a very long, or possibly infinite, longshore wave length, as would be expected for a purely on/offshore motion. There is some energy in the spectrum at other wave numbers and frequencies, away from the edge wave dispersion relationship curves, but it is not very strong. The corresponding wave number–frequency spectrum computed from the longshore velocity data yields little more information, although there is some energy at $f \approx 0.04$ Hz, and with a central longshore wave number of 1.2 m^{-1}, suggesting that there are rip currents migrating toward the southern end of the beach. The two rip cell structures from PTEST and QTEST have obviously been destroyed, resulting in little significant low frequency motion in the nearshore region. The wave number–frequency spectrum based on the longshore velocity data was computed, but the results were very similar. The MLM analysis of the wave data, presented in figure 6.4, shows the four incident wave trains generated in the basin as expected.

6.10 Evaluation of Experimental Repeatability

One of the major assumptions made during the laboratory testing of the rip current generation mechanism was that each experimental run was perfectly repeatable. The experimental work required simultaneous data collection from ten locations in the nearshore region, but there were only two currents meters available. So, each experimental test case had to be run five times with the current meters placed at two different locations for each run.

Having assumed the experimental runs were perfectly repeatable, it was considered necessary to check that repeatability. This was done by looking at the longshore and cross–shore velocity records from one of the experimental test cases, for each current meter, at an arbitrarily selected location within the longshore array. Every experimental run performed in the wave basin was repeated, so two "identical" records were available for comparison for each run.

For current meter $WE\,27$, the cross–shore and longshore velocity records at location
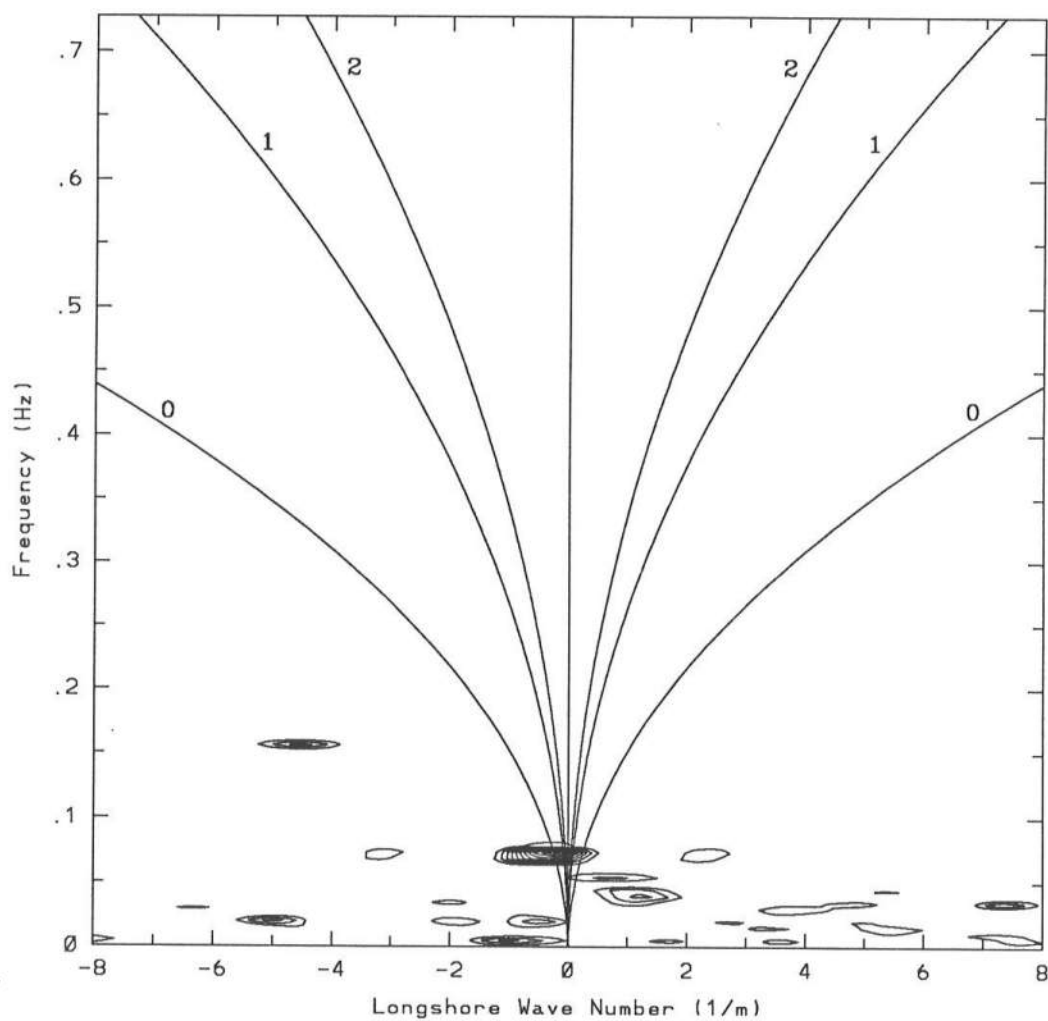
Figure 6.34: PQTEST: wave number–frequency spectrum obtained from DFT analysis of cross–shore velocity data from 10 longshore locations. 2 Bartlett segment of 2048 points, $\Delta f = 4.88 \times 10^{-3}$ Hz, $\Delta k = 0.1$ m^{-1}, 10 out of 10 contours plotted.
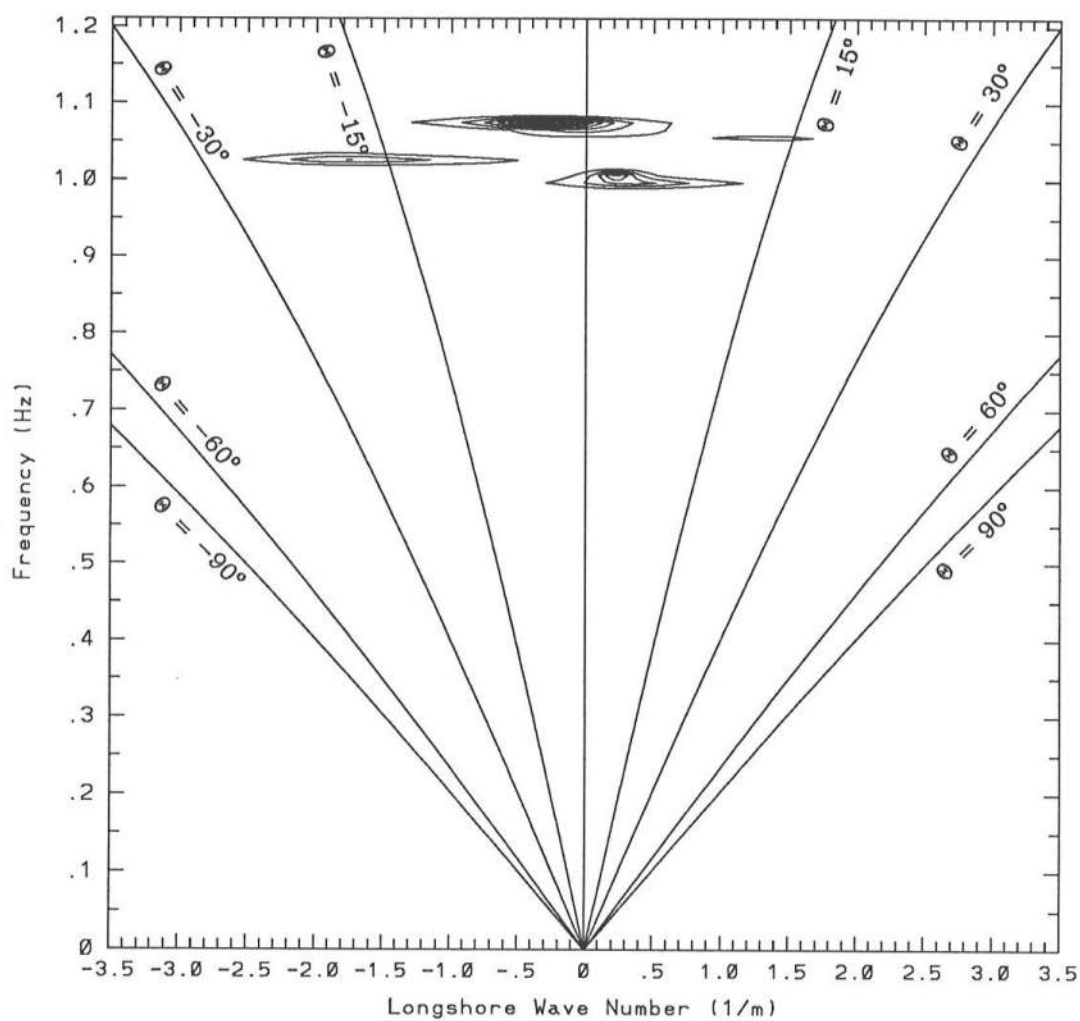
Figure 6.35: PQTEST: wave number–frequency spectrum obtained from MLM analysis of wave data from 3 longshore locations. 4 Bartlett segments of 1024 points, $\Delta f = 9.77 \times 10^{-3}$ Hz, $\Delta k = 0.05$ m^{-1}, 10 out of 10 contours plotted.

N5, for the P2TEST experimental test case, were reviewed. Sections of the time series for both cross–shore and longshore velocities are presented in figure 6.36. The two cross–shore velocity records match very well with only some velocity magnitude discrepancies occurring during the passage of the rip current past the current meter ($time$ = 15 s to $time$ = 20 s). However, the agreement between the longshore velocity records is not as good. It should be noted that the velocities in the longshore direction are considerably smaller than those in the cross–shore direction, and are therefore much more susceptible to electrical noise or turbulent fluctuations in the nearshore currents.

Quantifiable comparisons between the two longshore and cross–shore records were made by computing their coherences. For perfectly identical records, the coherence between them should be unity over all frequencies. The graph of coherence vs. frequency for the two cross–shore velocity records is presented in figure 6.37. The coherence at low frequencies is very good for this case, although it decreases with increasing frequency. However, the coherence rises almost to unity at the incident wave frequencies. Beyond this, the coherence decreases, but these frequencies are not important to the present study.

The coherence between the two longshore records is, in general, not as good as it was for the cross–shore records. Figure 6.38 shows that there is a peak of coherence at approximately the rip currents frequency and again around the incident wave frequencies. The lack of coherence between the two longshore records at other frequencies is probably due to the inability of the current meters to accurately read the low longshore velocities. The results for the other current meter, $WE\,62$, were very similar, with better low frequency coherence for the longshore velocity records. The graphs of coherence vs. frequency for the cross–shore and longshore velocity records for this current meter are presented in figures 6.39 and 6.40 respectively.

In general, the coherence between the records was good at the frequencies which were important to the investigation of migrating rip currents, i.e., the incident wave frequencies and the rip current frequencies. These results support the assumption of experimental repeatability with the reservation that the analysis of the data should be confined to those frequencies.
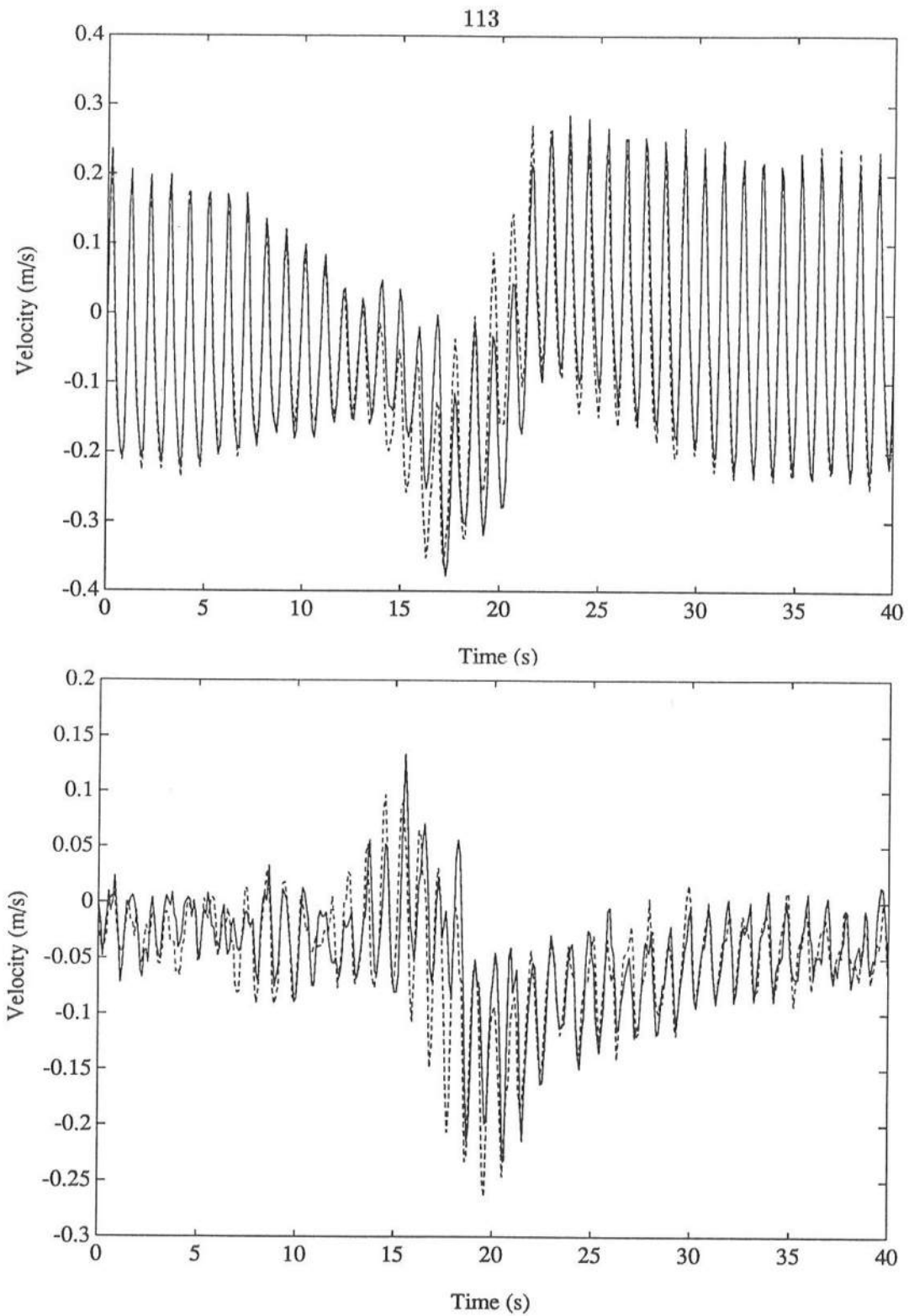
Figure 6.36: Time series (partial record) of two cross–shore velocity (top) and longshore velocity (bottom) records from experimental test case P2TEST, location N5, current meter $WE\,27$.
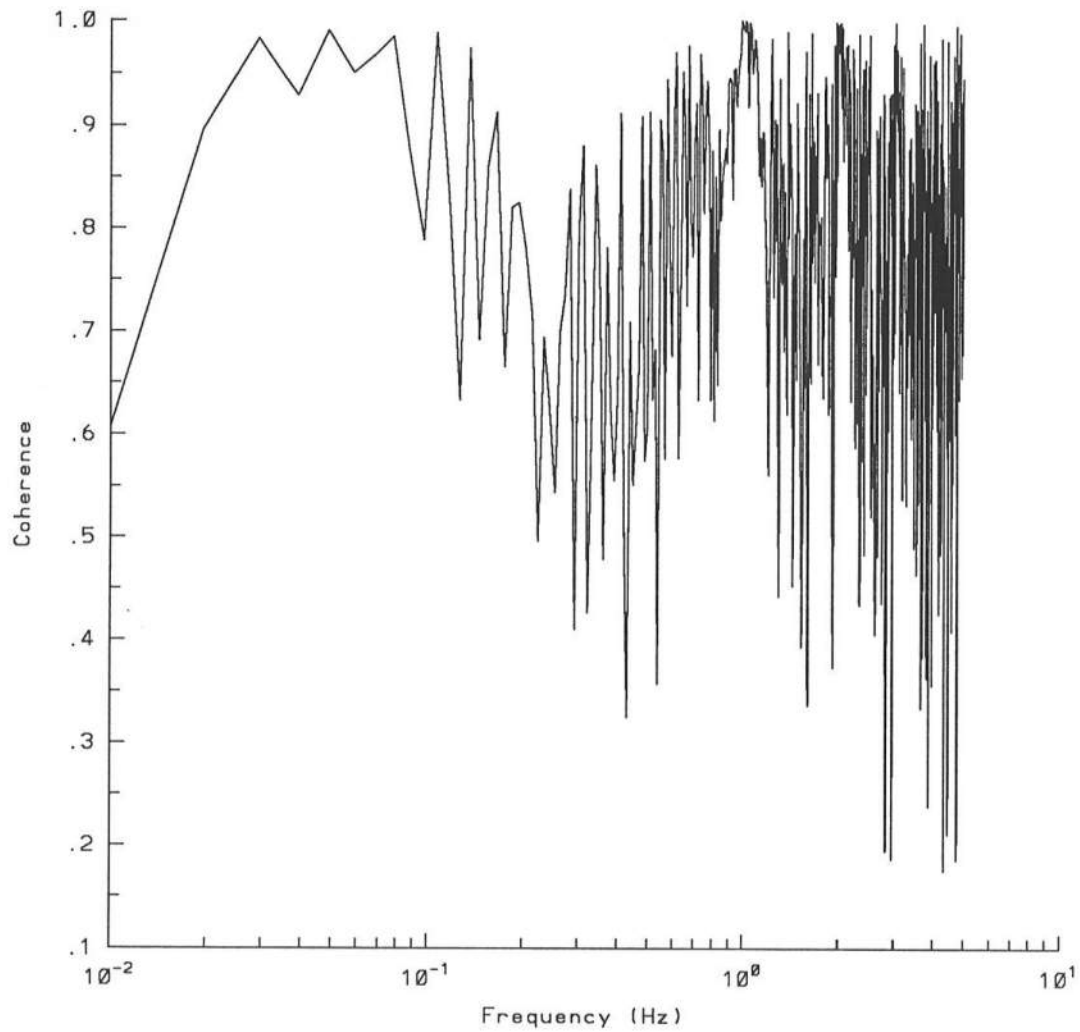
Figure 6.37: Coherence between two cross–shore velocity records from experimental test case P2TEST, location N5, current meter $WE\,27$, 4 Bartlett segments of 1024 points.
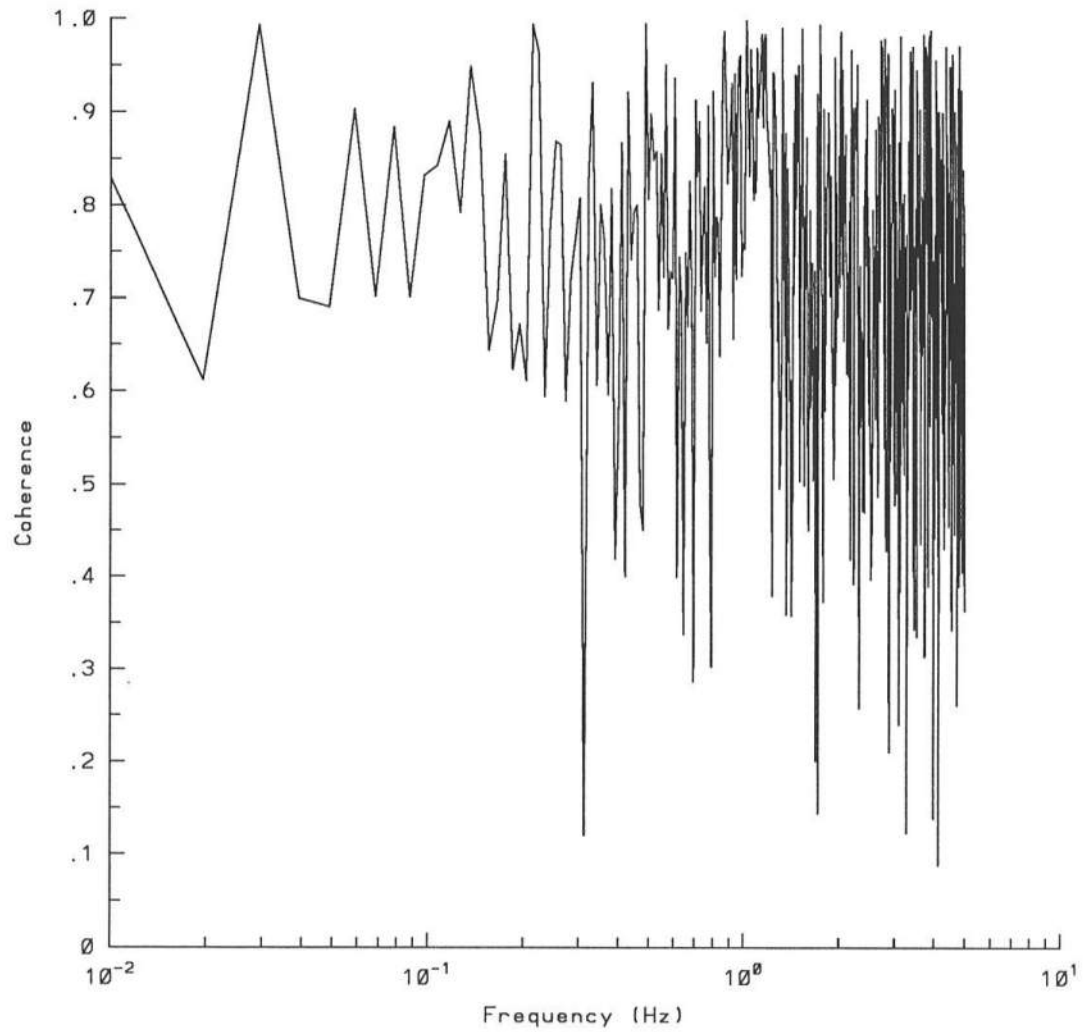
Figure 6.38: Coherence between two longshore velocity records from experimental test case P2TEST, location N5, current meter $WE\,27$, 4 Bartlett segments of 1024 points.
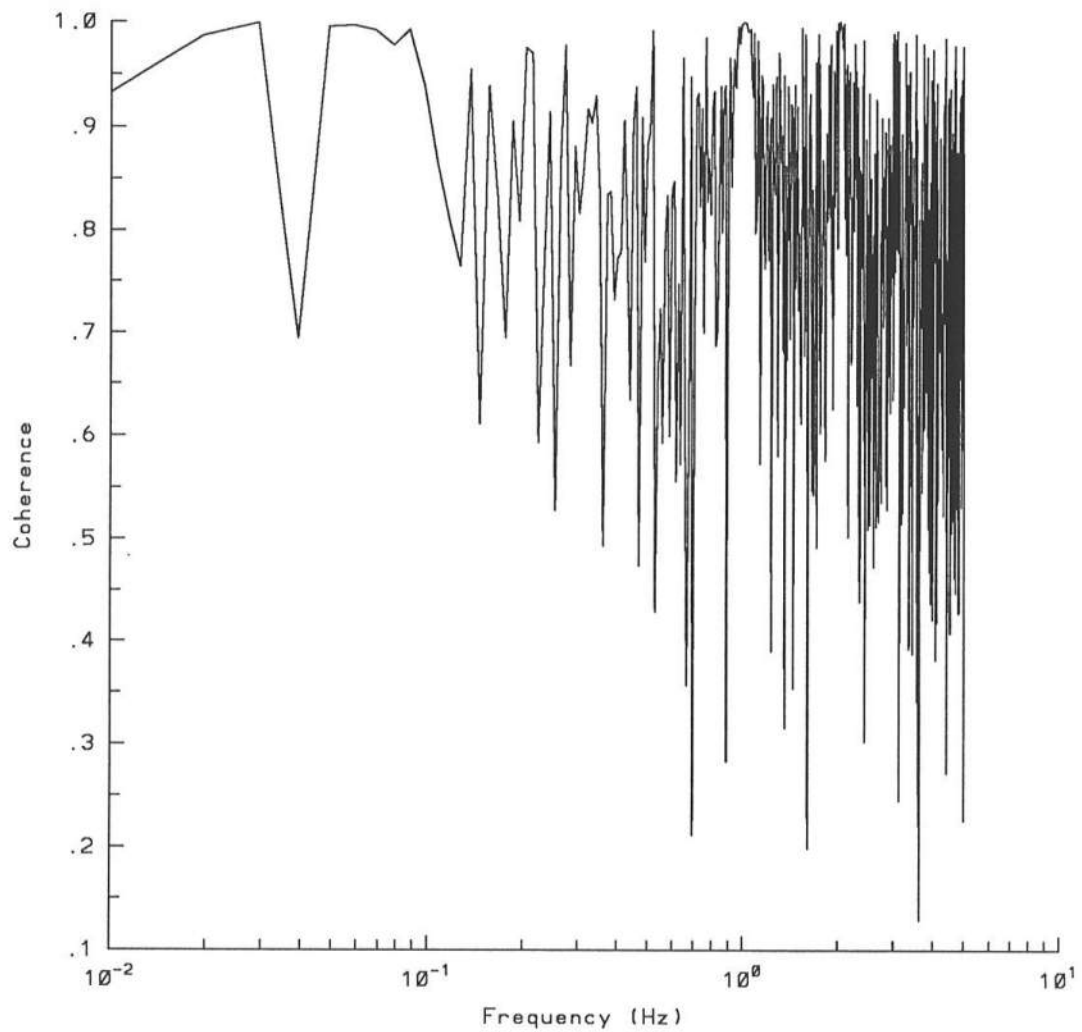
Figure 6.39: Coherence between two cross–shore velocity records from experimental test case P2TEST, location N5, current meter $WE\,62$, 4 Bartlett segments of 1024 points.
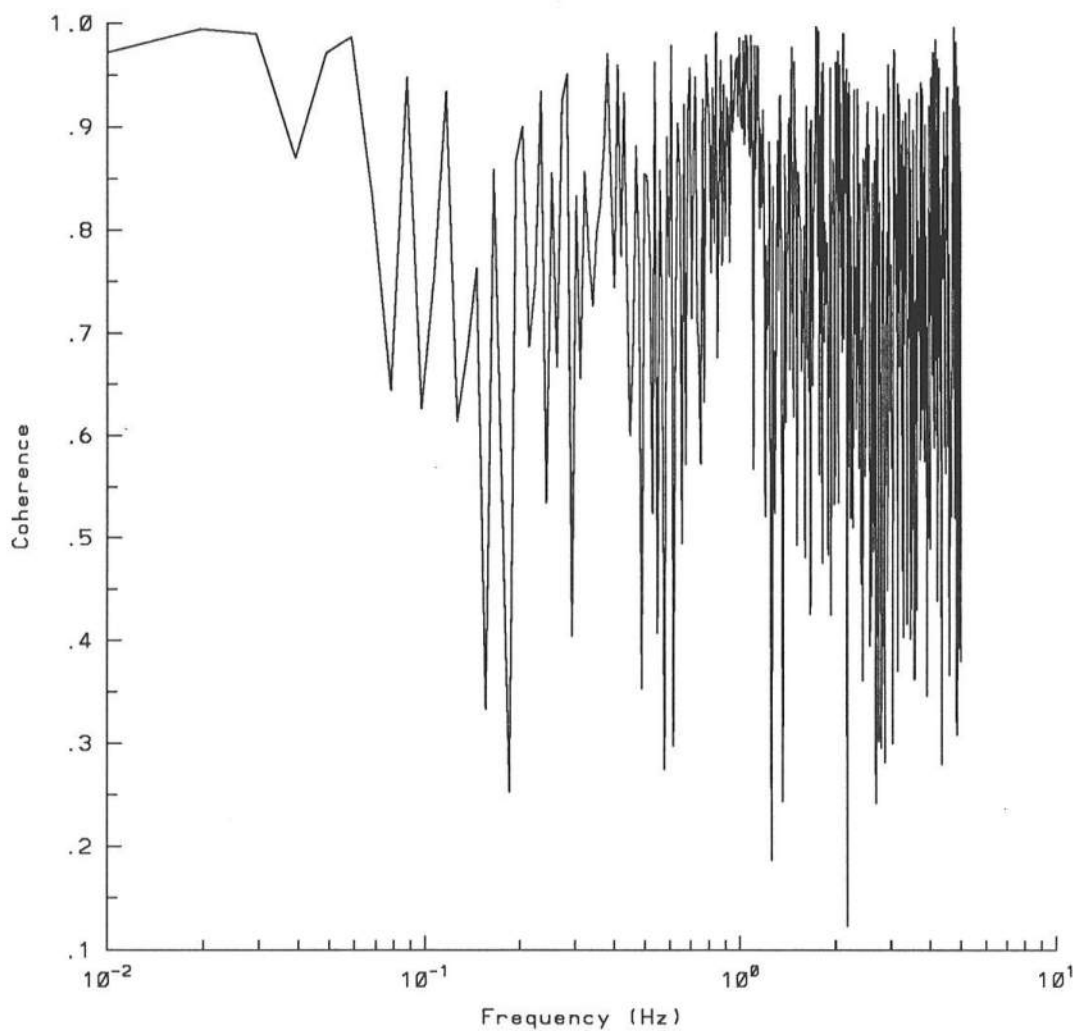
Figure 6.40: Coherence between two longshore velocity records from experimental test case P2TEST, location N5, current meter $WE62$, 4 Bartlett segments of 1024 points.

Chapter 7

SUMMARY AND CONCLUSIONS

Features of the nearshore circulation system have traditionally been characterized as stationary processes, such as longshore, cross–shore and rip currents, or unsteady processes, such as surf beat, edge waves, and the recently discovered far infra–gravity motions. From the research work described herein, incident wave groups have been shown to be very important to the dynamics of the nearshore circulation system. Attention was focused on incident wave groups, the development of a generation mechanism for migrating rip currents, and the low frequency reponse of the nearshore circulation system.

Simple, linear wave theory was used to develop the mechanism for migrating rip currents. Based on two incident wave trains with similar, but not identical frequencies, expressions for the total free surface elevation, η_t, and the wave group envelope were developed. Under certain conditions, these envelopes propagate through the nearshore region with their nodal lines intersecting the beach at angles close to the beach normal. As a result, there are longshore variations in wave height at the shoreline which create unbalanced hydrostatic forces in the nearshore region. Consequently, currents flow from the regions of high waves to regions of low or zero wave heights, causing the development and maintainance of rip currents there. As the longshore variations in wave height move slowly through the wave field, so the rip currents migrate slowly along the beach. A similar mechanism, for incident wave trains of the same frequency, leading to the development of stationary rip currents has already been proven. Experiments conducted in the directional wave basin at the University of Delaware have now confirmed this new, derivative mechanism for the generation of *migrating* rip currents. Eight different experimental test cases were designed and run. Visual observations of the response of the nearshore circulation

118

system were made and longshore and cross–shore velocities were measured at ten locations along the beach. Wave data were collected at three locations.

The longshore spacing of the rip currents can be predicted, and the experimental results and visual observations generally confirmed the predictions to within ±10%. The theory predicted the cross–shore and longshore velocities to be out of phase by 180°, a phenomenon previously observed in the field. This was confirmed qualitatively, except for one of the test cases which was unique in having both wave trains incident from the same side of the beach normal.

The longshore and cross–shore velocity data from all ten instrument locations were analysed in wave number–frequency space. The rip currents migrating along the beach produced a signature in the wave number–frequency spectrum which defines them as very low frequency motion in the nearshore region. The energy due to this motion is not a result of edge waves as it does not fall on, or near, any of the edge wave dispersion relationship curves. Instead, it has wave lengths that are significantly shorter than required for edge waves at the same frequencies. When analysed in wave number–frequency space, the velocity data from one test case which exhibited particularly strong, narrow rip currents, revealed a fundamental low frequency motion, and three harmonics at increasing frequencies and wave numbers. The four concentrations of low frequency energy on the wave number–frequency spectrum were in a straight line passing through the origin, the gradient of which corresponded closely to the longshore speed of propagation of the rip currents.

Similar low frequency motion has been observed in the nearshore region at beaches in California and North Carolina. Tang and Dalrymple (1989) found concentrations of low frequency energy at a single wave length and frequency, similar to the majority of the experimental results described in this thesis. They suggested this was due to the passage of rip currents through the surf zone as seen at the time of the field experiment. Oltman-Shay, Howd and Birkemeier (1989) also found low frequency motion in the nearshore region, but over a continuous range of frequencies and linearly dependent wave numbers. They proposed that these motions and those observed by Tang and Dalrymple were due

to longshore progressive shear waves, with a restoring force of vorticity.

The results of the experimental work presented in this thesis have demonstrated that offshore, incident wave groups can force a response of the nearshore circulation system in the form of migrating rip currents. In turn, these migrating rip currents are observed as very low frequency motion in the nearshore region which, if generated on a prototype scale, would be categorised in the previously named "FIG", or far infragravity, energy band. Therefore, it is proposed that migrating rip currents are a valid addition to shear waves as a generation mechanism for very low frequency motion in the nearshore region.

The practicality of migrating rip currents as a far infra–gravity energy generation mechanism has already been proven through Tang and Dalrymple's results from the field experiments in California. Offshore islands influence the nature of the incident wave field at Torrey Pines Beach and narrow incident wave spectra from two directions are not uncommon. The intersection of wave trains from two different storm systems could also provide suitable conditions for the generation of migrating rip currents.

Future research should include consideration of how to uniquely identify the two generation mechanisms for very low frequency motion, shear waves and migrating rip currents, in the field. Also, further investigation into the response of the nearshore region to incident wave groups with significant frequency and directional spread should be made to determine the limitations on the incident wave field for migrating rip currents to be generated and maintained in the nearshore region.

BIBLIOGRAPHY

Barber, N.F. (1961). "The directional resolving power of an array of wave detectors," in *Ocean Wave Spectra*, Prentice Hall, Inc., Englewood Cliffs, New Jersey, 137–150.

Biesel, F. (1952). "Équations générales au second ordre de la houle irrégulière." *La Houille Blanche*, 7, 372–376.

Bowen, A.J. and Guza, R.T. (1978). "Edge waves and surf beat." *J. Geophys. Research*, 83, C4, 1913–1920.

Bowen, A.J. and Holman, R.A. (1989). "Shear instabilities of the mean longshore current; 1. Theory." *J. Geophys. Research*, 94, C12, 18023–18030.

Capon, J., Greenfield, R.J. and Kolker, R.J. (1967). "Multidimensional maximum-likelihood processing of a large aperture seismic array." *Proceedings, IEEE*, 55, 192–211.

Crowson, R.A., Birkemeier, W.A., Klein, H.M., and Miller, H.C. (1988). "SUPERDUCK nearshore processes experiment: Summary of studies C.E.R.C. Field Research Facility." *Tech. Rep. C.E.R.C.-88-12*, Coastal Engng. Res. Cent., Vicksburg, Mississippi.

Dalrymple, R.A. (1975). "A mechanism for rip current generation on the open coast." *J. Geophys. Research*, 50, 24, 3485–3487.

Dalrymple, R.A. and Lanan, G.A. (1976). "Beach cusps formed by intersecting waves." *Geol. Soc. of America Bulletin*, 87, 57–60.

Dalrymple, R.A. (1978). "Rip currents and their causes." *Proc. 16th Intl. Coastal Engineering Conf.*, A.S.C.E, Hamburg, 2, 1414–1427.

Dalrymple, R.A. (1989). "Directional wavemaker theory with sidewall reflection." *J. Hydraulic Research*, 27, 1, 23–34.

Dean, R.G., and Dalrymple, R.A. (1984) *Water Wave Mechanics for Engineers and Scientists*, Prentice–Hall, Englewood Cliffs, New Jersey.

121

Gallagher, B. (1971). "Generation of surf beat by nonlinear wave interactions." *J. Fluid Mechanics*, 49, 1–20.

Guza, R.T., and Davis, R.E. (1974). "Excitation of edge waves by waves incident on a beach." *J. Geophys. Research*, 79, 9, 1285–1291.

Kim, C.S., and Huntley, D.A. (1986). "On time delays in the nearshore zone between on-shore and longshore currents at incident wave frequencies." *J. Geophys. Research*, 91, C3, 3967–3978.

Harkins, G.S., (1991). "Sensitivity analysis for multi–element wavemakers," thesis to be presented to the University of Delaware, Newark, Delaware, in 1991, in partial fulfillment of the requirements for the degree of Master of Applied Sciences.

Huntley, D.A., Guza, R.T., and Thornton, E.B. (1981). "Field observations of surf beats; 1. Progressive edge waves." *J. Geophys. Research*, 86, C7, 6451–6466.

Leech, J. (1956). "On the representation of 1, 2, $\cdots$, n by differences." *London Math. Soc. Journal*, 31, 160–169.

Longuet–Higgins, M.S., and Stewart, R.W. (1962). "Radiation stress and mass transport in gravity waves, with application to 'surf beats'", *J. Fluid Mechanics*, 13, 481–504.

Longuet–Higgins, M.S., and Stewart, R.W. (1964). "Radiation stress in water waves; a physical discussion, with applications", *Deep Sea Res.*, 11, 529–562.

Muir Wood, A.M., and Fleming, C.A. (1981). *Coastal Hydraulics*, Halstead Press, John Wiley and Sons, Inc. , New York.

Munk, W.H. (1949) "Surf beats." *Trans. Am. Geophys. Union*, 30, 849–854.

Oltman–Shay, J., Howd, P.A., and Birkemeier, W.A. (1989). "Shear instabilities of the mean longshore current; 2. Field observations." *J. Geophys. Research*, 94, C12, 18031–18042.

Tang, E.C.-S., and Dalrymple, R.A. (1989). "Nearshore circulation: Rip currents and wave groups," in *Nearshore sediment transport study*, R.J. Seymour ed., Plenum Press.

Tucker, M.J. (1950) "Surf beats: sea waves of 1 to 5 min. period." *Proc. Royal Soc.*, A202, 565–573.

U.S. Army Engineer Waterways Experiment Station Coastal Research Center, (1984). *Shore Protection Manual*, 4th edition, U.S. Government Printing Office, Washington D.C., 20402.

Vincent, C.L., and Briggs, M.J. (1989). "Refraction–diffraction of irregular waves over a mound." *J. Waterway, Port, Coastal and Ocean Engng.*, A.S.C.E., 115, 2, 269–284.

Wright, L.D., Guza, R.T., and Short, A.D. (1982). "Dynamics of a high–energy dissipative surf zone." *Mar. Geol.*, 45, 41–62.

Appendix A

CALIBRATION OF ELECTROMAGNETIC CURRENT METERS

Table A.1: Experimental details for calibration of current meter $WE\,62$, x–direction.

File name	Central frequency f_c (Hz)	Bandwidth Δf	Sampling frequency f_s (Hz)	Wave height at breaking (m)	Distance of breaker point from wavemaker X_b (m)
xr162.dat	0.71	0.75	100	0.30	20.0
xr562.dat	1.10	1.00	100	0.20	20.0
xt662.dat	1.10	1.00	50	0.20	20.0
xl162.dat	0.30	0.40	50	0.30	20.0
xl262.dat	0.25	0.30	50	0.30	20.0

Equation for calibration curve (best fit straight line):

$$y = 2.7217 - 0.0737x$$

124

Figure A.1: Experimental calibration data for current meter $WE\,62$, x-direction.
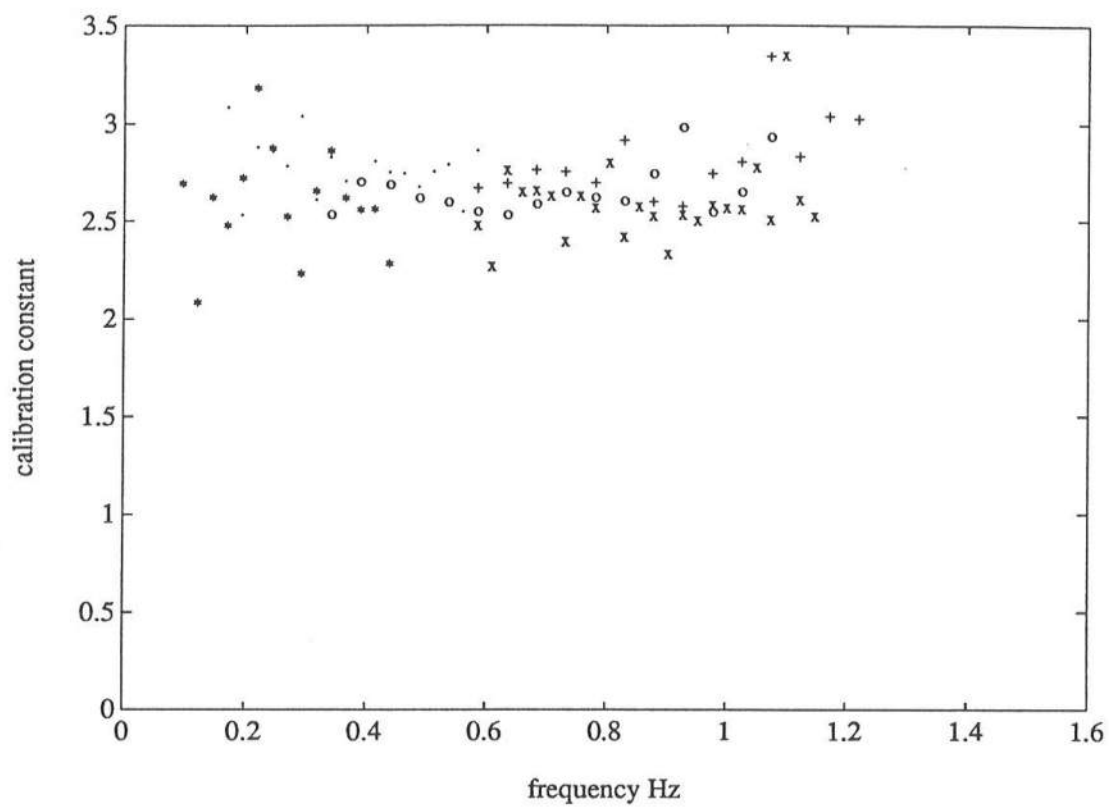
Table A.2: Experimental details for calibration of current meter $WE\,62$, y–direction.

File name	Central frequency f_c (Hz)	Bandwidth Δf	Sampling frequency f_s (Hz)	Wave height at breaking (m)	Distance of breaker point from wavemaker X_b (m)
yr162.dat	0.71	0.75	50	0.30	20.0
yr562.dat	1.10	1.00	50	0.20	20.0
yl162.dat	0.30	0.40	50	0.30	20.0
yl262.dat	0.25	0.30	50	0.30	20.0
yl362.dat	0.25	0.30	50	0.30	20.0

Equation for calibration curve (best fit straight line):

$$y = 2.5447 + 0.3421x$$
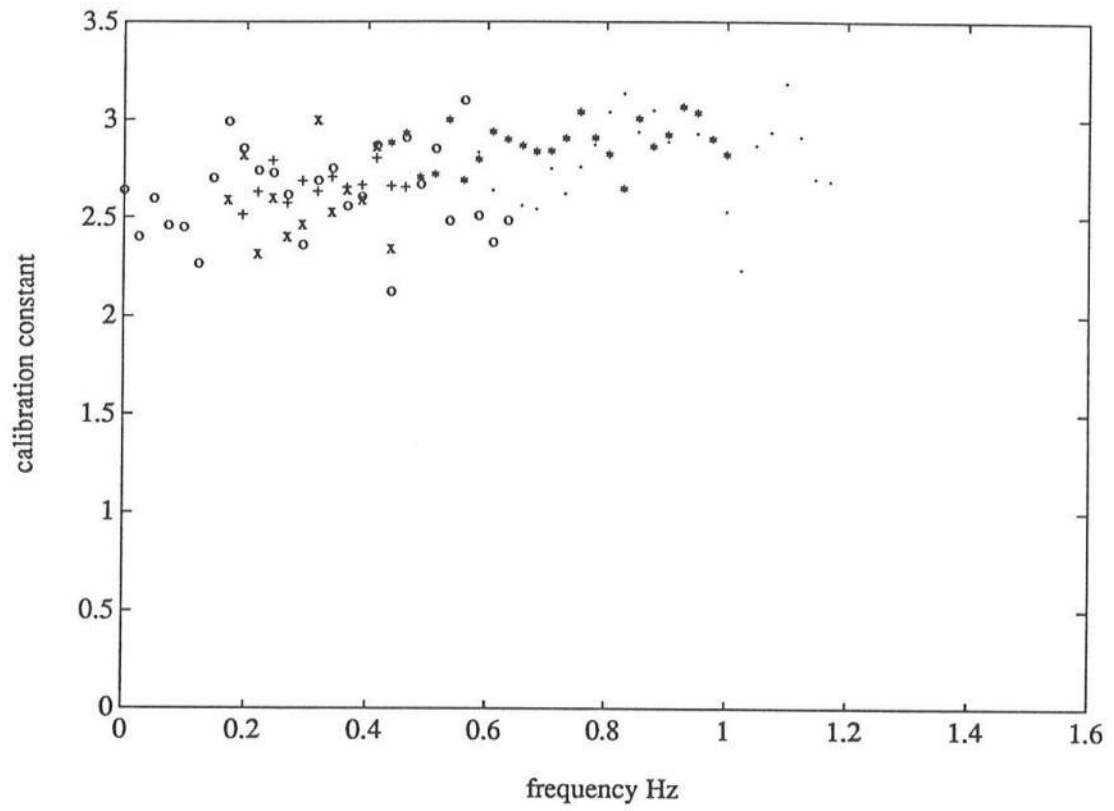
Figure A.2: Experimental calibration data for current meter $WE\,62$, y–direction.

Table A.3: Experimental details for calibration of current meter $WE\,27$, x–direction.

File name	Central frequency f_c (Hz)	Bandwidth Δf	Sampling frequency f_s (Hz)	Wave height at breaking (m)	Distance of breaker point from wavemaker X_b (m)
xr127.dat	0.71	0.75	50	0.30	20.0
xr527.dat	1.10	1.00	50	0.20	20.0
xl127.dat	0.30	0.40	50	0.30	20.0
xl227.dat	0.25	0.30	50	0.30	20.0

Equation for calibration curve (best fit straight line):

$$y = 2.9668 + 0.2615x$$
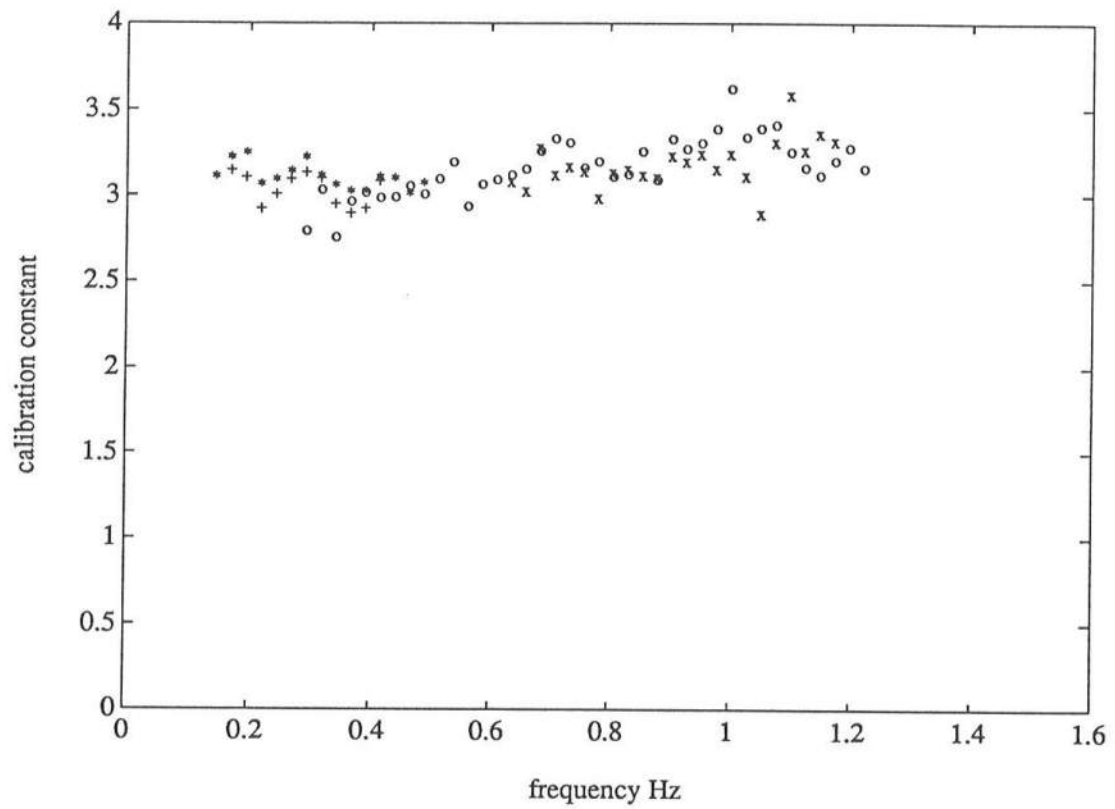
Figure A.3: Experimental calibration data for current meter $WE\,27$, x-direction.

Table A.4: Experimental details for calibration of current meter $WE\,27$, y–direction.

File name	Central frequency f_c (Hz)	Bandwidth Δf	Sampling frequency f_s (Hz)	Wave height at breaking (m)	Distance of breaker point from wavemaker X_b (m)
yr127.dat	0.71	0.75	50	0.30	20.0
yr527.dat	1.10	1.00	50	0.20	20.0
yl127.dat	0.30	0.40	50	0.30	20.0
yl227.dat	0.25	0.30	50	0.30	20.0

Equation for calibration curve (best fit straight line):

$$y = 2.5354 + 0.6382x$$
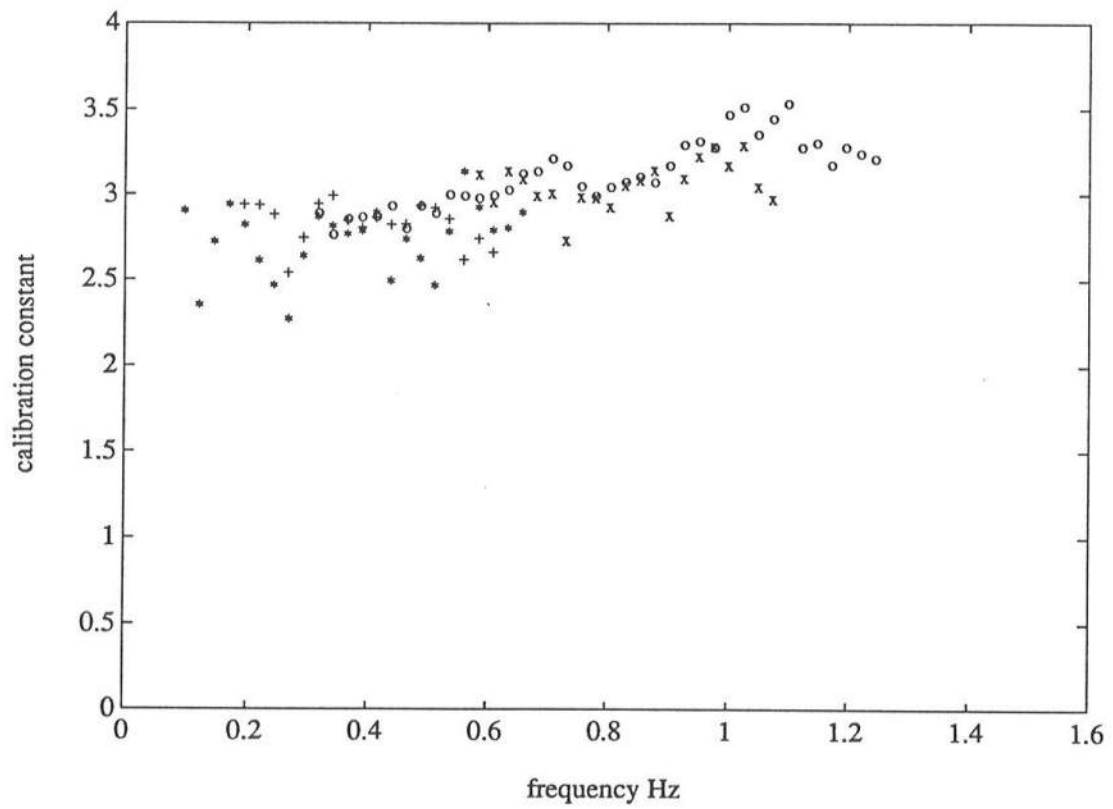
Figure A.4: Experimental calibration data for current meter $WE\,27$, y–direction.

Appendix B

CHECKS FOR EDGE WAVE RESONANCE CONDITIONS

Experimental test case: QTEST

```
WAVE TRAIN 1 : WAVE PERIOD          =  .934
               SIGMA (FREQUENCY)    =  6.7272
               DEEP WATER INC. ANGLE =  -1.1829
               SHALLOW  "     "    "  "  =  -1.

WAVE TRAIN 2 : WAVE PERIOD          =  .9488
               SIGMA (FREQUENCY)    =  6.6222
               DEEP WATER INC. ANGLE =  11.965
               SHALLOW  "     "    "  "  =  10.

MODE  0 : LHS =  1.10113E-2
          RHS =  .99924    DIFFERENCE =  -.98823
MODE  1 : LHS =  1.10113E-2
          RHS =  2.958     DIFFERENCE =  -2.947
MODE  2 : LHS =  1.10113E-2
          RHS =  4.7993    DIFFERENCE =  -4.7883
MODE  3 : LHS =  1.10113E-2
          RHS =  6.4498    DIFFERENCE =  -6.4388
MODE  4 : LHS =  1.10113E-2
          RHS =  7.8441    DIFFERENCE =  -7.8331
MODE  5 : LHS =  1.10113E-2
          RHS =  8.9267    DIFFERENCE =  -8.9157
```

132

Experimental test case: RTEST and PTEST

```
WAVE TRAIN 1 : WAVE PERIOD          = .9734
               SIGMA (FREQUENCY)    = 6.4549
               DEEP WATER INC. ANGLE = -12.154
               SHALLOW "    "    " " = -10.

WAVE TRAIN 2 : WAVE PERIOD          = 1.
               SIGMA (FREQUENCY)    = 6.2832
               DEEP WATER INC. ANGLE = 3.6946
               SHALLOW "    "    " " = 3.

MODE  0 : LHS =  2.94807E-2
          RHS =  1.1279    DIFFERENCE = -1.0984
MODE  1 : LHS =  2.94807E-2
          RHS =  3.3388    DIFFERENCE = -3.3093
MODE  2 : LHS =  2.94807E-2
          RHS =  5.4171    DIFFERENCE = -5.3876
MODE  3 : LHS =  2.94807E-2
          RHS =  7.2801    DIFFERENCE = -7.2506
MODE  4 : LHS =  2.94807E-2
          RHS =  8.8538    DIFFERENCE = -8.8244
MODE  5 : LHS =  2.94807E-2
          RHS =  10.076    DIFFERENCE = -10.046
```

Experimental test case: STEST

```
WAVE TRAIN 1 : WAVE PERIOD              =  .9706
               SIGMA (FREQUENCY)        =  6.4735
               DEEP WATER INC. ANGLE =  36.651
               SHALLOW  "      "      "  "  =  30.

WAVE TRAIN 2 : WAVE PERIOD              =  .9488
               SIGMA (FREQUENCY)        =  6.6222
               DEEP WATER INC. ANGLE =  12.133
               SHALLOW  "      "      "  "  =  10.

MODE  0 : LHS =  2.2123E-2
          RHS =  1.5746    DIFFERENCE =  -1.5524
MODE  1 : LHS =  2.2123E-2
          RHS =  4.6611    DIFFERENCE =  -4.639
MODE  2 : LHS =  2.2123E-2
          RHS =  7.5625    DIFFERENCE =  -7.5404
MODE  3 : LHS =  2.2123E-2
          RHS =  10.163    DIFFERENCE =  -10.141
MODE  4 : LHS =  2.2123E-2
          RHS =  12.36     DIFFERENCE =  -12.338
MODE  5 : LHS =  2.2123E-2
          RHS =  14.066    DIFFERENCE =  -14.044
```

Experimental test case: STEST

```
WAVE TRAIN 1 : WAVE PERIOD           =  .9706
               SIGMA (FREQUENCY)     =  6.4735
               DEEP WATER INC. ANGLE = -142.76
               SHALLOW "    "    " "  = -30.

WAVE TRAIN 2 : WAVE PERIOD           =  .9488
               SIGMA (FREQUENCY)     =  6.6222
               DEEP WATER INC. ANGLE = -168.03
               SHALLOW "    "    " "  = -10.

MODE  0 : LHS =  2.2123E-2
          RHS =  1.6215    DIFFERENCE =  -1.5994
MODE  1 : LHS =  2.2123E-2
          RHS =  4.8001    DIFFERENCE =  -4.7779
MODE  2 : LHS =  2.2123E-2
          RHS =  7.7879    DIFFERENCE =  -7.7658
MODE  3 : LHS =  2.2123E-2
          RHS =  10.466    DIFFERENCE = -10.444
MODE  4 : LHS =  2.2123E-2
          RHS =  12.729    DIFFERENCE = -12.707
MODE  5 : LHS =  2.2123E-2
          RHS =  14.486    DIFFERENCE = -14.463
```

Experimental test case: PQTEST (i)

```
WAVE TRAIN 1 : WAVE PERIOD            =  1.
               SIGMA (FREQUENCY)      =  6.2832
               DEEP WATER INC. ANGLE  =  3.6946
               SHALLOW "     "    " " =  3.

WAVE TRAIN 2 : WAVE PERIOD            =  .97233
               SIGMA (FREQUENCY)      =  6.462
               DEEP WATER INC. ANGLE  = -12.154
               SHALLOW "     "    " " = -10.

MODE  0 : LHS =  3.19601E-2
          RHS =  1.1298    DIFFERENCE =  -1.0978
MODE  1 : LHS =  3.19601E-2
          RHS =  3.3445    DIFFERENCE =  -3.3125
MODE  2 : LHS =  3.19601E-2
          RHS =  5.4263    DIFFERENCE =  -5.3943
MODE  3 : LHS =  3.19601E-2
          RHS =  7.2925    DIFFERENCE =  -7.2605
MODE  4 : LHS =  3.19601E-2
          RHS =  8.8689    DIFFERENCE =  -8.8369
MODE  5 : LHS =  3.19601E-2
          RHS =  10.093    DIFFERENCE =  -10.061
```

Experimental test case: PQTEST (ii)

```
WAVE TRAIN 1 : WAVE PERIOD              =  .9488
                SIGMA (FREQUENCY)       =  6.6222
                DEEP WATER INC. ANGLE   =  11.965
                SHALLOW "     "    " "  =  10.

WAVE TRAIN 2 : WAVE PERIOD              =  .934
                SIGMA (FREQUENCY)       =  6.7272
                DEEP WATER INC. ANGLE   =  -1.1829
                SHALLOW "     "    " "  =  -1.

MODE  0 : LHS =  1.10113E-2
          RHS =  .99924    DIFFERENCE =  -.98823
MODE  1 : LHS =  1.10113E-2
          RHS =  2.958     DIFFERENCE =  -2.947
MODE  2 : LHS =  1.10113E-2
          RHS =  4.7993    DIFFERENCE =  -4.7883
MODE  3 : LHS =  1.10113E-2
          RHS =  6.4498    DIFFERENCE =  -6.4388
MODE  4 : LHS =  1.10113E-2
          RHS =  7.8441    DIFFERENCE =  -7.8331
MODE  5 : LHS =  1.10113E-2
          RHS =  8.9267    DIFFERENCE =  -8.9157
```

Experimental test case: PQTEST (iii)

```
WAVE TRAIN 1 : WAVE PERIOD          =  .9734
               SIGMA (FREQUENCY)    =  6.4549
               DEEP WATER INC. ANGLE = -12.154
               SHALLOW "    "    " " = -10.

WAVE TRAIN 2 : WAVE PERIOD          =  .9488
               SIGMA (FREQUENCY)    =  6.6222
               DEEP WATER INC. ANGLE =  11.965
               SHALLOW "    "    " " =  10.

MODE  0 : LHS =  2.80092E-2
          RHS =  1.7805    DIFFERENCE =  -1.7524
MODE  1 : LHS =  2.80092E-2
          RHS =  5.2706    DIFFERENCE =  -5.2426
MODE  2 : LHS =  2.80092E-2
          RHS =  8.5514    DIFFERENCE =  -8.5234
MODE  3 : LHS =  2.80092E-2
          RHS =  11.492    DIFFERENCE = -11.464
MODE  4 : LHS =  2.80092E-2
          RHS =  13.977    DIFFERENCE = -13.949
MODE  5 : LHS =  2.80092E-2
          RHS =  15.906    DIFFERENCE = -15.878
```

Experimental test case: PQTEST (iv)

```
WAVE TRAIN 1 : WAVE PERIOD              =  1.
               SIGMA (FREQUENCY)        =  6.2832
               DEEP WATER INC. ANGLE =  3.6946
               SHALLOW "     "      " "  =  3.

WAVE TRAIN 2 : WAVE PERIOD              =  .934
               SIGMA (FREQUENCY)        =  6.7272
               DEEP WATER INC. ANGLE =  -1.1829
               SHALLOW "     "      " "  =  -1.

MODE  0 : LHS =  .19713
          RHS =  .34666      DIFFERENCE =  -.14953
MODE  1 : LHS =  .19713
          RHS =  1.0262      DIFFERENCE =  -.82907
MODE  2 : LHS =  .19713
          RHS =  1.665       DIFFERENCE =  -1.4678
MODE  3 : LHS =  .19713
          RHS =  2.2376      DIFFERENCE =  -2.0405
MODE  4 : LHS =  .19713
          RHS =  2.7213      DIFFERENCE =  -2.5242
MODE  5 : LHS =  .19713
          RHS =  3.0969      DIFFERENCE =  -2.8997
```

Experimental test case: PQTEST (v)

```
WAVE TRAIN 1 : WAVE PERIOD           =  1.
               SIGMA (FREQUENCY)      =  6.2832
               DEEP WATER INC. ANGLE  =  3.6946
               SHALLOW "    "    " "  =  3.

WAVE TRAIN 2 : WAVE PERIOD           =  .9488
               SIGMA (FREQUENCY)      =  6.6222
               DEEP WATER INC. ANGLE  =  11.965
               SHALLOW "    "    " "  =  10.

MODE  0 : LHS =   .11496
          RHS =   .65258     DIFFERENCE =  -.53762
MODE  1 : LHS =   .11496
          RHS =  1.9318      DIFFERENCE =  -1.8169
MODE  2 : LHS =   .11496
          RHS =  3.1343      DIFFERENCE =  -3.0193
MODE  3 : LHS =   .11496
          RHS =  4.2122      DIFFERENCE =  -4.0973
MODE  4 : LHS =   .11496
          RHS =  5.1228      DIFFERENCE =  -5.0079
MODE  5 : LHS =   .11496
          RHS =  5.8298      DIFFERENCE =  -5.7149
```

Experimental test case: PQTEST (vi)

```
WAVE TRAIN 1 : WAVE PERIOD            =  .9734
                SIGMA (FREQUENCY)     =  6.4549
                DEEP WATER INC. ANGLE = -12.154
                SHALLOW "    "    " "  = -10.

WAVE TRAIN 2 : WAVE PERIOD            =  .934
                SIGMA (FREQUENCY)     =  6.7272
                DEEP WATER INC. ANGLE = -1.1829
                SHALLOW "    "    " "  = -1.

MODE  0 : LHS =  7.41441E-2
          RHS =  .78121    DIFFERENCE = -.70707
MODE  1 : LHS =  7.41441E-2
          RHS =  2.3126    DIFFERENCE = -2.2385
MODE  2 : LHS =  7.41441E-2
          RHS =  3.7521    DIFFERENCE = -3.6779
MODE  3 : LHS =  7.41441E-2
          RHS =  5.0425    DIFFERENCE = -4.9684
MODE  4 : LHS =  7.41441E-2
          RHS =  6.1326    DIFFERENCE = -6.0584
MODE  5 : LHS =  7.41441E-2
          RHS =  6.9789    DIFFERENCE = -6.9048
```

Appendix C

WAVE PARAMETER FILES

The wave parameter files are used as input to the designer waves generation program. They contain information in the following format:

\# of component waves

1/2 width of wave basin, X_m

integration step in x–direction

padddle stroke voltage (mV), $T_1/2$ (s), θ_1, phase difference

padddle stroke voltage (mV), $T_2/2$ (s), θ_2, phase difference

padddle stroke voltage (mV), $T_3/2$ (s), θ_3, phase difference

repeat for \# of component waves......

Experimental test case: QTEST

```
2
7.36,10.80
0.1
150,0.4744,10,0
150,0.4670,-01,0
```

Experimental test case: RTEST

```
2
7.36,10.85
0.1
150,0.5000,3,0
150,0.4867,-10,0
```

Experimental test case: PTEST

```
2
7.36,10.80
0.1
200,0.5000,3,0
200,0.4867,-10,0
```

Experimental test case: STEST

```
2
7.36,10.80
0.1
150,0.4744,-10,0
150,0.4853,-30,0
```

Experimental test case: P2TEST

```
2
7.36,12.20
0.1
200,0.5000,3,0
200,0.4867,-10,0
```

Experimental test case: PQTEST

```
4
7.36,12.20
0.1
100,0.5000,3,0
100,0.4867,-10,0
100,0.4744,10,0
100,0.4670,-01,0
```

Experimental test case: P2RAND, the RANDOM wave file

```
32
7.36,12.20
0.1
    0.1    .80    3.    2.746
    0.3    .77    3.    2.529
    0.6    .74    3.    4.644
    1.2    .71    3.    1.877
    2.05   .69    3.    4.644
    3.15   .67    3.    1.877
    4.55   .65    3.    4.644
    6.15   .63    3.    2.529
    8.0    .61    3.    4.644
   10.25   .59    3.    2.529
   13.15   .58    3.    2.746
   17.35   .56    3.    2.529
   23.6    .55    3.    4.644
   32.3    .53    3.    1.877
   42.3    .52    3.    4.644
   50.0    .51    3.    1.877
    0.05   .80  -10.    2.529
    0.15   .77  -10.    4.644
    0.4    .74  -10.    2.529
    0.9    .71  -10.    4.644
    1.65   .69  -10.    2.529
    2.7    .67  -10.    4.644
    4.1    .65  -10.    2.529
    5.8    .63  -10.    4.644
    7.75   .61  -10.    2.529
    9.95   .59  -10.    4.644
   12.6    .58  -10.    2.529
   16.05   .56  -10.    4.644
   21.0    .55  -10.    2.529
   28.25   .53  -10.    4.644
   38.3    .52  -10.    2.529
   50.     .51  -10.    4.644
```

Experimental test case: P2DIRAND, the RANDOM2 file

```
26
7.36,12.20
0.1
    2.    .77    6.    2.459
    5.    .77    2.    1.877
    1.    .71    8.    2.432
   26.    .71    4.    2.529
    7.    .71    0.    3.767
   48.    .63    6.    2.459
  121.    .63    2.    1.877
    4.    .63   -2.    1.361
  132.    .56    6.    2.459
  344.    .56    2.    1.877
   15.    .56   -2.    1.361
   50.    .51    8.    2.432
 1000.    .51    4.    2.529
  364.    .51    0.    3.767
    2.    .51   -4.    3.449
    1.    .80  -10.    2.529
   22.    .69   -8.    2.459
   18.    .69  -12.    1.877
    2.    .59   -4.    3.449
  127.    .59   -8.    3.984
  113.    .59  -12.    2.746
    2.    .59  -16.    3.064
    6.    .53   -4.    3.449
  351.    .53   -8.    3.984
  331.    .53  -12.    2.746
    5.    .53  -16.    3.064
```

Appendix D

EXAMPLE WAVE SPECTRA FOR P2RAND AND P2DIRAND
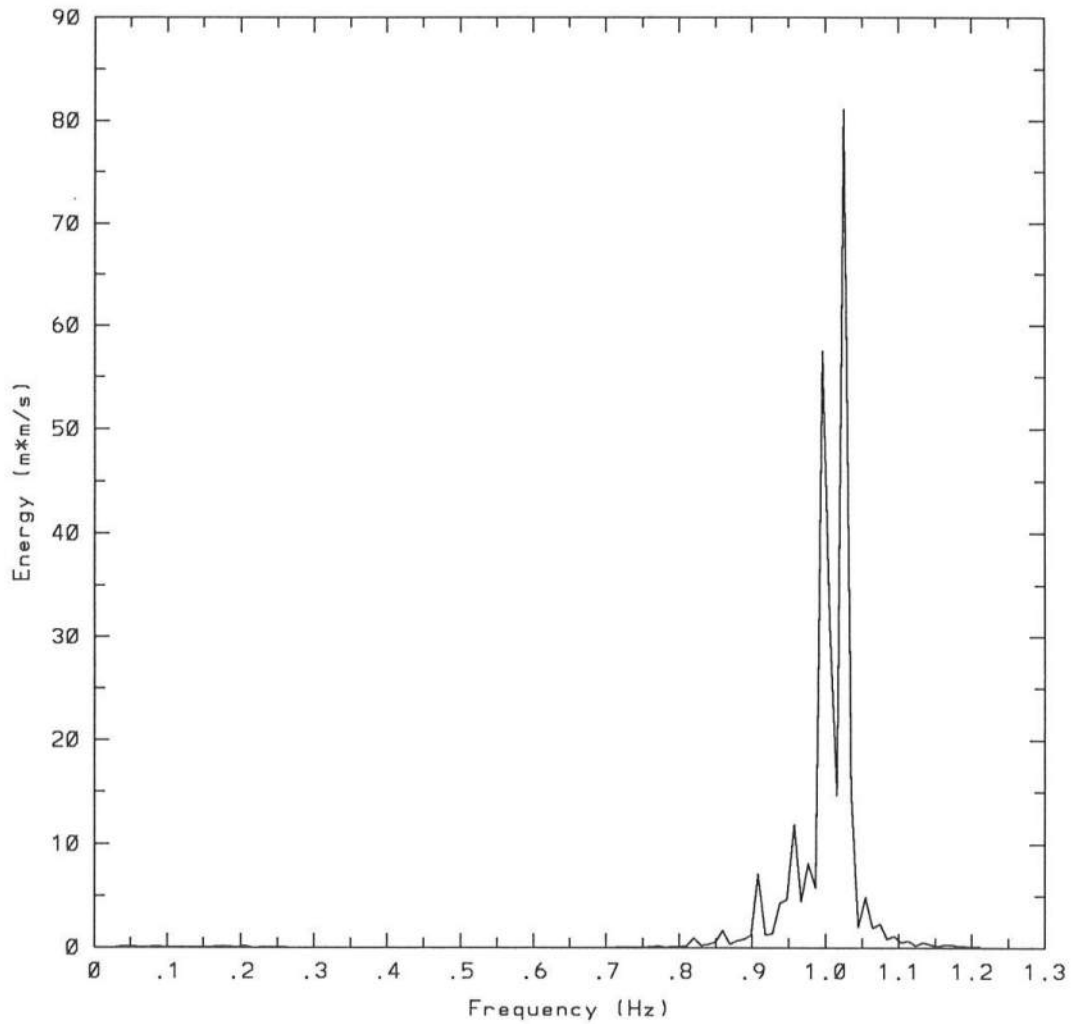## EXPERIMENTAL TEST CASES.

Figure D.1: P2RAND incident wave spectrum from data collected at one location in the wave gauge array. 4 Bartlett segments of 1024 points averaged.
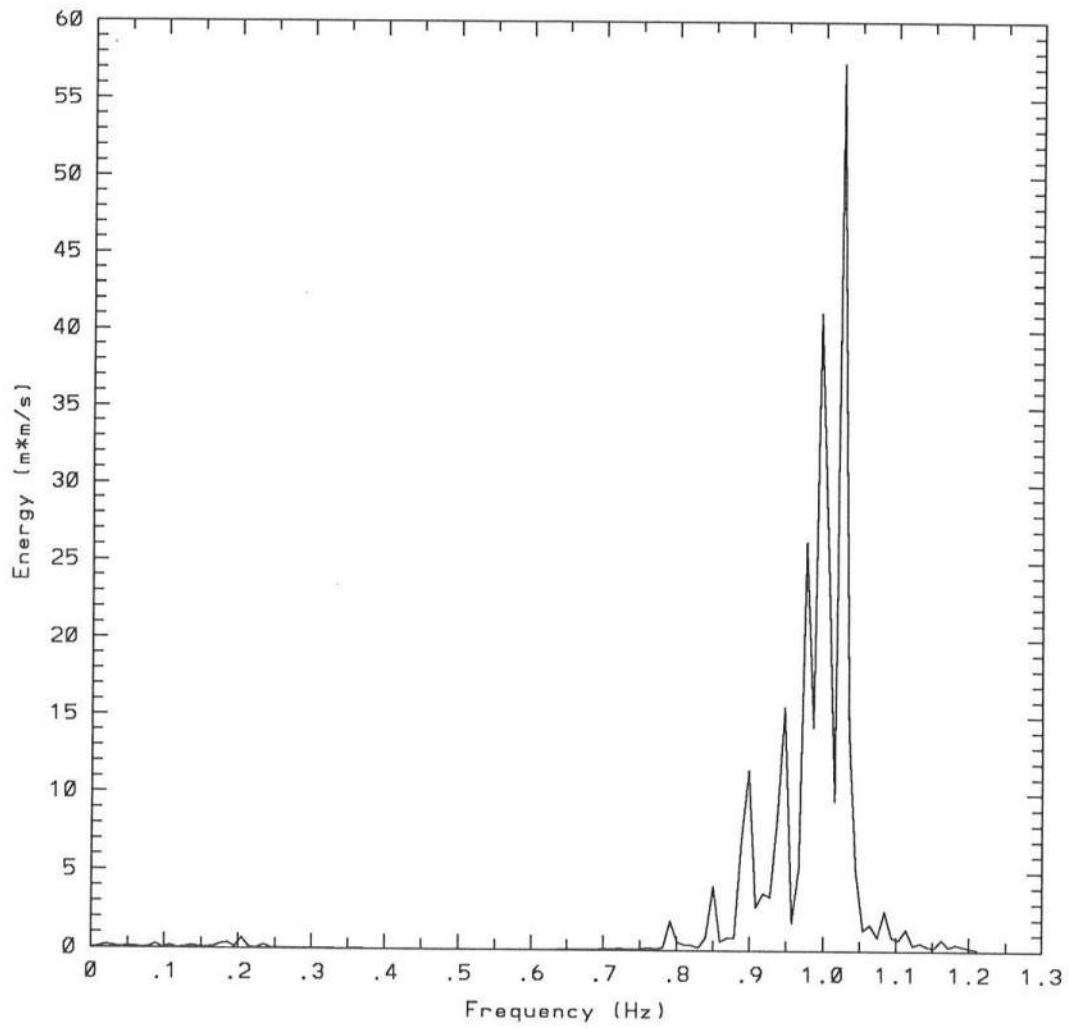
146

Figure D.2: P2DIRAND incident wave spectrum from data collected at one location in the wave gauge array. 4 Bartlett segments of 1024 points averaged.